

Upscaling the evolution of snow microstructure: From 4D image analysis to rigorous models

THÈSE N° 7996 (2017)

PRÉSENTÉE LE 27 OCTOBRE 2017

À LA FACULTÉ DE L'ENVIRONNEMENT NATUREL, ARCHITECTURAL ET CONSTRUIT
LABORATOIRE DES SCIENCES CRYOSPHÉRIQUES
PROGRAMME DOCTORAL EN GÉNIE CIVIL ET ENVIRONNEMENT

ÉCOLE POLYTECHNIQUE FÉDÉRALE DE LAUSANNE

POUR L'OBTENTION DU GRADE DE DOCTEUR ÈS SCIENCES

PAR

Quirien Eibhilín KROL

acceptée sur proposition du jury:

Prof. C. Ancey, président du jury
Prof. M. Lehning, Dr H. Löwe, directeurs de thèse
Dr F. Flin, rapporteur
Prof. E. Adams, rapporteur
Dr S. Haussener, rapporteuse



ÉCOLE POLYTECHNIQUE
FÉDÉRALE DE LAUSANNE

Suisse
2017

Canto Ostinato

Sectie 74

Simeon ten Holt



Voor Oma Henny

Acknowledgements

This thesis would not have been possible without the help and support of various people.

First of all I am very grateful to my direct supervisor Dr. Henning Löwe. Without his support and guidance this thesis would not have been possible. I am especially thankful for the numerous brainstorm sessions and in-depth discussions that often led to enlightenment and better understanding of the complex behavior of snow. His patience with my chaotic approach showed dedication and endurance. Thank you for keeping me focussed and on the road towards scientific results. Your curiosity and high level skill-set made me enjoy the often difficult process in the last four years.

I would like to thank my thesis director Prof. Michael Lehning for all the discussions on the progress of the last couple of years. With his enthusiasm and quick understanding of the scientific problems he provided the necessary perspective. Thank you for taking on the role of thesis-director of my thesis.

In addition I would like to thank the other members of the thesis-committee: Dr. Sophia Haussener, Dr. Frédéric Flin, Prof. Edward Adams and Prof. Christophe Ancey to accept the invitation, taking the time to review the thesis and take part in my oral examination.

My appreciation goes to the people that have been conducting the experiments on which this thesis heavily relies: Bernd Pinzer, Stefan Schleef and Henning Löwe.

To Nathalie who has proof read a great deal of this thesis: thank you for being there at the right moment!

I especially want to thank Bert, for supporting me in this whole process. Thank you for moving with me to Switzerland, it has been and still is a great adventure. Thank you for teaching me how to ski and enjoy *Snow* from a very different perspective, you have been very patient. I love to be out there with you.

Last but not least I want to thank my Family and Friends. The list for both, close-by and far away, is far too long and without risking to forget very important individuals I thank you all collectively!

Davos, 10 July 2017

Quirine

Abstract

Snow microstructure and its evolution play an important role for various applications of snow physics in cryospheric sciences. The main modes of microstructure evolution in snow are referred to as isothermal and temperature gradient metamorphism. The former describes the coarsening driven by interfacial energy while the latter is dominated by recrystallization processes induced by temperature gradients. An accurate description of these processes in snowpack models is of key importance. However, common snowpack models are still based on traditional grain metrics, originally tailored to field observations, and empirical evolution laws. This treatment of snow microstructure is essentially unrelated to recent advances of snow observations by micro-computed tomography (μ CT). The present thesis contributes to the solution of this problem by i) identifying suitable microstructure parameters ii) deriving evolution equations for these from first principles and iii) developing methods that allow to utilize 4D μ CT measurements of snow as a link between local ice crystal growth and upscaled microstructure as relevant on the scales of interest for common snowpack models. To this end, three studies have been conducted.

The first study focuses on estimating local ice-crystal growth rates from interface tracking by analyzing 4D μ CT data of in-situ snow metamorphism experiments under isothermal and temperature gradient conditions. For temperature gradient metamorphism, diffusion-limited growth is considered, while for isothermal metamorphism the data is compared to kinetics and diffusion limited growth. Despite considerable scatter, in both cases the significance of underlying growth laws could be statistically confirmed.

The second study uses μ CT images from a variety of snow samples to investigate the role of grain shape in the context of microwave and optical properties of snow. Grain shape can be objectively defined via size-dispersity of structure from the second moment of either the mean curvature distribution or the chord-length distribution. In addition, a quantitative link between these quantities and the exponential correlation length is established. The latter is relevant for parameterizing macroscopic properties such as microwave scattering coefficients, dielectric permittivity and thermal conductivity.

Finally, a rigorous, upscaled microstructure scheme is developed by deriving mathematically exact evolution equations for the density, specific surface area, the mean and Gaussian curvature and the second moment of mean curvature. The microstructural evolution is driven by local ice crystal growth. All parameters are upscaled by volume averaging and the correctness of the model is confirmed for the time evolution of idealized grains. The model can be compared to 4D μ CT data without any a-priori assumptions. This benchmarking reveals the uncertainties of the interface tracking method which are largely caused by limited temporal and spatial resolution. The model allows to statistically assess the validity of ice crystal growth laws during snow metamorphism. For a temperature gradient experiment it is shown that a diffusion limited growth law is not consistent with the observed decay of the specific surface area.

The developed model is a powerful and rigorous tool that is tailored to 4D μ CT data. It connects microscale ice-crystal growth thermodynamics with the macroscale snowpack modeling.

Key words:

snow, crystal growth, metamorphism, microstructure modeling, grain shape, exponential correlation length, mean curvature, Gaussian curvature, micro-computed tomography.

Zusammenfassung

Die Mikrostruktur von Schnee und ihre zeitliche Entwicklung spielen für verschiedene Anwendungen in den Kryosphärenwissenschaften eine grosse Rolle. Die wichtigsten Formen der mikrostrukturellen Umwandlung sind abbauende und aufbauende Metamorphose. Erstere beschreibt die durch Oberflächenenergie angetriebene Vergröberung unter isothermen Bedingungen. Letztere wird durch Rekristallisationsprozesse dominiert, die durch Temperaturgradienten hervorgerufen werden. Eine genaue Beschreibung dieser Prozesse in Schneedeckenmodellen ist von zentraler Bedeutung. Gängige Schneedeckenmodelle basieren jedoch auf Kornmetriken und empirischen Evolutionsgesetzen, die auf traditionelle Schnee-Beobachtungen zugeschnitten sind. Eine derartige Beschreibung der Schnee-Mikrostruktur steht jedoch kaum in einem Bezug zu den Fortschritten, die durch neueste Untersuchungen mittels Mikro-Computertomographie (μ CT) gemacht wurden. Die vorliegende Arbeit leistet wie folgt einen Beitrag zur Lösung dieses Problems: i) Identifizierung geeigneter Mikrostruktur-Parameter, ii) Herleitung von Entwicklungsgleichungen basierend auf grundlegenden Prinzipien, iii) Entwicklung einer Methode, die es erlaubt 4D μ CT Daten von Schnee als Link zwischen dem Wachstum von Eiskristallen auf kleinen Skalen und der Strukturbeschreibung auf der für Schneedeckenmodelle relevanten Skalen zu benutzen. Die Arbeit gliedert sich in drei separate Beiträge.

Die erste Studie konzentriert sich auf die Abschätzung lokaler Wachstumsraten von Eiskristallen anhand der Verfolgung von Grenzflächen bei in-situ Metamorphose-Experimenten von Schnee. Die analysierten 4D μ CT-Daten decken sowohl isotherme Bedingungen als auch solche unter Temperaturgradienten ab. Für die aufbauende Metamorphose wird ein diffusionsbegrenztes Wachstum in Betracht gezogen. Bei der abbauenden Metamorphose werden die Daten mit kinetisch begrenztem und diffusionsbegrenztem Wachstum verglichen. Trotz einer beträchtlichen Streuung, konnte für beide Fälle eine Signifikanz der zugrundeliegenden Wachstumsgesetze statistisch bestätigt werden.

Die zweite Studie verwendet μ CT-Bilder aus einer Vielzahl von Schneeproben, um den Einfluss der Kornform vor dem Hintergrund von optischen und Mikrowellen-Eigenschaften von Schnee zu untersuchen. Eine Kornform kann objektiv über die Heterogenität der Strukturgrösse definiert werden, entweder durch das zweite Moment der Verteilung der mittleren Krümmungen oder durch das zweite Moment der Sehnenlängenverteilung. Zusätzlich wird eine quantitative Verknüpfung zwischen diesen Grössen und der exponentiellen Korrelationslänge hergestellt. Letztere ist für die Parametrisierung makroskopischer Eigenschaften wie Mikrowellenstreuoeffizient, dielektrische Leitfähigkeit und Wärmeleitfähigkeit relevant.

Abschliessend wird ein rigoroses, Mikrostrukturmodell für den Skalenübergang entwickelt, indem mathematisch exakte Entwicklungsgleichungen für die Dichte, die spezifische Oberfläche, die mittlere und Gaußsche Krümmung und das zweite Moment der mittleren Krümmung abgeleitet werden. Das lokale Eiskristallwachstum bestimmt dabei die Entwicklung der Mikrostruktur. Der

Skalenübergang für die Parameter wird dabei durch Volumenmittelung erzielt. Die Richtigkeit des Modells wird anhand der zeitlichen Entwicklung von idealisierten Körnern verifiziert. Das Modell kann mit 4D μ CT Daten ohne a-priori Annahmen verglichen werden. Dieses Benchmarking zeigt die Unsicherheiten der Methode zur Verfolgung von Grenzflächen, die weitgehend durch die begrenzte zeitliche und räumliche Auflösung verursacht werden. Das Modell ermöglicht es, die Gültigkeit des Eiskristallwachstums während der Schneemetamorphose statistisch zu überprüfen. Für ein Experiment mit Temperaturgradienten wird gezeigt, dass ein diffusionsbegrenztes Wachstumsgesetz im Widerspruch zur beobachteten Abnahme der spezifischen Oberfläche ist. Das neu entwickelte Modell ist ein mächtiges und rigoroses Werkzeug welches auf 4D μ CT Daten zugeschnitten wurde. Es verknüpft dabei die Thermodynamik des Eiskristallwachstums auf der Mikroskala mit der makroskopischen Schneedecken-Modellierung.

Stich wörter:

Schnee, Kristallwachstum, Metamorphose, Mikrostrukturmodellierung, Kornform, exponentielle Korrelationslänge, mittlere Krümmung, Gausssche Krümmung, Mikro-Computertomographie.

Contents

Acknowledgements	v
Abstract (English/Deutsch)	i
List of figures	ix
List of tables	xiii
List of Constants and Symbols	xv
1 Introduction	1
1.1 Context	1
1.2 Structural controls on physical properties	1
1.3 Experimental characterization of snow microstructure	3
1.4 Snow metamorphism	3
1.5 Model approaches to microstructure evolution	6
1.5.1 Isothermal conditions	6
1.5.2 Temperature gradient conditions	8
1.6 Microstructure representation in snowpack models	9
1.7 Research Gap and Objectives	10
1.8 Outline	11
2 Analysis of local ice crystal growth in snow	15
2.1 Introduction	15
2.2 Theoretical Background	17
2.2.1 Temperature gradient dominated growth	18
2.2.2 Curvature dominated growth: Diffusion limited case	20
2.2.3 Curvature dominated growth: Kinetics limited case	21
2.3 Methods	21
2.3.1 Curvatures and normal vectors	22
2.3.2 Interface tracking	23
2.3.3 Local Temperature Gradients	26
2.3.4 Discerning settling and growth	27
2.3.5 Sub voxel sample position corrections	27
2.4 Results	28
2.4.1 Curvature driven metamorphism	28
2.4.2 Temperature gradient driven metamorphism	30

2.5	Discussion	33
2.5.1	Curvature driven metamorphism	33
2.5.2	Temperature gradient driven metamorphism	35
2.6	Conclusions	37
3	Relating optical and microwave grain metrics of snow: The relevance of grain shape	39
3.1	Introduction	39
3.2	Theoretical background	41
3.2.1	Two-point correlation function and microwave metrics	41
3.2.2	Chord length distributions and optical metrics	43
3.2.3	Connection between chord lengths and the Porod length and the curvature-length	44
3.3	Methods	45
3.3.1	Data	45
3.3.2	Geometry from two-point correlation functions	45
3.3.3	Geometry from triangulations	46
3.3.4	Accuracy of surface area and curvatures estimates	46
3.3.5	Chord length distribution	48
3.3.6	Statistical models	48
3.4	Results	48
3.4.1	Relating exponential correlation length to the Porod length and curvature-length	48
3.4.2	Connection between chord length distributions and two-point correlation functions	49
3.4.3	Relating the second moment of the chord length distribution to the Porod length and the curvature-length	49
3.4.4	Relating microwave metrics and optical metrics	53
3.4.5	Shape factors g^G and B	54
3.5	Discussion	55
3.5.1	Methodology	55
3.5.2	Linking size metrics in snow	57
3.5.3	Grain shape	59
3.6	Conclusions	62
3.7	Appendix: Optical shape factor B from moments of the chord length distribution	62
3.8	Acknowledgements	63
4	Upscaling ice-crystal growth dynamics in snow: Rigorous modeling and comparison to 4D X-ray tomography data	65
4.1	Introduction	65
4.2	Upscaling of microstructure in snow metamorphism	67
4.2.1	Preliminaries and notation	67
4.2.2	Volume and surface averages	68
4.2.3	Evolution of the ice volume fraction	69
4.2.4	Evolution of the surface area per unit volume	69

4.2.5	Evolution of interfacial curvatures	70
4.3	Interface evolution of idealized grains	70
4.3.1	Reduced evolution equations	70
4.3.2	Generation of initial states	71
4.4	Ice-air interface evolution from 4D tomography data	72
4.4.1	Time lapse experiments and interface tracking	72
4.4.2	Results	73
4.5	Statistical analysis of crystal growth laws	74
4.5.1	Growth laws for temperature gradient driven growth	74
4.5.2	Results	75
4.6	Discussion	77
4.6.1	Main findings	77
4.6.2	Limitations and prospects	78
4.7	Conclusions	79
4.8	Appendices	79
4.8.1	Derivation of the surface area equation	79
4.8.2	Derivation of the curvature equations	80
5	Assessment of growth laws for isothermal metamorphism	81
5.1	Introduction	81
5.2	Evolution equation for SSA_V and $\overline{H^2}$	82
5.3	Data and Methodology	83
5.4	Growth laws for isothermal metamorphism	84
5.5	Results	86
5.6	Discussion and Conclusion	87
6	Conclusion	91
7	Limitations and Outlook	95
7.1	Image analysis and experimental setup	95
7.2	Modeling snow microstructure	96
	Bibliography	109
	Curriculum Vitae	111

List of Figures

1.1	A comparison between microscopic images and μ CT visualization of two snowtypes. Left: depth hoar (DH), right: Precipitation particles (PP). Photographs are taken from Fierz et al. [2009]. 3D images are taken from a temperature gradient metamorphism experiment [Pinzer et al., 2012] and an isothermal metamorphism experiment [Schleef et al., 2014].	4
1.2	Schematic of Nakaya’s ice-crystal morphology diagram [Nakaya, 1954] showing the various shapes of snow-crystals grown under different temperature and super-saturation conditions (Fig. 4 from Deville [2013])	5
1.3	Visual representation of isothermal metamorphism at 4 timesteps ($\Delta t = 45$ hours and the cube length is 1.5 mm)	6
1.4	Visual representation of temperature gradient metamorphism at 4 timesteps ($\Delta t = 192$ hours and the cube length is 3.51 mm).	7
1.5	Schematic overview of the thesis, which contributes to connecting microstructural evolution at three different scales. Left: Snow as a continuum in macroscopic snow cover modeling. Middle: Snow as a bicontinuous structure as seen by μ CT. Right: Individual snow crystals top: modeled figures from Demange et al. [2017a], bottom: photographs from Libbrecht [2006]).	10
2.1	Schematic of the iterative interface tracking. Γ_i and Γ_f represent two consecutive images and the dashed lines the simulated intermediate interfaces. In contrast to d_n , d_{\min} is not perpendicular to Γ_i . d_g is perpendicular to the simulated interfaces.	22
2.2	Scatter plot of measured distances d_{meas} as a function of prescribed distances d_n for $N = 4, 8, 12, 16$ iterations. $d_g = \overline{d_{\text{meas}}(d_f)}$, the averaged value for the final iteration ($N = 18$).	23
2.3	Measured errors E as a function of prescribed growth with corresponding ε . The lower bound for the estimated error $E_{\varepsilon_{\text{exp}}}$ for the temperature gradient experiment are indicated by the dashed red line.	24
2.4	Measured errors E as a function of the number of iterations N . The estimated error corresponding to the minimal distance measurement of the experimental data $E_{\varepsilon_{\text{exp}}}$ is indicated by the dashed red line.	25
2.5	Visualization of the curvature difference $\overline{H} - H$ (left) and the normal distances d_g computed from the interface tracking (right) for the the first sample of the isothermal time-series. The size of the sample is $60 \times 60 \times 60$ voxels.	28

2.6	Interface velocities for the isothermal time series. Top: Two-dimensional histograms for v_n and the growth law Equation (2.12) for $t = 0$ h (left) and $t = 30$ h (right). Bottom: Two-dimensional histograms for v_n and the growth law Equation (2.14), for $t = 0$ h (left) and $t = 30$ h (right).	29
2.7	Left: Fitted values B_{exp} from Equation (2.12) with the Pearson correlation coefficient r over time t . For comparison the theoretical value B_{theo} evaluated at -18°C from Equation (2.13) is shown. Right: Fitted values C_{exp} from Equation (2.14) with the Pearson correlation coefficient r over time t . For comparison the theoretical value C_{theo} evaluated at -18°C from Equation (2.15). Note that C_{theo} is only an order of magnitude estimate.	30
2.8	Visualization of the temperature gradient projected on the normal $\nabla T \cdot \mathbf{n}$ (left) and the normal distances d_g computed from the interface tracking (right) for the the first sample of the temperature gradient time-series. The size of the sample is $70 \times 70 \times 70$ voxels.	31
2.9	Interface velocities for the temperature gradient time series shown as two-dimensional histograms at four different times for the velocity v_n as a function of local temperature gradients $\nabla T \cdot \mathbf{n}$. Included are two fits for A from Equation (2.9), a weighted least squares and a tangent fit for small $\nabla T \cdot \mathbf{n}$	32
2.10	Left: Fitted values A_{exp} from Equation (2.9) with the Pearson correlation coefficient r over time t . For comparison the theoretical value A_{theo} evaluated at -7.8°C from Equation (2.10) is shown. Right: Fitted values for B to Equation (2.12) and the sample Pearson correlation coefficient r over time. For comparison the theoretical value B_{theo} evaluated at -7.8°C from Equation (2.13) is shown. . . .	33
2.11	The sample Pearson correlation coefficients over time for various fits. r_A corresponds to the fitted data to Equation (2.9), r_B to Equation (2.12) and $r_{A,B}$ to Equation (2.27).	34
2.12	The fitted A to Equation (2.9) as a function of the scale factor ϵ as defined by Equation (2.24).	35
3.1	a) Illustration of the chord lengths obtained from an ice sample. The mean chord length is defined as the average length of the green line lengths. A stereological approach [Underwood, 1969] to calculate s is to count the number of blue dots per unit length. The estimation for s_{mf} is given by the red contour. b) Illustration of the two-point correlation function $A(r)$ and the method obtaining an estimate for the Porod length λ_1 to get s_{cf} by fitting the slope at the origin, and the exponential correlation length ξ by fitting $A(r)$ to $\exp(-r/\xi)$ over a larger span.	43
3.2	Comparison between smoothing parameter $S = 50$ (left) and $S = 200$ (right). Top: Representation of the triangulated surface of a subsection of a snow sample. Middle: Scatter plots of the Porod length λ_1^{cf} versus λ_1^{tk} , including a fit (red dotted line). Bottom: Scatter plots of the curvature-length λ_2^{cf} versus λ_2^{tk} , including a fit (red dotted line).	47

3.3	Scatter plots of a) the exponential correlation length ξ versus the Porod length λ_1 . A linear fit is plotted in green. Additionally the prediction of Eq. (3.16) (MM) is plotted in red. b) The residuals of ξ and the statistical model Eq. (3.17), versus the curvature-length λ_2 . c) The statistical model Eq. (3.18) predicting ξ depending on the Porod length λ_1 and the curvature-length λ_2	50
3.4	Comparison of the chord length distributions computed from Eq. (3.13) (symbols) and by direct analysis of the μ CT data (solid-line) for three examples of snow types (PP, RG and DH).	51
3.5	Scatter plots of a) the statistical model see Eq. (3.20) predicting $\mu_2/2\mu_1$ depending on the Porod length λ_1 , b) the residuals of $\mu_2/2\mu_1$ and the statistical model Eq. (3.20) versus the curvature-length scale parameter λ_2 , c) the statistical model predicting $(1 - \phi)\mu_2/2\mu_1$ (see Eq. (3.22)) depending on the Porod length λ_1 and the curvature-length λ_2	52
3.6	Scatterplot of the exponential correlation length ξ versus the statistical model Eq. (3.23) that depends on the first and second moment of the chord length distribution, μ_1 and μ_2	53
3.7	Scatterplot of the asymmetry factor g^G and the optical shape factor B evaluated for the refractive index at wavelength $\lambda = 1.3 \mu\text{m}$	56
4.1	Idealized grains (spheroids A,B,C and torus), surfaces colored by mean curvature H	71
4.2	Scatter plots of measured and modeled rates for interface parameters of the grains from Fig. 4.1.	72
4.3	Cubic cutouts of the ice-air interface at $t = 0$ (left) and $t = 288h$ (right) from Series 1 (top, cube length 1.26 mm) and Series 2 (bottom, cube length 2.52 mm) colored by interface velocities v_n	73
4.4	Plot of measured rates versus predicted rates for the ϕ, s, H, K, χ and H^2 from Eqs. (4.20).	74
4.5	Comparison of modeled and measured evolution of \dot{s} according to (4.22).	75
4.6	Evolution of \overline{H} and $\overline{H^2}$ restricted to growing ($n_z < 0$) and sublimating ($n_z < 0$) parts of the interface.	76
5.1	Visualization of initial and final mean curvature measures on one of the compaction experiments (natural snow at -13°C , Schleef et al. [2014]), retrieved from the VTK-based image analysis.	84
5.2	Scatter plots of the mean curvature \overline{H} and the Gaussian curvature \overline{K} measured with the VTK based image analysis and with the Minkowski functionals, according to Eq. 5.8 on TG series 2 from chapter 4. The red lines indicate the 1 : 1 correspondence.	85
5.3	Plot of the measured parameters ϕ , SSA_V , \overline{H} and $\overline{H^2}$ of all 48 datasets over time.	86
5.4	Plot of measured rates versus predicted rates for the SSA_V and $\overline{H^2}$	88
5.5	Scatter plot of fitted values for $C(T)$ and $D(T)$ as a function of temperature.	89

List of Tables

3.1	Summary Statistical Models	54
3.2	Determination of the absorption coefficient α [Warren and Brandt, 2008], the first order, the fraction of the first and second order of Eq. (3.10), and the obtained estimates for B and g^G averaged over all snowsamples, including the standard deviation σ	55
5.1	Summary: Correlation coefficients for ISO closure models	87

List of Constants and Symbols

Physical constants at temperature $T = -10^\circ\text{C}$

Symbol	Name	Dimensions	Value	Page
γ	Surface energy	Jm^{-2}	0.109	17
a	Intermolecular spacing of ice	m	3.19×10^{-10}	17
α	Condensation coefficient	-	10^{-2*}	17
κ_a	Thermal conductivity of air	$\text{Wm}^{-1}\text{K}^{-1}$	2.4×10^{-2}	18
κ_i	Thermal conductivity of ice	$\text{Wm}^{-1}\text{K}^{-1}$	2.3	18
v_{kin}	Kinetic velocity	m s^{-1}	3.3×10^{-4}	17
k_B	Boltzmann constant	$\text{m}^2\text{s}^{-2}\text{kg K}^{-1}$	1.38×10^{-23}	17
ρ_i	Ice density	kg m^{-3}	917	17
$\rho_{v,s}$	Water vapor density	kg m^{-3}	1.34	17
p	Peclet number	-	10^{-7*}	18
D_v	Diffusion coefficient for water vapor	m^2s^{-1}	2.0×10^{-7}	17
d_0	Capillary length	m	9.7×10^{-10}	17

*estimated order of magnitude

Symbols

Symbol	Name	Dimensions	Page
$\mathcal{I}(r)$	Indicator function	-	41
$C(r)$	Two-point correlation function	-	41
$p(\ell)$	Chord length distribution	-	44
ϕ	Ice volume fraction	-	41
s	Average surface area per unit volume	m^{-1}	42
SSA	Specific surface area	m^{-1}	1
SSA_V	Specific surface area	m^{-1}	81
d_{opt}	Optical diameter	m	42
λ_1	Porod length	m	42
λ_2	Curvature length	m	42
ξ	Exponential correlation length	m	42
μ_i	i-th moment of the chord length distribution	m^i	44
H	Mean curvatures	m^{-1}	7
K	Gaussian curvature	m^{-2}	7
κ_1, κ_2	Principle curvatures	m^{-1}	7
χ	Euler characteristic	-	7
T	Temperature	K	17
v_n	Growth law/Interface velocity	m s^{-1}	17
ρ_v	Water vapor density	kg m^{-3}	17

Introduction

1.1 Context

Ice crystal growth is not only of fundamental interest because of the fascinating morphologies of isolated crystals on small scales [Nakaya, 1954], there is also a practical demand for understanding the evolution of crystal growth in snow on large scales e.g. for applications like avalanche formation [Schweizer et al., 2003]. Virtually any scientific problem involving physical properties of snow depends highly on the microstructure of the snowpack. Given the range of scales of interest, there is a clear need from an application point of view to model the evolution of snowpacks on large scales within continuum approaches for heat and mass transfer, and describe the snowpack in terms of objective microstructural parameters that are relevant for the application. Current snowpack models are still formulated (SNOWPACK [Lehning et al., 2002] and CROCUS [Vionnet et al., 2012]) in terms of traditional parameters [Fierz et al., 2009] that can be conveniently measured in the field. On the other hand, significant progress has been made in previous years to characterize snow metamorphism in the laboratory by micro-computed-tomography (μ CT) measurements. However, a systematic attempt to establish a link between the requirements of microstructure evolution in snowpack models and the full capabilities of μ CT has not yet been undertaken. This requires a “microstructural balancing act” between fully oppositional perspectives on snow dynamics, the large-scale, environmental modeling perspective [Barrere et al., 2017] and the small-scale, material science perspective [Demange et al., 2017a]. A contribution to this balancing act is the subject of the present thesis.

1.2 Structural controls on physical properties

One of the most important effects of snow on the climate system is that the relatively high albedo reflects a large part of the electromagnetic radiation back into the atmosphere. The surface of the earth is up to 50% for land and up to 7% for oceans, covered by snow and ice, significantly influencing the energy budget of the earth [IPCC, 2013]. The snow cover on the Antarctic as well as the Arctic and Greenland protects the sea-ice and ice-sheets from melting [IPCC, 2013]. The snow cover albedo is found to be highly dependent on snow microstructure, specifically on the specific surface area (SSA), (e.g. Wiscombe and Warren [1980], Gardner and Sharp [2010] and Dumont et al. [2014]), which is defined as the surface area per ice-mass. The

SSA is an objective measure related to the optical diameter by $d_{\text{opt}} = 6/\text{SSA}\rho_i$ in terms of the density of ice ρ_i . In the optical spectral regime the reflected radiation surmounts up to 95%, and is approximately independent of wavelength, giving the snow its white appearance.

Besides the predominant role of SSA on the snow surface to reflect radiation, the penetration-depth of the remaining, transmitted radiation depends also on the shape of the crystals [Libois et al., 2013, 2014]. Here, the shape is defined by two parameters that can be inferred from optical measurements [Kokhanovsky and Zege, 2004]. These shape parameters can be calculated for simple geometrical objects such as spheroids and hexagonal plates [Picard et al., 2009], but for a continuous structure such as snow it is unclear how these shape factors should be derived. An interesting approach modeling light absorption and scattering in porous material is geometrical optics developed by Malinka [2014] which is based on the chord length distribution. The first moment of the chord length distribution, the mean chord length, can be directly related to the SSA [Linow et al., 2012]. Including the ice-volume fraction ϕ the mean chord length can be related to the average pore size which is relevant for various pore space transport properties (e.g. Zalc et al. [2004]).

Another effect of snow microstructure becomes apparent for both active and passive (remote) sensing of the earth in the microwave regime (e.g. Mätzler [1998], Mätzler and Wiesmann [1999], Roy et al. [2013], Koch et al. [2014] and Leinss et al. [2016]), which is used to estimate the grain size and water-content of the snow. Since the grain size of the snowpack and its water-content are relevant for the energy balance of snow covered surfaces, it also influences the energy balance of the earth at a global scale, and the state of melt and consecutive flooding on regional scales [Würzler et al., 2017]. To retrieve grain size from remote sensing in the microwave regime, radiative transfer models are used [Brucker et al., 2010, Roy et al., 2013]. A key microstructural parameter influencing microwave radiative transfer is the exponential correlation length, derived from the two-point correlation function [Vallese and Kong, 1981, Wiesmann and Mätzler, 1999]. The exponential correlation length is approximately related to the Porod length (related to the inverse SSA) [Mätzler, 2002], however a considerable scatter between these two parameters is observed and the uncertainties still lack a geometrical interpretation.

The two-point correlation function of snow is an important quantity for deriving also other effective properties of complex random heterogeneous materials [Torquato, 2002]. For example, the effective thermal conductivity of the snowpack is, to a large extent controlled by the density but the remaining scatter can be explained by the anisotropy of the ice-matrix [Löwe et al., 2013]. The same anisotropy metric derived from the two-point correlation function can be alternatively retrieved from polarimetric radar measurements [Leinss et al., 2016].

This non-comprehensive list of examples shows that key physical properties are governed by different microstructural parameters, posing a key-challenge for unified modeling approaches that can focus only on a few of them.

1.3 Experimental characterization of snow microstructure

A prerequisite of understanding physical properties of snow are objective microstructural measurements. Snow microstructure has been characterized in alpine snowpacks for over decades. Historically, snow has been characterized by grain size, grain shape, density, and hardness from snowprofiles experiments in their natural environment. Parameters such as grain size and grain shape are defined according to ‘The international classification of seasonal snow on the ground’ [Fierz et al., 2009] and are generally determined from individual grains by visual inspection under a magnifying glass. Grain shape is a very important characteristic for the prognostics of snow conditions in alpine regions, particularly due to their importance for avalanche risk assessment and forecasting. A comprehensive list of typical shapes that indicates the state of the snowpack is given in Fierz et al. [2009].

Besides snow profiling, snow samples can also be casted and analyzed in a cold laboratory. The SSA can be obtained from stereology [Underwood, 1969], on thin-sections [Perla et al., 1986], gas-absorption experiments [Legagneux et al., 2002] and micro-computed tomography (μ CT) [Hagenmuller et al., 2016]. All methods measuring the SSA come with their strengths, practical limitations and uncertainties. The ‘Intercomparison of snow grain size measurements workshop’ reported their findings in a special issue in *The Cryosphere* dedicated to this issue (e.g. Carlsen et al. [2017]).

One of the most influencing experimental methods developed in the last two decades is certainly X-ray tomography. 3D imaging of snow samples with μ CT has thereby made considerable progress [Coléou et al., 2001, Flin et al., 2004, Schneebeli and Sokratov, 2004, Kaempfer and Schneebeli, 2007, Wang, 2008, Haussener et al., 2012, Pinzer et al., 2012, Schleef and Löwe, 2013, Calonne et al., 2014a, Wiese and Schneebeli, 2017]. In Fig. 1.1 a comparison of 2D microscopy and 3D μ CT imaging of two typical snow types is shown. Since μ CT gives access to the full microstructure of the sample at the micrometer scale, it enables computation of virtually any parameter of interest.

A powerful extension to regular 3D and 4D X-ray images was developed in recent years, where time-resolved (4D) imaging became more popular. Given its non-destructive nature, it enables time-lapse analysis, such as the assessment of the evolution of the microstructure over time. Due to instrumented sample holders, e.g. with Peltier-elements for temperature control [Pinzer et al., 2012, Calonne et al., 2015, Wiese and Schneebeli, 2017], both isothermal and temperature gradient metamorphism can be studied in-situ.

1.4 Snow metamorphism

In contrast to the human perception of being a cold substance, snow is actually a ‘hot’ material from a physical point of view. In typical terrestrial environments for temperatures in the range (-30°C to 0°C), the homologous temperature $T_h = T/T_m$ (i.e. the ratio of the temperature to the melting temperature in Kelvin) ranges from 0.9 to 1.0. This means that snow is always very close to its melting temperature, far from equilibrium and prone to structural changes at short times. The focus of this thesis will be on dry snow, and is therefore only concerned with

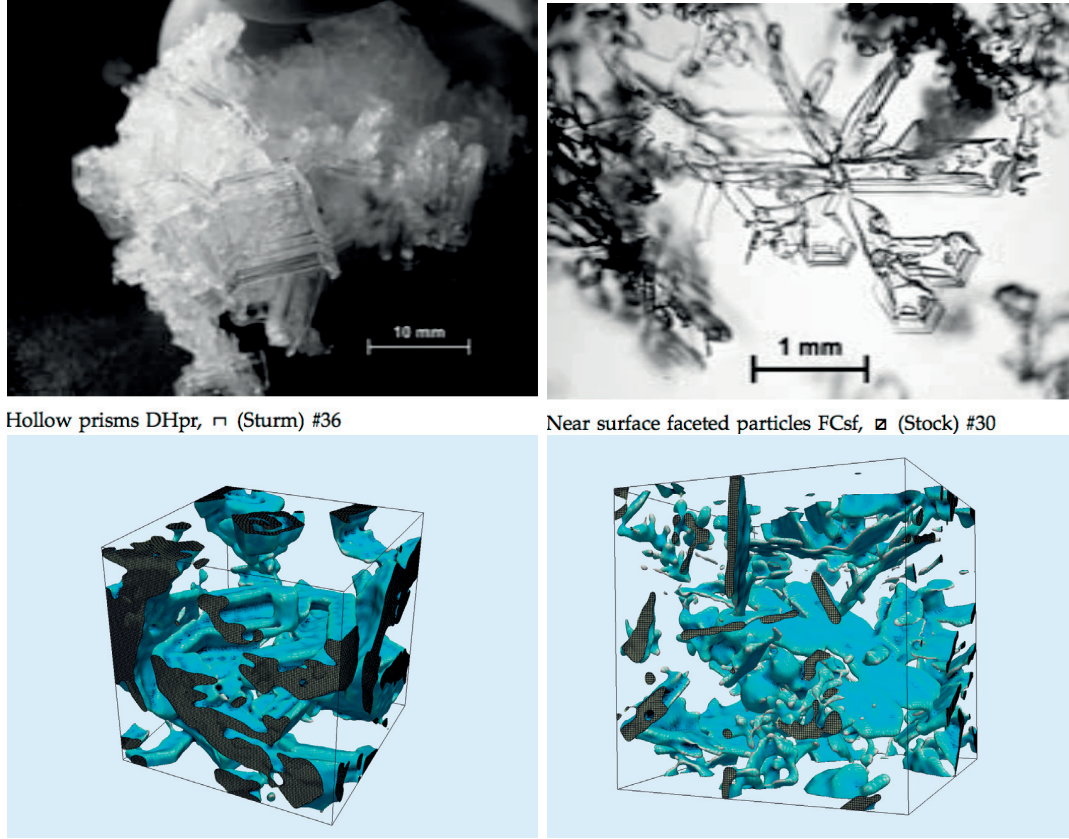


Figure 1.1 – A comparison between microscopic images and μ CT visualization of two snowtypes. Left: depth hoar (DH), right: Precipitation particles (PP). Photographs are taken from Fierz et al. [2009]. 3D images are taken from a temperature gradient metamorphism experiment [Pinzer et al., 2012] and an isothermal metamorphism experiment [Schleef et al., 2014].

solid-vapor phase changes.

After snowfall, fresh snow consists of aggregated precipitation particles formed in the atmosphere. Depending on the temperature and water vapor concentration of the environment, the initial structure of snowflakes varies considerably from columnar or needle like shapes to highly dendritic structures [Nakaya, 1954] (see Fig. 1.2). Once fallen on the earth's surface, snow immediately sinters into a highly-connected, heterogeneous material consisting of an aggregate of mono-crystalline particles. The hexagonal and plate-like structures, a clear signature of the underlying crystal orientation, rapidly disappear and cannot be visually discerned anymore. The heterogeneous material of new (dry) snow can have very low density, even below 50 kg m^{-3} . Over time, the microstructure changes due to recrystallization and gravitational compaction, resulting in higher densities of up to 500 kg m^{-3} for seasonal snow. The temporal variability of snow microstructure yields a wide spread in its mechanical, optical and thermal macroscopic properties.

Fresh snow crystals are highly dendritic with small structural features and therefore have a high SSA. The SSA generally decreases over time due to coarsening, commonly referred to as destructive or isothermal metamorphism [Fierz et al., 2009]. A visualization of this process

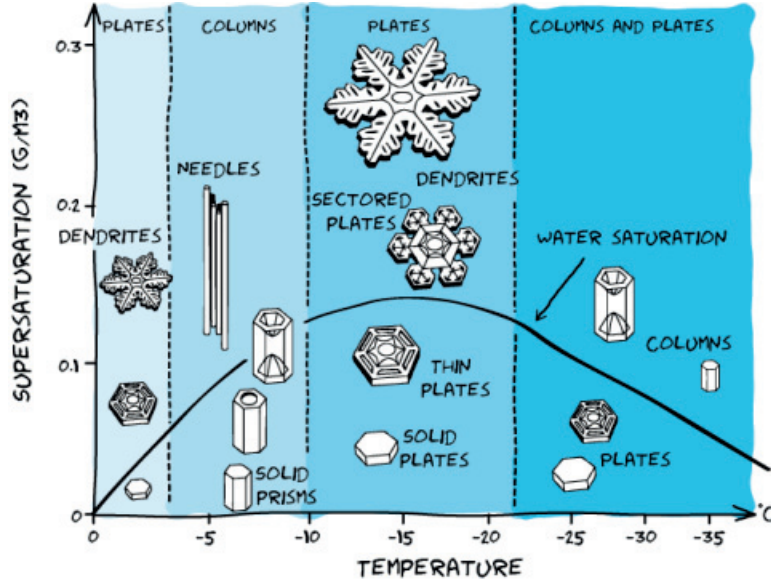


Figure 1.2 – Schematic of Nakaya’s ice-crystal morphology diagram [Nakaya, 1954] showing the various shapes of snow-crystals grown under different temperature and super-saturation conditions (Fig. 4 from Deville [2013])

based on actual μ CT images from an isothermal experiment [Schleef et al., 2014] is shown in Fig. 1.3. This mechanism is driven by the minimization of the surface free energy [Ratke and Voorhees, 2002] of the ice-air interface. The coarsening process in fresh snow is accompanied by compaction due to the weight of (new) snow, in which the Euler characteristic plays an important role [Schleef et al., 2014]. The Euler characteristic is a topological measure that is related to the number of connections (or holes) of a given structure. It has been shown that an applied stress in new snow influences the evolution of the Euler characteristic, but does not significantly influence the evolution of the SSA [Schleef et al., 2014].

Typical thermodynamic conditions for a natural snowpack during the winter season are however far from isothermal, they are rather dominated by the average temperature difference between the ground (approximately zero degrees) and the colder air just above the snowpack. This difference causes a dynamic heat flux through the snowpack. An important consequence of these thermodynamic boundary conditions are the induced vapor fluxes in the pore space which in turn cause ice-crystals to grow on the colder and sublime on the warmer side [Colbeck, 1983]. This process causes a morphological evolution that can drastically change the entire structure, thereby influencing its macroscopic physical properties. A visualization based on μ CT images of a temperature gradient metamorphism experiment [Pinzer et al., 2012] is given in Fig. 1.4. The resulting depth hoar crystals are characterized by chain- or cup-like structures (see Fig. 1.1). Similar to isothermal metamorphism, the SSA commonly decays over time but the rates are much higher (e.g. Taillandier et al. [2007]). In most experiments the SSA decays [Calonne et al., 2014a, Wiese and Schneebeli, 2017], but in some experiments the opposite is measured [Domine et al., 2009, Pinzer et al., 2012]. The increase of SSA is not yet described by any model.

Temperature gradient conditions are typical for shallow snowpacks or in regions with highly fluctuating temperatures caused by the diurnal cycle. Especially during the early season and

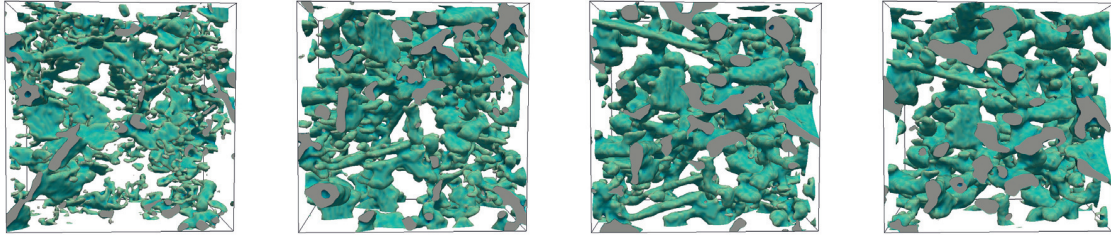


Figure 1.3 – Visual representation of isothermal metamorphism at 4 timesteps ($\Delta t = 45$ hours and the cube length is 1.5 mm)

in inner alpine regions, local temperature gradients can be very high. These conditions cause depth-hoar crystals (DH) to grow rapidly, increasing the mechanical instability of the snowpack [Schweizer and Wiesinger, 2001, Schweizer et al., 2003]. Unstable snowpacks are prone to trigger avalanches which endanger not only skiers and mountaineers active in the mountain areas, but also local infrastructure and mountain villages. For risk assessment it is therefore important to predict where and when these layers form [Huggel, 2015], which requires appropriate models. Besides that DH crystals cause mechanical unstable layers within the snowpack, they also influence the density significantly. Shallow snowpacks or snowpacks that have been extensively exposed to temperature gradients, develop a low density layer in the DH base which may significantly influence the effective thermal conductivity of the snowpack [Domine et al., 2016].

1.5 Model approaches to microstructure evolution

1.5.1 Isothermal conditions

The most significant progress of relating the dynamics of microstructural properties to pore-scale mass transport has been made for isothermal metamorphism. Isothermal metamorphism has been studied thoroughly both from experimental [Flin et al., 2004, Kaempfer and Schneebeli, 2007] and theoretical points of view [Adams and Brown, 1982, Legagneux and Dominé, 2005, Flanner and Zender, 2006].

All studies relate to, at least from the phenomenology, to the so called process of Ostwald ripening [Ratke and Voorhees, 2002]. Ostwald ripening is characterized by the growth of the average size of a collection of particles that interact by vapor diffusion and growth with or without attachment kinetics. The classical theoretical framework is provided by the Lifshits-Slyozov-Wagner (LSW) theory for diffusion limited [Lifshitz and Slyozov, 1961, Wagner, 1961] and kinetics limited growth [Wagner, 1961], which provide minimal models for these processes. For a microstructure comprising a collection of spheres, the larger particles can grow at the cost of smaller ones. The time evolution of the average radius of the spheres can be seen as an upscaled isothermal model.

The dominant underlying process that cause the coarsening may differ leading to different power-laws for the growth of the average sizes of the particles [Ratke and Voorhees, 2002]. But all processes involve the equilibrium vapor pressure in the vicinity of the interface. The equilibrium vapor pressure depends on the size of the individual particle, or more precisely on

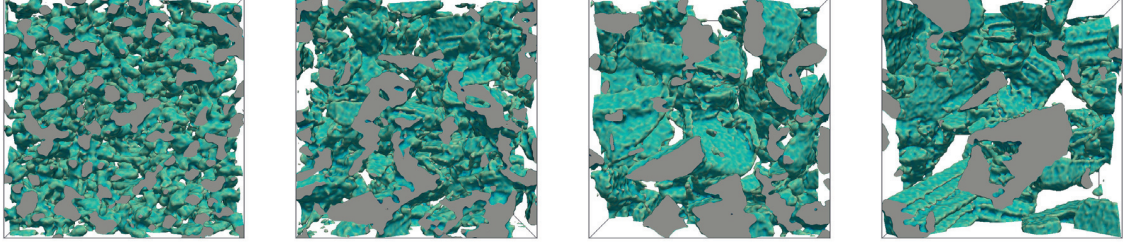


Figure 1.4 – Visual representation of temperature gradient metamorphism at 4 timesteps ($\Delta t = 192$ hours and the cube length is 3.51 mm).

the mean curvature via the Gibbs-Thomson equation [Thomson, 1871]. The mean curvature H is defined for all points on a smooth interface and given by the divergence of the normal vector \mathbf{n} , or equivalently, the mean of the two principle curvatures κ_1, κ_2 [Spivak, 1975],

$$H = \frac{1}{2} (\nabla \cdot \mathbf{n}) = \frac{1}{2} (\kappa_1 + \kappa_2). \quad (1.1)$$

The principle curvatures are given by the minimal and maximal reciprocal of all possible inscribed radii.

An obvious problem of the LSW model is that it is restricted to spherical particles. The microstructure of snow is however highly connected and the LSW theory lacks an immediate analogue if measured with μ CT. Moreover, from an experimental point of view, it has been recognized that the Euler characteristic, a topological measure for the connectivity, changes over time [Schleef and Löwe, 2013, Calonne et al., 2014a]. The Euler characteristic χ is closely related to the area average of the Gaussian curvature K by

$$\chi = \frac{1}{2\pi} \int K da, \quad (1.2)$$

where K is given by the two principle curvatures

$$K = \kappa_1 \kappa_2. \quad (1.3)$$

The Euler characteristic is relevant for mechanical properties in snow [Schleef et al., 2014], and cannot be captured by isolated spherical particles. For bicontinuous heterogeneous media, such as snow, a generalization of the LSW model framework to bicontinuous structures is required in order to describe isothermal coarsening in porous snow and to cope with microstructural parameters like the mean and Gaussian curvature.

The relevance of curvatures is also stressed from a purely material science point of view, where the problem of predicting averaged properties of coarsening microstructures is ongoing and far from being solved [Fife et al., 2014]. The latter work emphasizes the relevance of an additional length scale for the diffusion process that depends on both mean and Gaussian curvature, which are relevant to build a mean field theory for bicontinuous interfaces [Tomita, 2000]. In Fife et al.

[2014] μ CT was used as a tool to measure and verify the predicted interface velocities. These recent advances from material science are highly relevant for the development of a microstructure evolution model for snow.

1.5.2 Temperature gradient conditions

Although isothermal coarsening is a fundamental process for snow metamorphism, it becomes less important when initial high-curvature parts of the structure disappear. Then, temperature gradient metamorphism has a dominant influence and a microstructural evolution model must be able to describe it. The main driver of temperature gradient metamorphism in snow is the temperature difference in the snowpack as described in the previous section. Since the equilibrium vapor pressure of water vapor depends on temperature, the vapor pressure varies in the snowpack. These variations cause a flux of vapor in the pore spaces, which in turn causes local ice crystals to sublime on the warmer sides and vapor depositing on the colder sides. To model these transport processes, the coupled heat and mass equations must be solved simultaneously at the pore scale. Because structural changes are slow compared to the adjustment of the heat and vapor fluxes to the structure, usually stationary versions of the heat and vapor equations can be considered [Libbrecht, 2003]. Both equations are mutually coupled via latent heat and the temperature influence on the equilibrium vapor pressure. It has been recently theoretically confirmed that latent heat can be neglected in a first approximation [Calonne et al., 2014b]. Thereby only a one-way coupling between the local temperature-field and the local vapor-field remains and needs to be solved to retrieve the vapor-flux in the pore spaces. A phase field approach has been put forward [Kaempfer and Plapp, 2009], which is based on an isotropic variant of the Hertz-Knudsen growth law including the Gibbs-Thomson effect. The computational requirements of the method are however, quite high.

Another approach to temperature gradient metamorphism has been suggested by Flanner and Zender [2006] which is based on distributions of sphere radii and pore sizes. They argue that vapor pressure sources and sinks are dependent on adjacent pore spaces. Each particle gets assigned a vector representing the super-position of all surrounding particles and the irregular particle spacings cause competition for water vapor sources, thereby favoring some particles over others based on their position. With their model they show that this leads to the frequently observed decay in SSA. However more detailed temperature gradient experiments are needed to tune their parameters. Despite other modeling work on temperature gradient metamorphism [Miller and Adams, 2009] first principles methods which are tailored to the complex microstructure of snow are still missing.

Probably the most sophisticated growth model presently available for isolated snow crystal growth is that of Barrett et al. [2012] which includes the competition between both diffusive and kinetic effects, by taking into account the lattice anisotropy of ice crystals. In principle, such a model could be generalized to more complex geometries to capture the effect in snow. This would, however, require simultaneous information on crystal orientations during metamorphism, which is technically feasible but still complex from an experimental point of view. Although a proof of concept exists [Rolland du Roscoat et al., 2011], systematic approaches are presently out of reach. In view of the structural complexity of snow, simplifications are needed to meet

the requirements of snowpack models.

1.6 Microstructure representation in snowpack models

Predicting the macroscopic physical properties of snow from the microstructural evolution is one of the long standing challenges for current snow pack models. Available snowpack models that describe snow metamorphism, such as SNOWPACK [Lehning et al., 2002] and CROCUS [Vionnet et al., 2012], use parameters like density, grain size, dendricity and sphericity to describe the microstructure. The choice of parameters was based on the convenience for traditional field observations to characterize snow on the millimeter scale with a magnifying glass. The disadvantage of these parameters is that they depend on the observer and therefore are, to a certain extent, subjective. Furthermore, they do not have an objective equivalent that can be validated in controlled and reproducible laboratory experiments by using μ CT. Current snowpack models treat the evolution of the snow parameters in a phenomenological way (e.g Bartelt and Lehning [2002] and Legagneux and Dominé [2005]). They often use parametrized functions to predict the evolution of a few experiments, but these are derived from particle-based growth mechanisms mentioned in the previous section and do not represent the complexity of a highly connected geometry.

It has indeed been recognized by Carmagnola et al. [2014] that snowpack parameters are not sufficient or not well-defined and in need of improvement. To evolve towards more objective parameters, Carmagnola et al. [2014] have proposed a reformulation of the microstructural description in terms of the optical diameter d_{opt} and suggested to drop the dendricity parameter without losing a reduction in predictability. The parameterization however, remains similar in nature to the formulations used before. The improvement is that at least one parameter has an objective definition. This study subsequently raises the question of how many parameters are needed to predict snow microstructure. Based on Carmagnola et al. [2014], it is very likely that the four parameters used by SNOWPACK are not orthogonal and three or even two parameters describing the microstructure could have similar prognostic capabilities. Besides improving the definitions or the choice of the actual parameters, the parametrization that describes its evolution should be upgraded towards more physics-based descriptions.

To improve on the representation of microstructure in snowpack models, as required for many applications in cryospheric sciences, the structural changes need to be related to the actual physical processes for crystal-growth at a smaller scale. Therefore a constitutive growth law for the ice-vapor interface that couples the transport of heat and mass diffusion to local properties of the interface is needed. Recent attempts to upscale the transport equations to include a macroscopic temperature gradient was developed by Calonne et al. [2014b] and Hansen and Foslien [2015] using homogenization and mixture theory respectively. The upscaled temperature and vapor equations thereby depend on the density and the SSA as microstructural parameters. A microstructure model would thus at least require evolution equations for these parameters in terms of the average temperature and temperature gradient.

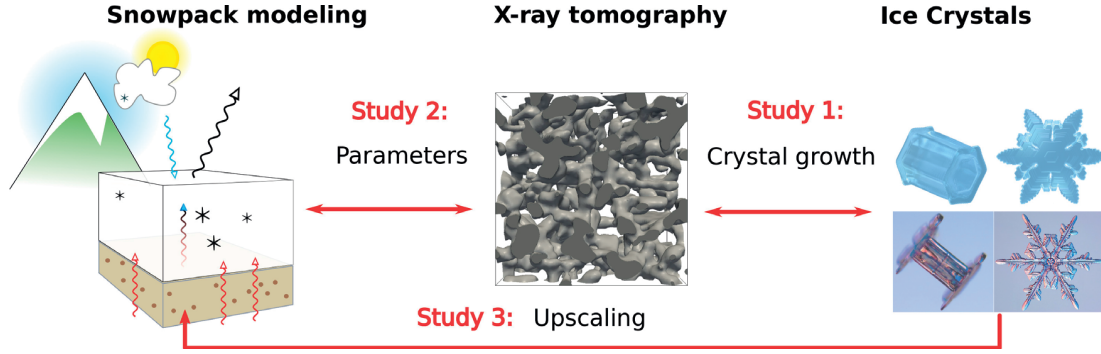


Figure 1.5 – Schematic overview of the thesis, which contributes to connecting microstructural evolution at three different scales. Left: Snow as a continuum in macroscopic snow cover modeling. Middle: Snow as a bicontinuous structure as seen by μ CT. Right: Individual snow crystals top: modeled figures from Demange et al. [2017a], bottom: photographs from Libbrecht [2006]).

1.7 Research Gap and Objectives

Based on the previous introduction, we have to acknowledge that modeling snow microstructure evolution is a multiscale problem. At the scale of individual ice-crystals, growth processes are relatively well understood, which is reflected by the successful simulations of the 3D morphologies of snow crystals formed in the atmosphere [Barrett et al., 2012, Demange et al., 2017a]. At the micro scale snow microstructure has been extensively studied over the last two decades using 4D μ CT data. These studies have used the full 3D microstructure to assess the evolution of derived physical properties such as density, SSA, effective conductivity and permeability. However, crystal growth, which is the key process to assess microstructural changes at these scales, has hitherto not been quantified. At the larger scales, snowpack models such as SNOWPACK and CROCUS need microstructural parameters to calculate macroscopic quantities such as the albedo and effective conductivity. As described in the previous section, it is not even clear on which and how many parameters snowpack models should focus. Therefore, to ensure that the choice of parameters is relevant and to some extent orthogonal, it is necessary to relate most of the objective parameters that can be obtained from μ CT. Although the ingredients of microstructural evolution should be based on the same physical process, namely crystal growth, the links between recent advances in crystal growth theory, microstructural evolution of snow at the micro scale, and snowpack modeling are presently missing. There is a clear need to evolve snow microstructure modeling to a more physics based approach that utilizes the recent advances in μ CT observations of snow. To assist this development, we have conducted three studies that are presented in the upcoming chapters of this thesis. These studies, as diagrammatically depicted in Fig.1.5, aim at 1) quantifying crystal growth in 4D μ CT observations, 2) finding relations between objective parameters obtained from 3D μ CT images to avoid redundancy and guide the choice of parameters for 3) developing a snow microstructure evolution model.

The aim of the first study is to develop an image analysis tool that can measure local crystal growth rates in snow for both isothermal and temperature gradient conditions. The recent development of time-lapse measurements of snow allows for a comparison of two consecutive, 3D binary images. To retrieve a measure of local ice-crystal growth, an image analysis method

must be developed. This method will be based on the minimal distance calculation between two consecutive images that estimates local growth rates at all points on the ice-air interface. With a measure for local growth rates, a first attempt of relating crystal growth to theoretical growth laws will be feasible. For isothermal conditions, the main focus will be on relating local growth rates to local mean curvatures to assess existing ideas on coarsening processes in snow. For temperature gradient conditions the local growth rates will be compared to local temperature gradients in the vicinity of the ice-air interface. To obtain estimates for local temperature gradients, we will use the finite element simulation developed by Pinzer et al. [2012].

The aim of the second study will be to interrelate a range of objective parameters that can be obtained from μ CT images to find a set of parameters that can be used for the development of microstructure modeling. For this purpose, we will focus on parameters that can be estimated using the two-point correlation function and the chord length distribution, since these structure and distribution functions have been proven relevant to thermal conductivity, microwave modeling and geometrical optics. These two functions can be directly measured from μ CT images and yield estimates for the density, optical diameter, SSA, Porod length, exponential correlation length, chord length and higher order parameters, such as the curvature length. The latter is related to the mean and Gaussian curvature and a size-dispersity parameter (the second moment of the chord length distribution). In addition to an in-depth analysis of interrelating the aforementioned listed parameters, the role of grain shape will be investigated within geometrical optics and microwave modeling. The obtained relations between these parameters will guide the choice of a minimal set of parameters that avoid unnecessary redundancy, and can be considered in the development of a microstructure model for snow.

The third aim is to develop an upscaled microstructure model for snow that relates to objective microstructural parameters and metamorphism by means of crystal growth. Local heat and vapor transport and crystal growth are tightly coupled (e.g. Libbrecht [2005], Kaempfer and Plapp [2009], Pinzer et al. [2012]) and upscaling local heat and vapor transport by homogenization and mixture theory has successfully carried out [Calonne et al., 2014b, Hansen and Foslien, 2015]. The microstructure is nevertheless treated statically in both approaches. An equivalent approach for microstructure modeling is therefore needed. The main idea is to start from a local description of the dynamic ice-air interface that is given by the level-set equation [Sethian, 1999] and use the local evolution of the principle curvatures driven by the a priori unknown interface velocity (representing crystal growth) derived by Drew [1990]. The evolution of the averaged surface area is then obtained by volume averaging these ingredients, from which a hierarchical system of coupled partial differential equations arises that include evolution equations for the Mean and Gaussian curvatures. Since crystal growth is represented by the interface velocity, theoretical growth laws could in principle be validated via their influence on the overall evolution of the microstructure.

1.8 Outline

The three main objectives mentioned in the previous section are addressed in the main body of this thesis. The content of chapters 2, 3 and 4 has been published or submitted in peer-reviewed open-access journals. The work is presented in chronological order. Chapter 4 presents the

microstructural evolution model of snow in a general form and are compared only to 4D μ CT data of temperature gradient experiments. In chapter 5, preliminary results for comparison of the model to isothermal metamorphism experiments are presented within the same mathematical setup used in chapter 4.

Chapter 2: Analysis of local ice crystal growth in snow

This chapter has been published and reprinted with permission (with some additional typographical corrections).

- Q. Krol and H. Löwe. Analysis of local ice crystal growth in snow. *J. Glaciol*, 62(232): 378–390, 2016a. doi: 10.1017/jog.2016.32

Summary

The structural evolution of snow under metamorphism is one of the key challenges in snow modeling. The main driving forces for metamorphism are curvature differences and temperature gradients, inducing water vapor transport and corresponding crystal growth that is detectable by the motion of the ice-air interface. To provide quantitative means for a microscopic validation of metamorphism models, a VTK-based image analysis method is developed to track the ice-air interface in time-lapse μ CT experiments to measure local interface velocities under both isothermal and temperature gradient conditions. Using estimates of local temperatures from microstructure-based finite element simulations, a quantitative comparison of measured interface velocities with theoretical expressions is facilitated. For isothermal metamorphism, the data is compared to a kinetics and a diffusion limited growth law. In both cases the data is largely scattered but consistently shows a mean curvature dependency of the interface velocity. For temperature gradient metamorphism, we confirm that the main contribution stems from the temperature gradient induced vapor flux, accompanied by effects of mean curvature as a secondary process. The scatter and uncertainties are discussed in view of the present theoretical understanding, the experimental setup, and complications such as mechanical deformations.

Chapter 3: Characteristics of snow microstructure: relevance of grain shape

This chapter has been published and reprinted with permission (with some additional typographical corrections).

- Q. Krol and H. Löwe. Relating optical and microwave grain metrics of snow: the relevance of grain shape. *The Cryosphere*, 10(6):2847–2863, 2016b. doi: 10.5194/tc-10-2847-2016

Summary

Grain shape is commonly understood as a morphological characteristic of snow that is independent of the optical diameter (or specific surface area) influencing its physical properties. In this

study we use tomography images to investigate two objectively defined metrics of grain shape that naturally extend the characterization of snow in terms of the optical diameter. One is the curvature length λ_2 , related to the third order term in the expansion of the two-point correlation function, and the other is the second moment μ_2 of the chord length distributions. We show that the exponential correlation length, widely used for microwave modeling, can be related to the optical diameter and λ_2 . Likewise, we show that the absorption enhancement parameter B and the asymmetry factor g^G , required for optical modeling, can be related to the optical diameter and μ_2 . We establish various statistical relations between all size metrics obtained from the two-point correlation function and the chord length distribution. Overall, our results suggest that the characterization of grain shape via λ_2 or μ_2 is virtually equivalent since both capture similar aspects of size dispersity. Our results provide a common ground for the different grain metrics required for optical and microwave modeling of snow.

Chapter 4: Upscaling microscopic crystal growth dynamics in snow

This chapter, has been submitted to *Acta Materialia*, July 2017. Some typographical corrections are made here.

Summary

A unified treatment of microstructure dynamics in terrestrial snow from principles of ice crystal growth is presently hindered by the lack of models for the evolution of the bicontinuous ice matrix. To this end, we developed a rigorous microstructure upscaling scheme which takes common pore-scale (diffusion) principles of crystal growth to predict the averaged evolution of the interface morphology. We derived a coupled set of evolution equations for the (volume averaged) ice volume fraction, specific surface area, Gaussian curvature and first and second moment of the mean curvature distribution, and demonstrate their correctness by a comparison to interface tracking of idealized grains. In a second step, we use the model as a benchmark tool without *a-priori* assumptions for a comparison to experiments of snow microstructure evolution via image analysis on 4D X-ray tomography data. The benchmarking allows us to quantify uncertainties from local estimates of crystal growth velocities. Finally, we demonstrate how the rigorous model facilitates a statistical assessment of common growth laws by combining 4D microstructure data with finite element numerics. The results show that the prediction of the specific surface area from first principles demands further conceptual insight from ice crystal growth.

Chapter 5: Assessment of growth laws for isothermal metamorphism

This chapter shows preliminary results of the model developed in chapter 4, tailored to isothermal metamorphism experiments.

Summary

Isothermal snow metamorphism is characterized by a combination of coarsening and settling of the highly porous heterogeneous material. Considering the specific surface area (SSA) instead of the surface area per unit volume allows us to separate compaction and crystal-growth related changes in the microstructure. We derived a new equation for the evolution of the SSA in terms of surface averages of the local interface velocity and local curvature. We assess three possible expressions for the interface velocity suggested by kinetic and diffusion limited growth laws. This enables us to rewrite the model equations in terms of geometrical parameters that can be computed by methods based on integral geometry and the two-point correlation function. The best performing model ($R^2 = 0.88$) predicts the evolution of the SSA in terms of the variance of the mean curvature and the exponential correlation length. A parametrization for the evolution of the second moment of the mean curvature is given in the terms of the same parameters as the SSA, with similar performance ($R^2 = 0.83$). The results of the model are discussed in comparison with previously obtained results given by Schleef et al. [2014].

Analysis of local ice crystal growth in snow

2.1 Introduction

Ice crystal growth is not only of fundamental interest related to the fascinating morphologies of isolated crystals [Nakaya, 1954], there is also a practical demand of understanding the collective growth of crystals in snow due to the relevance of metamorphism for environmental modeling [Fierz and Lehning, 2001], [Vionnet et al., 2012], avalanche formation [Schweizer et al., 2003] and remote sensing [Wiesmann and Mätzler, 1999]. A common phenomenological starting point to model crystal growth are variants of the Stefan problem [Kaempfer and Plapp, 2009], i.e. the coupled treatment of heat and mass diffusion in the presence of the growing crystal as a moving boundary. Heat and mass conservation are coupled at the interface via boundary conditions, which typically comprise two components, mass conservation and a so called growth law, respectively. Both involve the normal velocity v_n of the growing interface which is the key quantity of crystal growth. The growth law is not a consequence of basic conservation laws and thus requires additional input.

The simplest law for growth from the vapor phase is the Hertz–Knudsen law $v_n \sim \sigma$ in which the interface velocity is proportional to the supersaturation σ [Saito, 1996]. This has been used e.g. in Libbrecht [2005] to estimate velocities of growing snow crystals. The growth law must be understood as a microscopic constitutive equation for modeling crystal growth via ambient vapor diffusion. If surface processes like step dynamics and surface diffusion play a role (cf. discussion in Libbrecht [2005]) the growth law must be understood as an empirical closure relation, which potentially contains non-local elements of surface kinetics. The relevance of the growth law for snow modeling stems from the direct coupling to the upscaled thermodynamic fields [Calonne et al., 2014b], since the net mass change $\dot{\rho}$ of the ice matrix per unit volume V and unit time is given by $\dot{\rho} \sim \rho_i \int_A v_n da / V$. As long as snow metamorphism models are derived from pore scale diffusion models, it is necessary to validate growth laws for v_n from measurements.

From a theoretical viewpoint, an appealing example of crystal growth modeling is the migration of vapor bubbles in ice under a temperature gradient [Shreve, 1967] which is caused by vapor transport and subsequent growth. The migration and interface velocities in Shreve [1967] are based on purely diffusion limited growth where the interface kinetics are assumed to be infinitely fast. This model was e.g. used to analyze experiments for bubble migration in Antarctic

ice in view of the albedo of blue ice fields [Dadic et al., 2010]. It predicts growth rates that depend mainly on local temperature gradients which are realistic for spherical geometries. It provides thus a reasonable starting point also for snow, if limitations due to geometry can be overcome. The opposite extreme are so called geometrical models for crystal growth [Taylor et al., 1992] which completely neglect diffusion effects. An anisotropic geometrical growth law in two dimensions [Wettlaufer et al., 1994] is able to correctly predict out-of-existence-growth of rough crystal orientations during kinetic faceting of spherical initial shapes. This so called kinetic faceting is also observed if anisotropic kinetics is coupled to diffusion in two dimensions [Yokoyama and Kuroda, 1990]. Only recently it was however claimed that three dimensional faceted growth of snow crystals instead requires the mechanism of equilibrium faceting, i.e. an anisotropy in the surface energy [Barrett et al., 2012].

Aggregated snow inherits growth properties of the single ice crystals it is comprised of but even for single crystals it is tricky to measure the prefactors in the growth law [Libbrecht, 2003]. In addition, the evolution of snow is complicated by the complexity of the microstructure. Time lapse tomography [Pinzer et al., 2012, Schleef and Löwe, 2013, Calonne et al., 2015] has become a powerful tool to monitor the evolution of snow microstructure under conditions of temperature driving and mechanical stress. In principle, these techniques are perfectly suited to track the growing interface and measure variations of the local normal velocity $v_n(x)$, which gained interest only recently due to the new opportunities.

The aim of this paper is to present a method for the analysis and validation of local growth laws in snow. We present estimates of the local ice-air interface velocity obtained from the analysis of time lapse experiments of snow subject to constant temperature gradient and isothermal conditions. From the three-dimensional structures obtained by micro-computed tomography, we track the ice-air interface of snow by means of image analysis. For a quantitative comparison, we derive three simple growth laws. For temperature gradient conditions we follow the classical approach by Shreve [1967] used for vapor bubbles. For isothermal conditions we compared a diffusion limited growth law which includes the Gibbs-Thomson effect to a kinetics limited growth law. All three approaches are applicable to bicontinuous microstructures and involve closed form expression which are solely determined by local temperatures, temperature gradients and geometrical characteristics of the interface such as mean and Gaussian curvatures. Local temperatures are computed by pore scale FE simulations and the geometrical features are estimated from the reconstructed interface. The order of magnitude of measured interface velocities is similar to the theoretical models. However, we observe large scatter, which we discuss in view of experimental uncertainties, limitations of image analysis, and missing theoretical insight.

The paper is organized as follows. In Sec. 2.2 we present the necessary theoretical background and governing equations for coupled heat and mass transport and the implications on interface dynamics. In Sec. 2.3 we provide a summary of the image analysis tools and develop an interface tracking method based on VTK algorithms. The results are presented in Sec. 2.4 and discussed in Sec. 2.5.

2.2 Theoretical Background

Snow metamorphism is driven by coupled transport of heat and mass. A common starting point for modeling is a description in terms of stationary, coupled diffusion equations at the pore scale with appropriate boundary conditions at the ice-vapor interface. In the following description we essentially follow Kaempfer and Plapp [2009], and Calonne et al. [2014b].

The (gravimetric) water vapor density ρ_v in the pore space is governed by the stationary diffusion equation

$$\nabla^2 \rho_v = 0 \quad (2.1)$$

which must be equipped with boundary conditions at the ice-air interface. The first boundary condition is given by mass conservation at the interface. The diffusive vapor flux must balance the flux caused by the solid-vapor interface which advances (by growth) with a normal velocity v_n , viz

$$(\rho_v - \rho_i)v_n = D_v \nabla \rho_v \cdot \mathbf{n}|_+ , \quad (2.2)$$

where ρ_i denotes the ice density, D_v the diffusion constant for water vapor, and $|_+$ the limit of approaching the interface from the vapor phase. The orientation of the normal vector field \mathbf{n} on the interface is chosen to be directed from ice to vapor. Besides mass conservation, the water vapor concentration satisfies a non-equilibrium “growth law” at the interface which is a local constitutive equation relating v_n to deviations from the saturation (equilibrium) density $\rho_{v,s}$. The growth law must be understood as an Onsager relation, which relates a flux to a thermodynamic force. Including the Gibbs-Thomson effect, the growth law can be written as

$$\rho_v = \rho_{v,s}(T) \left(1 + d_0 H + \frac{1}{\alpha v_{\text{kin}}} v_n \right) \quad (2.3)$$

It includes the influence of the mean curvature H on the equilibrium vapor density over a flat surface, $\rho_{v,s}(T)$, which depends on local temperature T . The capillary length $d_0 = \gamma a^3 / k_B T$ is related to the surface energy γ , the Boltzmann constant k_B , temperature and the mean intermolecular spacing a of water molecules in solid ice. The product αv_{kin} describes the attachment kinetics at the interface in terms of the condensation coefficient α and the velocity scale v_{kin} [Libbrecht, 2005]. The magnitude of αv_{kin} discerns between diffusion and kinetics limited growth. The diffusion limited case corresponds to $\alpha v_{\text{kin}} \gg v_n$ where the Robin boundary condition, (2.2) and (2.3), reduces to a Dirichlet condition.

The equilibrium vapor density $\rho_{v,s}$, as the primary driver for crystal growth from vapor, depends

on temperature T . Therefore, the vapor field is coupled to the temperature field which is governed by the static heat equation

$$\nabla^2 T = 0 . \quad (2.4)$$

To solve this, a boundary condition at the interface is required. It describes the continuity of the heat flux through two conducting media with different conductivities κ_a for vapor and κ_i for ice [Carslaw and Jaeger, 1986]. Neglecting the latent heat contribution due to phase changes [Calonne et al., 2014b] the boundary conditions reduce to

$$\kappa_i \nabla T \cdot \mathbf{n}|_- = \kappa_a \nabla T \cdot \mathbf{n}|_+ , \quad T_a = T_i. \quad (2.5)$$

The approach of using stationary diffusion equations (2.1) and (2.4) is commonly justified by a time scale analysis of the diffusion and growth processes [Libbrecht, 2003]. The relevant time scale of variations in the vapor density can be roughly estimated by the diffusion time $\tau_{\text{diff}} = \ell^2/D_v$, with ℓ being a characteristic size of the microstructure. This has to be compared to the time it takes to grow the ice crystal with size ℓ , which is $\tau_{\text{growth}} = \ell/v_n$. The ratio of these two scales is called the Peclet number which is given by $p = \tau_{\text{diff}}/\tau_{\text{growth}} \approx 10^{-7}$. Here we used $v_n \approx 10^{-9}$ m/s and $\ell \approx 10^{-3}$ m as typical values, which are rough estimates from the data in this work and similar to the values used in Kaempfer and Plapp [2009]. Thus the vapor density is adjusting itself by diffusion much faster than the crystal growth which justifies the assumption of stationarity.

In practice, the coupled equations (2.1) and (2.4) in the presence of a moving interface can be solved only numerically for complex geometries, e.g. via the phase field approach [Kaempfer and Plapp, 2009]. Even such a computationally demanding approach still does not take into account the anisotropy in kinetic coefficient and surface energy as a generalization of (2.3). The anisotropy gives rise to faceting and branching which are key to obtain realistic, three dimensional growth morphologies of single ice crystals [Barrett et al., 2012]. This will be likewise relevant for aggregated ice crystals in snow. Due to these complexities, we re-derive simple approximations for the local growth velocities in the next section to provide quantitative means for the comparison with the developed image analysis method.

2.2.1 Temperature gradient dominated growth

To obtain an estimate for the local interface velocity in the presence of a steady, macroscopic temperature gradient we follow the classical example of air bubble migration in ice [Shreve, 1967]. This can be readily generalized to arbitrary geometries to address crystal growth in snow. Therein, it is assumed that the diffusion of water vapor in the pore space is predominantly caused by temperature differences, which affect the equilibrium concentration $\rho_{v,s}$ and in turn

cause vapor fluxes across the pores. The dependence of curvatures is neglected by setting $d_0 = 0$ in Equation (2.3). In this setting, it remains only a one-way coupling between the heat and mass equations: First the temperature equation can be solved for a given microstructure, and afterwards the vapor field can be obtained for a given temperature field.

More precisely, if the temperature gradient is not too large, it is reasonable to linearize the dependence of the saturated vapor density on temperature

$$\rho_{v,s}(T) = \rho_{v,s}(T_0) + \rho'_{v,s}(T_0) (T - T_0) , \quad (2.6)$$

around a reference temperature T_0 where $\rho'_{v,s}(T_0) = d\rho_{v,s}(T)/dT|_{T=T_0}$. Shreve [1967] has implicitly considered $\alpha v_{\text{kin}} \gg v_n$ in (2.3). This corresponds to $\rho_v - \rho_{v,s} \rightarrow 0$, i.e. the interface is in quasi-equilibrium with the ambient vapor. This setting is also used by Pinzer et al. [2012], Brzoska et al. [2008] and is equivalent to a Dirichlet boundary conditions at the ice-vapor interface

$$\rho_v = \rho_{v,s}(T) . \quad (2.7)$$

This boundary conditions implies that the interface velocity is solely determined by the mass conservation condition (2.2) yielding

$$(\rho_i - \rho_v)v_n = D_v \nabla \rho_{v,s} \cdot \mathbf{n}|_+ = D_v \rho'_{v,s} \nabla T \cdot \mathbf{n}|_+ . \quad (2.8)$$

This corresponds to a diffusion-limited problem where interfacial kinetics are ignored. As an advantage, a minimal description for an effective growth law at the interface is obtained which is determined by the local temperature gradient as follows

$$v_n = A \nabla T \cdot \mathbf{n} , \quad (2.9)$$

where the rate coefficient A depends on temperature and is given by

$$A(T) = \frac{D_v \rho'_{v,s}(T)}{\rho_i - \rho_v} \approx \frac{D_v \rho'_{v,s}(T)}{\rho_i} . \quad (2.10)$$

The temperature dependence of ρ' can be parametrized as e.g. given in Kaempfer and Plapp

[2009]. In writing down Equation (2.9), growth velocities vary throughout a sample because they are determined by local temperatures and temperature gradients. This is the generalization to migration of a single bubble, where the temperature gradient is uniform across the bubble [Shreve, 1967] due to the simplicity of the spherical microstructure. The analysis of Equation (2.9) only requires a numerical solution of the temperature field which can be obtained by the Finite element method as e.g. described in Pinzer et al. [2012].

2.2.2 Curvature dominated growth: Diffusion limited case

For isothermal conditions, $T = T_0$ is a solution of Equations (2.4) and (2.5). Curvature differences remain as the only driving force for vapor gradients and the evolution of the interface. For a system of spherical particles, Equations (2.1)-(2.3) are equivalent to the classical problem of Ostwald ripening which has been studied by Lifshitz and Slyozov [1961] and Wagner [1961], and commonly referred to as LSW theory. It provides an analytical solution for the evolution of the interface of spherical particles which mutually interact via a mean-field background concentration determined by the averaged mean curvature \bar{H} . If αv_{kin} is assumed to be much larger than v_n , the boundary condition Equation (2.3) reduces to a Dirichlet condition

$$\rho_v = \rho_{v,s}(T)(1 + d_0 H) \quad (2.11)$$

The application of LSW to snow has been addressed by Legagneux and Dominé [2005], subject to the limitation of microstructures comprising spheres. Some progress for arbitrary microstructures can be made by exploiting that the growth problem defined by Equations (2.1), (2.8) and (2.11) is equivalent to a Cahn–Hilliard phase-field model in its sharp interface limit [Garcke, 2013], which is therefore considered as an equivalent approach to derive properties of LSW-type growth [Wang, 2008]. A mean field approximation for the interface velocity of a bicontinuous system derived from the Cahn–Hilliard equation has been put forward by Tomita [2000], suggesting an explicit expression for the normal velocity

$$v_n = \frac{B}{\lambda} (\bar{H} - H) . \quad (2.12)$$

Here λ is a characteristic cutoff length scale for the diffusion field in the vicinity of an arbitrary interface. This length scale can be defined by the mean and Gaussian curvature H and K to be $\lambda = (2H^2 - K)^{-\frac{1}{2}}$. \bar{H} is the averaged mean curvature. Equation (2.12) is the lowest order approximation for the interface velocity when surface diffusion is neglected. The rate coefficient B is related to the other parameters by

$$B(T) = \frac{D_v d_0 \rho_{v,s}(T)}{\rho_i} \quad (2.13)$$

and also depends on temperature mainly via $\rho_{v,s}(T)$. Note that Equation (2.12) is not exact. It was however used recently also by Fife et al. [2014] to study local growth velocities of Al-Cu microstructures in liquid-solid systems. The coefficients in Equation (2.13) are chosen to be consistent with physical parameters in the latter work. In general, the identification of phase field parameters and sharp interface parameters requires some caution [Kaempfer and Plapp, 2009].

2.2.3 Curvature dominated growth: Kinetics limited case

If the growth is dominated by the kinetics at the interface, $\alpha v_{\text{kin}} \ll v_n$ [Libbrecht, 2005], the vapor diffusion field adjusts reasonably fast and diffusion can be neglected. In this case the ambient vapor density ρ_v in the boundary condition (2.3) can be approximated by the spatially averaged equilibrium density, $\rho_v = \rho_{v,s}(1 + d_0 \bar{H})$. This approach was used by Flin et al. [2003] to predict the evolution of the specific surface area and the mean curvature in snow for isothermal metamorphism. It follows immediately, that the interface velocity is given by

$$v_n = C(\bar{H} - H) , \quad (2.14)$$

with a rate constant C which is related to the coefficients in (2.3) via

$$C(T) = \alpha v_{\text{kin}} d_0 . \quad (2.15)$$

For the kinetics limited case, an alternative justification for (2.14) can again be motivated by the mapping on a phase field formulation. The kinetics limited case of LSW growth is often alternatively addressed within an Allen–Cahn phase field description [Wang, 2008]. If subject to a global conservation constraint (mass conservation) the normal velocity in the sharp interface limit has the form of Eq. (2.14), cf. e.g. [Garcke, 2013]. The same form was obtained by Tomita [2000].

The value for the condensation coefficient α in (2.15) is believed to be in the range $10^{-3} < \alpha < 10^{-1}$ [Kaempfer and Plapp, 2009], though its experimental determination is difficult cf. [Libbrecht, 2003]. For the comparison of the measured C to the theoretical value (2.15) below we will choose $\alpha = 10^{-2}$.

2.3 Methods

In the following section we summarize the methods to measure local crystal growth from experimental time lapse data obtained from μCT . An assessment of the local growth laws Equation (2.12) and Equation (2.9) requires a simultaneous evaluation of curvatures, normal velocities and temperature gradients. Our image analysis is based on the open source library

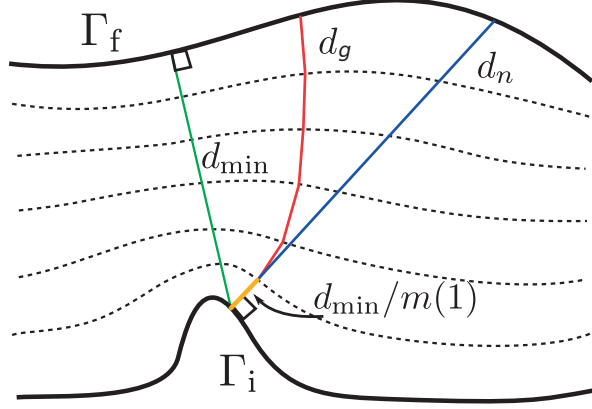


Figure 2.1 – Schematic of the iterative interface tracking. Γ_i and Γ_f represent two consecutive images and the dashed lines the simulated intermediate interfaces. In contrast to d_n , d_{\min} is not perpendicular to Γ_i . d_g is perpendicular to the simulated interfaces.

VTK (www.vtk.org).

2.3.1 Curvatures and normal vectors

After reconstruction via μ CT, the three-dimensional images are available as binary voxel data. On the binary images, the VTK contour filter is applied to obtain a triangulated mesh which represents the ice-air interface. The pseudo normal vectors of the interface are created at every point \mathbf{x} on the mesh by averaging face normals of adjacent triangles by angle weighting. A smoothing filter, `vtkSmoothPolyDataFilter()`, is used to obtain a smooth distribution of the normal vectors. The smoothing is iterated (controlled by the filter parameter number of iteration) until the original voxel structure disappeared. Since the smoothing is controlled locally, it neither preserves the volume nor the surface area of a closed surface and too much smoothing leads to a continuous decrease of the volume and surface area. As a tradeoff, for the analysis of the experiments below the number of iterations was subjectively chosen to be 400 and 200 for isothermal and temperature gradient case, respectively.

Local curvatures are obtained by standard VTK filter acting on the triangulated interface on input. For a discrete, triangulated surface, local curvatures at a point \mathbf{x} can be obtained by standard means as e.g. described in [Sullivan, 2008]. The local mean curvature is calculated by

$$H(\mathbf{x}) = \frac{3}{A_{\Delta}\nu} \sum_{i=1}^{\nu} l(e_i)\alpha(e_i) , \quad (2.16)$$

where e_i are the adjacent triangle edges, ν is the number of edges, $l(e_i)$ the length of the edges in meters, A_{Δ} is the sum of the areas of adjacent triangles and $\alpha(e_i)$ the dihedral angles of the edges. Note that the documentation of the algorithms (www.vtk.org) omits the normalization

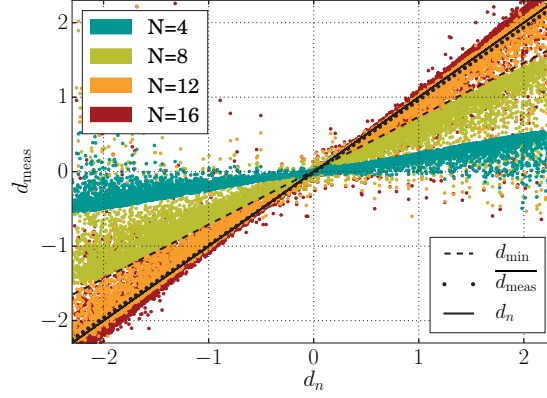


Figure 2.2 – Scatter plot of measured distances d_{meas} as a function of prescribed distances d_n for $N = 4, 8, 12, 16$ iterations. $d_g = \overline{d_{\text{meas}}}(d_f)$, the averaged value for the final iteration ($N = 18$).

A_Δ . The local Gaussian curvature is calculated from

$$K(\mathbf{x}) = \frac{3}{A_\Delta} \left(2\pi - \sum_{i=1}^{\nu} \theta_i \right), \quad (2.17)$$

where θ_i are the angles between the two normal vectors of the neighboring faces of corresponding edges.

2.3.2 Interface tracking

Measuring local crystal growth is related to the evolution of the ice-vapor interface. Normal velocities are estimated from normal distances between points on the interfaces from consecutive time steps. Such a method is not directly available in VTK and therefore developed in the following.

We represent the interface by a discretized, time dependent triangular mesh Γ_t which comprises a collection of a finite number of points evolving from $\mathbf{x} \in \Gamma_i$ to $\mathbf{y} \in \Gamma_f$ by a normal distance $d_n(\mathbf{x})$

$$\mathbf{y} := \mathbf{x} + d_n \mathbf{n}(\mathbf{x}), \quad (2.18)$$

The triangulation is obtained by applying the VTK contour filter to the μ CT voxel data.

VTK provides a method to estimate the minimal distance between two surfaces, this distance is not necessarily normal to the reference surface, as required by Equation (2.9). To this end an iterative procedure is used to estimate the normal distances. It is based on the `vtkDistancePolyDataFilter()`

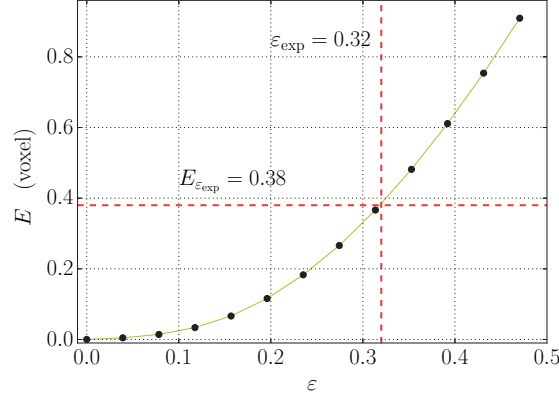


Figure 2.3 – Measured errors E as a function of prescribed growth with corresponding ε . The lower bound for the estimated error $E_{\varepsilon_{\text{exp}}}$ for the temperature gradient experiment are indicated by the dashed red line.

implemented by Quammen et al. [2011] which computes the signed distance measure as proposed by Baerentzen and Aanaes [2005]. The filter measures the minimal distance d_{\min} between two polygonal meshes that represent two consecutive ice-air interfaces. More precisely, for all points \mathbf{x} on interface Γ_i the minimal distance to the next interface Γ_f is calculated via

$$\mathbf{r}(\mathbf{x}, \mathbf{y}) = \mathbf{x} - \mathbf{y} , \quad (2.19)$$

$$d_{\min}(\mathbf{x}) = \pm \min_{\mathbf{y}} |\mathbf{r}(\mathbf{x}, \mathbf{y})| . \quad (2.20)$$

The sign of the d_{\min} is determined by the sign of $\mathbf{r} \cdot \mathbf{n}(\mathbf{x})$. If the time difference between two interfaces is chosen to be very small, the minimal distance approximates the distance in the normal direction. However, experimental data is available only at finite temporal resolution Δt in the order of hours, which leads to a loss of information and a decorrelation of the two consecutive interfaces and thus to a failure of the method. Instead an iterative process is suggested, in which the configurations of the interface between two time steps are guessed by a number N of interfaces Γ_j . A measure for the normal distance d_n is then retrieved using the simulated intermediate interfaces. We start with two interfaces Γ_i at time $t = 0$ and Γ_f a time step Δt later, which are specified by their points \mathbf{x} and normal vectors $\mathbf{n}(\mathbf{x})$. For all points on Γ_i the minimal distances d_{\min} to Γ_f are calculated as described above. Then the interface is moved along the normal vectors by a given fraction $1/m_1$, of d_{\min} , depending on the choice of number of simulated interfaces and the relative distances between them, yielding a new interface Γ_1 . This is done by using the VTK filter WarpByVector(), that moves the surface along the normal vectors with a given measure that can be defined locally. From the newly created interface the

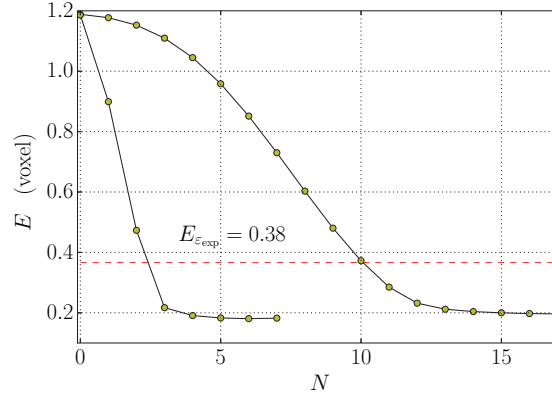


Figure 2.4 – Measured errors E as a function of the number of iterations N . The estimated error corresponding to the minimal distance measurement of the experimental data $E_{\varepsilon_{\text{exp}}}$ is indicated by the dashed red line.

procedure is repeated. The simulated interfaces Γ_j are defined by

$$\mathbf{x}_j = \mathbf{x}_{j-1} + \mathbf{n}_{j-1} d_{\min}(\mathbf{x}_j) / m_j , \quad (2.21)$$

where \mathbf{n}_{j-1} are the normal vectors of interface Γ_{j-1} and $\Gamma_0 := \Gamma_i$. Finally the distances between the two interfaces are estimated by

$$d_n \approx d_g = \sum_{j=1}^{N+1} d_{\min}(\mathbf{x}_j) / m_j , \quad (2.22)$$

with N the number of simulated interfaces and $m_{N+1} := 1$. The procedure can be envisaged as guessing the sequence of two (real) consecutive interfaces Γ_i and Γ_f by intermediate auxiliary interfaces to obtain an improved estimate of the normal distance. Choosing the values for m_j is a trade off between computation time and fraction of points that represent topological inconsistent simulated surfaces. Taking small values for m_j is computationally favorable but increases the number of points that have their relative position changed with respect to their nearest neighbors. This results in negative normal vectors with respect to Γ_i and consequently diverging values for d_g . The points with diverging distances are filtered out by setting a threshold for the distances. The difference between d_{\min} , d_g and d_n is illustrated in Fig. 2.1.

Test case

To test the previously described method a known growth law is applied to a reference interface and the method must recover the prescribed normal distances. To this end a real snow sample

has been used with a prescribed growth law $d_n = c \mathbf{n} \cdot \mathbf{e}_z$, which represents a local, uniaxial field in z -direction where c determines the amplitude.

A scatter plot of the prescribed and measured distances d_{meas} is shown in Fig. 2.2. The error of the algorithm is now calculated as the average difference between prescribed and measured distances

$$E = \frac{1}{M} \sum_x |d_{\text{meas}} - d_n|. \quad (2.23)$$

where M denotes the number of interface points. The error has dimensions of length and must be compared to the typical size of the structure. To compare the performance for different structural sizes we introduce a dimensionless quantity

$$\varepsilon = \frac{1}{A} \int |H d_n| da. \quad (2.24)$$

which is the average prescribed distance d_n weighted by the local mean curvature H . For illustration, increasing c in the prescribed growth law mimics the influence of an increasing time step, which leads to increasing values for ε .

To assess the errors we varied the local growth law d_n by varying the amplitude c , with corresponding ε , and measured the local distances d_{meas} with the minimal distance d_{min} . The errors as a function of ε are shown in Fig. 2.3 and decreases to zero for small ε . Our experiments however always come with a finite time and spatial resolution that leads to an estimated $\varepsilon_{\text{exp}} = \frac{1}{A} \int |H d_{\text{min}}| da$ of 0.32. This estimate is a lower bound since $d_{\text{min}} < d_n$ and actual errors might be higher. To do better than the minimal distance estimation of the normal distances the iterative interface tracking as described above is tested on the snow sample with a prescribed growth corresponding to $\varepsilon = 0.32$. The number of iterations and the divisor m_j together define how fast and how accurate the error is decreasing. In Fig. 2.4 two possible choices for m_i and number of iterations are plotted. The faster the simulated interfaces approach the second interface, the more scatter and the less topological inconsistencies are measured. The results show that the iterative approach reduces the error by at least 45%. To optimize computation time, and limit the number of topological inconsistencies we choose to limit the number of simulated interfaces to seven. As seen in Fig. 2.4, four or five iterations would be sufficient for this particular choice for m_j , but the threshold that cuts away points from the interface with divergent distances works more efficiently if the number of iterations is increased.

2.3.3 Local Temperature Gradients

In addition to purely geometric properties of the image, a Finite Element solution of Equation (2.4) with boundary condition Equation (2.5) is computed to estimate the local temperature gradient

for all voxels in the dataset. According to the growth law Equation (2.9), the temperature gradients must be known in the limit of approaching the interface from the vapor space. This limiting procedure is mimicked by a VTK interpolation filter (ResampleDataSets) which interpolates the temperature field in the pore space “close” to the interface

$$\nabla T(\mathbf{x}) = \nabla T(\mathbf{x} + \epsilon \mathbf{n}(\mathbf{x})) , \quad (2.25)$$

where ϵ is the spatial distance from the interface where the temperature gradient is sampled.

2.3.4 Discerning settling and growth

Estimating growth velocities in snow bears the fundamental difficulty, that the effect of growth cannot be well distinguished from settling effects due to gravity. This is readily illustrated by a hypothetical spherical ice particle, for which the growing interface in a constant temperature gradient (cf. Equation (2.9)) has the same effect as a translation of the particle in the absence of growth. If settling velocities are in the same order of magnitude as growth velocities, it requires a method to correct for the effects of settling. For the temperature gradient experiment the settling is assumed to be small compared to the actual crystal growth, but for the isothermal experiment the displacement fields generally depend on the position in the sample [Schleef and Löwe, 2013]. However, by evaluating only a shallow layer at the bottom of the snow (100 voxels thick) it is reasonable to assume a uniaxial displacement field as a first approximation. In addition, settling effects are minimized at the bottom of the snow. Vertical displacements of the structure are estimated manually. Once the settling rates are known, the μ CT images are translated back, and the remaining differences are interpreted as growth and analyzed by the methods described in the previous section.

2.3.5 Sub voxel sample position corrections

As a result of the experimental setup, the exact location of the sample has a sub voxel uncertainty. This originates from the error in absolute positions of consecutive images in the μ CT scanning procedure. The sample must be repeatedly moved to the scan position for each image acquisition which comes with an uncertainty. It is possible to correct for this uncertainty by measuring the average translation of the entire sample in x and y -direction by

$$\Delta r_{x,y} = \overline{d_n / (\mathbf{n} \cdot \hat{\mathbf{e}}_{x,y})} , \quad (2.26)$$

and translate the data back accordingly. The μ CT sub voxel uncertainty in the z -direction cannot be distinguished from both, settling and crystal growth in z -direction, and is therefore not corrected automatically. Local mechanical deformations play a significant role in the isothermal experiment and give a bias in the correction $\Delta r_{x,y}$. As a consequence the translation rates for

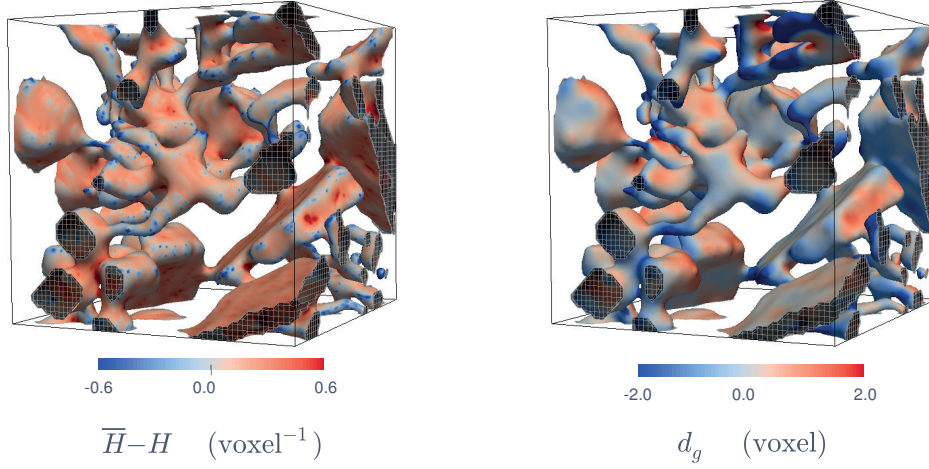


Figure 2.5 – Visualization of the curvature difference $\overline{H} - H$ (left) and the normal distances d_g computed from the interface tracking (right) for the the first sample of the isothermal time-series. The size of the sample is $60 \times 60 \times 60$ voxels.

the isothermal experiment are estimated manually.

2.4 Results

2.4.1 Curvature driven metamorphism

Experimental data

For the isothermal analysis we chose a time series from the isothermal metamorphism experiments described by Schleef and Löwe [2013]. In these experiments, the coupling of isothermal coarsening and densification was investigated within time-lapse experiments with new snow produced from a laboratory snowmaker. For further experimental details we refer to Schleef and Löwe [2013]. To minimize complications emerging from settling, we chose a sample which had very small densification. The temperature of the experiments was -18°C and the time step of the time lapse measurements of $\Delta t = 3$ h. The spatial resolution of the data is $10\,\mu\text{m}$. The size of the dataset is $600 \times 600 \times 100$ voxels, where we have restricted the data in the z -direction to the bottom 100 voxels, such that settling rates are uniform. The initial condition for the experiment were precipitation particles i.e. plates (PPpl) with rounded grains (RGsr) according to Fierz et al. [2009], with a relative high initial value for the specific surface area of $58\,\text{m}^2\text{kg}^{-1}$.

Visual overview

For a qualitative overview of the image analysis data that was used to assess the curvature-driven growth laws Eqs. (2.12),(2.14), we show an example visualization of the key quantities in Fig. 2.5.

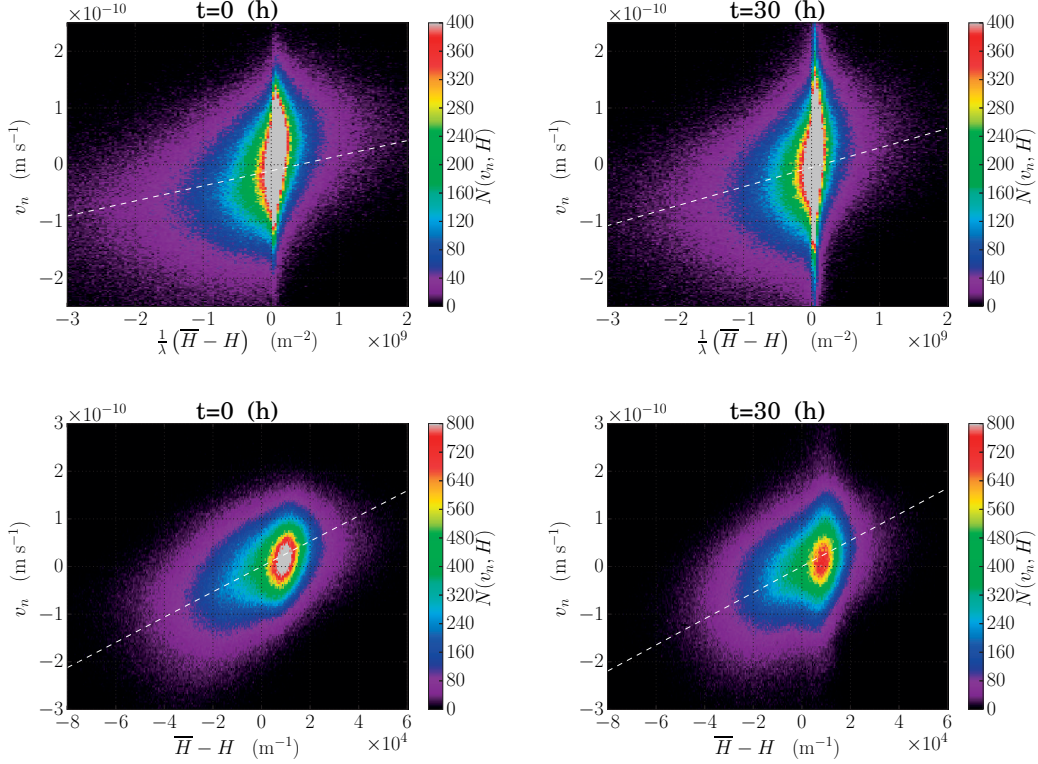


Figure 2.6 – Interface velocities for the isothermal time series. Top: Two-dimensional histograms for v_n and the growth law Equation (2.12) for $t = 0$ h (left) and $t = 30$ h (right). Bottom: Two-dimensional histograms for v_n and the growth law Equation (2.14), for $t = 0$ h (left) and $t = 30$ h (right).

For the first image of the time series, the curvature difference $\bar{H} - H$ is shown (left) together with the normal distance d_n (right), which was obtained from the interface tracking method applied to the first and the fifth image of the time series. Here and for the the analysis below, we did not use consecutive images of the experiment but rather compared every fifth image ($\Delta t = 15$ h) to increase the signal to noise ratio. The normal velocity is then obtained from the normal distance via $d_n = v_n \Delta t$. The images are restricted to a subset of the total data with a size of $60 \times 60 \times 60$ voxels. Further insight into the data is obtained below by a pointwise comparison of v_n with $\bar{H} - H$ as predicted by Eqs. (2.12),(2.14).

Interface velocity histograms

First we assess the diffusion limited growth law Equation (2.14). For every point on the interface we computed the mean curvature H and the velocity v_n and the results are shown in a two-dimensional histogram plot for $t = 0$ and $t = 30$ h, shown in Fig.2.6. A strong signal around zero velocities and zero mean curvatures, and a weaker signal that has a dependency of the velocity on the mean curvature. If we conduct the same analysis for two consecutive images with a smaller time step 3 and 9 hours, the curvature depending signal becomes much weaker. Secondly we compared the velocity to the actual growth law from Equation (2.12), that includes

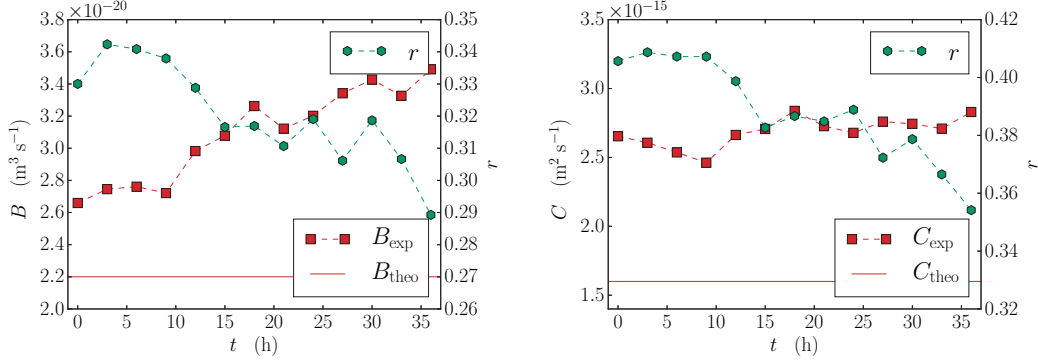


Figure 2.7 – Left: Fitted values B_{exp} from Equation (2.12) with the Pearson correlation coefficient r over time t . For comparison the theoretical value B_{theo} evaluated at -18°C from Equation (2.13) is shown. Right: Fitted values C_{exp} from Equation (2.14) with the Pearson correlation coefficient r over time t . For comparison the theoretical value C_{theo} evaluated at -18°C from Equation (2.15). Note that C_{theo} is only an order of magnitude estimate.

the curvature dependent length scale λ as depicted in Fig. 2.6. Again large scatter is observed at the origin, which is rather symmetric in the velocity distribution.

Time evolution of growth law coefficients

Despite the scatter we have conducted an area weighted least squared analysis on Equation (2.12) and Equation (2.14) to obtain an estimate for B_{exp} and C_{exp} including its evolution over time during the experiment. The results include the sample Pearson correlation coefficients r and are shown in Fig. 2.7 (left). The correlation coefficient r related to B_{exp} is slowly decreasing over time with mean $\bar{r} \approx 0.32$. The estimated values for B_{exp} are consistently higher than the theoretical value B_{theo} . Similarly the estimated values for C_{exp} shown in Fig. 2.7 (right) are consistently higher than C_{theo} , but it should be noted that the order of magnitude of C_{theo} strongly depends on the order of the condensation coefficient α , which for this evaluation is set to 10^{-2} [Kaempfer and Plapp, 2009]. The correlation coefficient r related to C_{exp} , with an average value of $\bar{r} = .39$, is significantly higher, and again shows a decrease over time. These results will be discussed in Sec. 2.5.1.

2.4.2 Temperature gradient driven metamorphism

Experimental data

For the temperature gradient analysis we have chosen a time series from the temperature gradient experiments described by Pinzer et al. [2012], where vapor fluxes during temperature gradient metamorphism were analyzed via time-lapse experiments carried out in a snow breeder. For further experimental details we refer to Pinzer and Schneebeli [2009], Pinzer et al. [2012]. For the present analysis, one time series was chosen with a time step between two images of $\Delta t = 8$ h and a spatial resolution of $18 \mu\text{m}$. The size of the dataset is $190 \times 190 \times 190$ voxels. The average

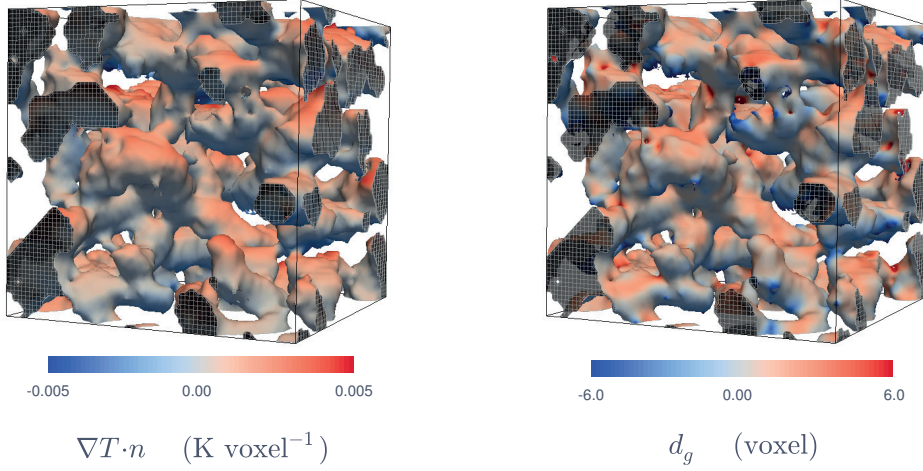


Figure 2.8 – Visualization of the temperature gradient projected on the normal $\nabla T \cdot \mathbf{n}$ (left) and the normal distances d_g computed from the interface tracking (right) for the first sample of the temperature gradient time-series. The size of the sample is $70 \times 70 \times 70$ voxels.

temperature was -7.8°C and the applied temperature gradient was 55 K/m . The initial crystal condition for the experiment was rounded grains, RGLr [Fierz et al., 2009] with an initial specific surface area of $22\text{ m}^2\text{kg}^{-1}$. The uncertainty in the relative x and y positions of two consecutive images was corrected automatically.

Visual overview

Again, we provide a qualitative overview of the image analysis data which is used to assess the growth law Equation (2.9) in Fig. 2.8. The images are restricted to a subset of the total data with a size of $70 \times 70 \times 70$ voxels. For the first image of the time series, the dot product $\nabla T \cdot \mathbf{n}$ of the temperature gradient at the interface with the normal vector is shown (left) together with the normal distances measured by the interface tracking method between first and second time step (right). The normal velocity of the interface is then obtained via $d_n = v_n \Delta t$.

Interface velocity histograms

To assess the relevance of Equation (2.9), we compared local interface velocities with local temperature gradients for all points on the interface at different times in our time-lapse data. The relation between velocities and temperature gradients is shown in Fig. 2.9 in terms of two-dimensional histograms for four equally spaced pairs of consecutive μCT images. In addition, two linear fits are included in Fig. 2.9 to compare the data to the growth law Equation (2.9). The tangent fit represents a linear fit of the histogram data in the small gradient region $-50\text{ K/m} < \nabla T \cdot \mathbf{n} < 50\text{ K/m}$ that describes the linear approximation of the interface velocity for small gradients close to zero. For small velocities, we clearly measure a higher A when

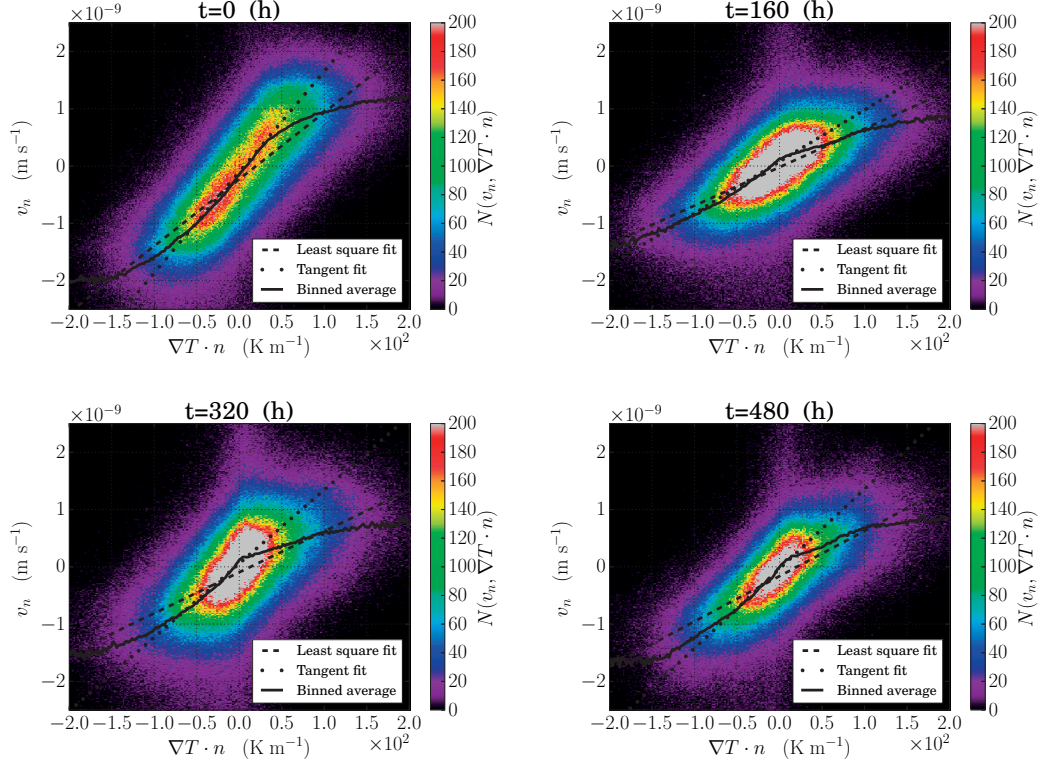


Figure 2.9 – Interface velocities for the temperature gradient time series shown as two-dimensional histograms at four different times for the velocity v_n as a function of local temperature gradients $\nabla T \cdot \mathbf{n}$. Included are two fits for A from Equation (2.9), a weighted least squares and a tangent fit for small $\nabla T \cdot \mathbf{n}$.

compared to a linear fit of all data points. In addition, we have plotted a binned average which gives a measure for the average velocity for a small range of temperature gradients.

Time evolution of growth law coefficients

To assess the temporal evolution of the growth law parameter A , a linear fit and the sample Pearson correlation coefficient r is evaluated for the entire time-lapse experiment and shown in Fig. 2.10 (left). The results show that the measured values of A are close to the theoretical value.

In a next step we analyzed the statistical significance of the presence of a curvature dependent term in the data. To this end we first fitted the data to the coarsening growth law Equation (2.12). The results of the estimates B_{exp} are shown in Fig. 2.10 (right). The correlation coefficients found here are in the same order as for the isothermal experiment (Fig. 2.7, left).

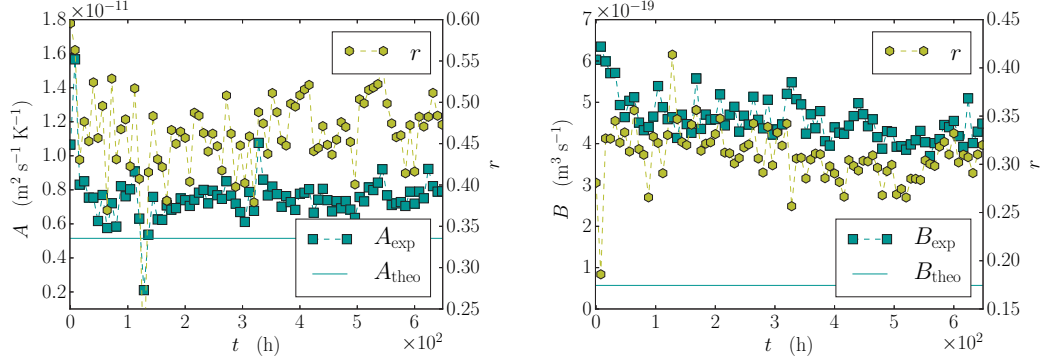


Figure 2.10 – Left: Fitted values A_{exp} from Equation (2.9) with the Pearson correlation coefficient r over time t . For comparison the theoretical value A_{theo} evaluated at -7.8°C from Equation (2.10) is shown. Right: Fitted values for B to Equation (2.12) and the sample Pearson correlation coefficient r over time. For comparison the theoretical value B_{theo} evaluated at -7.8°C from Equation (2.13) is shown.

It is thus reasonable to assess also the linear combination of Equation (2.9) and Equation (2.12)

$$v_n = A \nabla T \cdot \mathbf{n} + \frac{B}{\lambda} (\bar{H} - H) , \quad (2.27)$$

The values for A and B are similar to those obtained before (not shown). However the correlation coefficient changes, depending on which growth law is used. We assessed first r_A from fitting A to Equation (2.9). Secondly we calculated r_B where B is fitted to Equation (2.12). Finally $r_{A,B}$ is computed where A and B are simultaneously fitted in the combined growth law, Equation (2.27). The time-evolution of these coefficients is plotted in Fig. 2.11. The data shows that $\bar{r}_B \approx 0.30$, $\bar{r}_A \approx 0.46$ and $\bar{r}_{A,B} \approx 0.57$.

Sensitivity analysis

Finally, we assess the impact of the limit parameter ϵ introduced in Sec. 2.3.3. To this end we have analyzed the dependence of the growth law coefficient A on ϵ for one sample at $t = 0$. The results are shown in Fig. 2.12. Our choice of $\epsilon = 1.25$ used for the analysis of all the samples then corresponds to the minimal sensitivity of this parameter. The dependence on ϵ will be further detailed in the discussion.

2.5 Discussion

2.5.1 Curvature driven metamorphism

For isothermal metamorphism, we compared the data of the interface velocities obtained by the proposed interface tracking method to two available models: Diffusion limited, Equation (2.12)

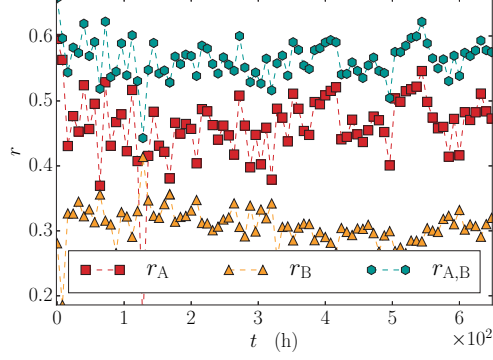


Figure 2.11 – The sample Pearson correlation coefficients over time for various fits. r_A corresponds to the fitted data to Equation (2.9), r_B to Equation (2.12) and $r_{A,B}$ to Equation (2.27).

and kinetics limited, Equation (2.14) growth. For the diffusion limited model (Fig. 2.6, top) the data revealed a large scatter around the origin and the scatter plots are difficult to interpret visually due to the symmetric appearance of the data. However, we observed a weak but consistent correlation (Fig. 2.7, left) when fitting the data to the diffusion limited growth law, Equation (2.12). The fitted values B_{exp} are higher than the theoretical value B_{theo} . If Equation (2.12) was strictly valid, a possible explanation would be an underestimation of the mean curvatures. We recall that our curvature estimates rely on the smoothing parameter, which had to be chosen subjectively and smoothing predominantly reduces always high curvature regions. Another explanation could be the presence of surface diffusion, which is neglected in Equation (2.12). If surface diffusion plays a role it would increase the value for the estimated B_{exp} , since both processes simultaneously contribute to the reduction of mean curvature. As suggested by Tomita [2000], surface diffusion should manifest itself as a higher order correction to Equation (2.12) according to

$$v_n = \frac{B}{\lambda} \left(1 - \lambda^2 \nabla_S^2 \right) [\bar{H} - H] , \quad (2.28)$$

with ∇_S^2 the surface Laplacian. It would be principally possible to also evaluate the growth law (2.28) and discern effects of surface diffusion and bulk vapor diffusion. However this would require a higher quality of the experimental data. The available dataset of new snow with a voxel size $10 \mu\text{m}$ is presently at the limit of resolution, where curvatures can be estimated reliably, as can be seen from Fig. 2.5 (left). The algorithms used by Flin et al. [2005] and Brzoska et al. [2007] use a different smoothing procedure and might give an improved curvature estimation for fresh snow, which would enable the analysis of surface diffusion depending growth laws. Previous results [Löwe et al., 2011] in fact suggest that surface diffusion does play a role at lower temperatures. This is indicated by the exponent governing the power law decrease of the specific surface area, which is closer to $1/4$, indicating surface diffusion, than $1/3$ indicating bulk diffusion.

If the data is fitted to the kinetics limited growth law, Equation (2.14), instead (Fig. 2.6, bottom),

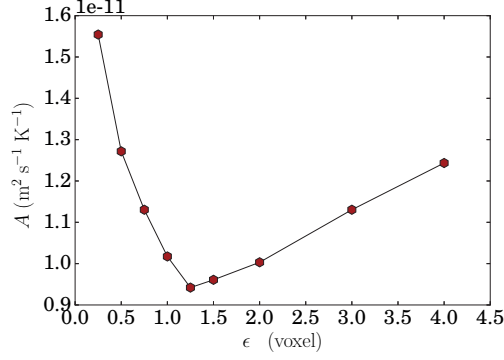


Figure 2.12 – The fitted A to Equation (2.9) as a function of the scale factor ϵ as defined by Equation (2.24).

the correlation coefficient slightly increases (Fig. 2.7, right). Within the limited accuracy of the data we would conclude that kinetics cannot be completely ignored. This is consistent with the dominant snow type (PPpl) of the sample which contains many plate-like structures, where kinetics should play a crucial role on the basal orientations of the plates [Libbrecht, 2005]. The same kinetics limited growth law (Equation (2.14)) was already suggested by Flin et al. [2003], to model isothermal metamorphism.

Our experimental setup bears another uncertainty in the order of one voxel in x, y and z direction (Sec. 2.3.5) which stems from the uncertainty in absolute position. Here the experimental setup developed by Calonne et al. [2015] might improve on that, since the sample is left exactly at the same position during the time-series. Another difficulty encountered here for the isothermal dataset is the necessity of correcting for settling effects. We outlined that the motion of an interface by crystal growth and the motion of the interface by gravitational settling can *a priori* not be discerned. On one hand, large specific surface areas are required to ensure a good signal-to-noise ratio for metamorphism. On the other hand, large specific surface areas increase the effect of settling [Schleef et al., 2014]. In new snow, the crystals experience significant displacements which are larger than the size of the particles. It is difficult to compensate for these effects automatically. In addition the settling is not uniform, as assumed in Equation (2.26) employed here. In the future, an ideal isothermal experiment would comprise artificially compacted, slightly sintered new snow in order to minimize settling effects with reasonably high curvature for significant growth effects.

2.5.2 Temperature gradient driven metamorphism

As a reference model, the obtained data was compared to the generalization of the classical picture from Shreve [1967] for the migration of vapor bubbles in ice. Despite its simplicity, the model is still used as reference to analyze experiments for the migration of vapor bubbles in ice [Dadic et al., 2010]. In the Shreve picture, the local interface velocities are mainly determined by the local temperature gradient in the pore space. For a single sphere, the simplicity of the geometry allows to compute the temperature gradient in the pore space analytically. This can be generalized to complex microstructures, if the temperature gradients are computed

numerically. Our results revealed that, on average, the Shreve picture holds reasonably well for the entire snow structure. Compared to the isothermal case, we found less scatter in the histograms (Fig. 2.9) and estimated values A_{exp} which are in the same order of magnitude as the theoretical value for the entire time series (Fig. 2.10, left). The estimate A_{exp} is fairly constant over time which implies that, on average, the relation between the interface velocities and the temperature gradient constitute an important physical contribution to the growth under temperature gradients. However, the fact that facets and depth hoar emerge during metamorphism clearly indicates that the purely diffusion limited picture (2.9) cannot be strictly valid.

In addition, we analyzed an empirical, linear superposition of the curvature and gradient driven processes, cf. Equation (2.27). Again, the analysis shows a low correlation implying a slight influence of the curvature term, but less pronounced than the temperature gradient contribution (Fig. 2.11). Similar to the isothermal analysis the estimated values for B_{exp} are higher than their theoretical value. The same explanations given for isothermal case are applicable here. A comparison to the isothermal case is however difficult due to the differences in their apparent kinetic regime, temperature, voxel resolution and initial snow type.

The analysis of the temperature gradient growth law has revealed another uncertainty, namely the numerical solution of the temperature field. A subtle source of error originates from the numerical solution on voxel-based images for the proposed method of estimating the temperature gradients in the pore space (Sec. 2.3.3). The temperature gradient must be computed in the limit of approaching the interface from the vapor space in Equation (2.9). This sampling must be close enough to the interface to represent the vapor-space near the interface, but not too close since the sampling will be in the ice-phase for a fraction of the points, resulting in a lower value for the average temperature gradient, and higher values for A . If the sampling were too far away from the interface, temperature gradients decrease, resulting in a higher value for A , as observed in the sensitivity analysis (Fig. 2.12). Accordingly we have chosen the spatial distance ϵ from the interface to be in the order of one voxel, more precisely $\epsilon = 1.25$ which corresponds to the minimum of the sensitivity. The choice and sensitivity of the results on ϵ are closely related to the accuracy of the numerical solution of the temperature distribution at that point. The numerical solution, [Pinzer et al., 2012] implements the two-phase material by a space-dependent, thermal conductivity which changes discontinuously from the ice conductivity κ_i to the air conductivity κ_a at the interface. Theoretically, the interface condition Equation (2.5) should be recovered. An *a posteriori* analysis was made of the interface condition by computing the ratio

$$\frac{\nabla T \cdot \mathbf{n}|_{-}}{\nabla T \cdot \mathbf{n}|_{+}} = \kappa_a / \kappa_i . \quad (2.29)$$

Theoretically the ratio should assume a value of ≈ 0.01 . From the simulations, an average ratio close to 0.125 was found, with significant scatter. This is a clear indication of limited accuracy close to the interface on a voxel mesh. This implies uncertainties of the estimated A up to a factor of 12.5. The origin of this uncertainty is the voxel based Finite Element solution which are commonly used [Pinzer et al., 2012, Löwe et al., 2013, Calonne et al., 2014a] and also

applied here. Apparently, the present case of discontinuous coefficients clearly requires more sophisticated methods [Soghrati et al., 2012] to ensure reasonable accuracy of the solution at the interface.

A crucial aspect of the temperature gradient analysis is the temporal resolution of the time-lapse experiment. The analysis has shown that interface tracking is feasible, but limited by the resolution of μ CT time series. The time difference of eight hours has turned out to be too high to avoid the loss of interface correlations between two consecutive images. The optimal temporal resolution depends on typical sizes of the structure, which could e.g. be assessed by the dimensionless quantity (2.24). The interface dynamics of small features naturally requires a higher temporal and spatial resolution. Consecutive interfaces also become decorrelated during structural re-arrangements triggered by growth under gravity which were occasionally observed. Such a mechanism of “dropping grains” has been observed in Vetter et al. [2010] for isothermal metamorphism. These events contribute to the scatter in the velocity, since dropping structures cannot be registered anymore by the interface tracking.

Overall the temperature gradient analysis is less affected by the influence of settling due to the higher initial density and the faster growth during temperature gradient metamorphism. But in contrast to the isothermal case, where vapor transport and growth are isotropic, here the main growth direction (temperature gradient) and the main settling direction (gravity) have the same direction. An ideal experimental setup would realize a temperature gradient perpendicular to gravity, or at least reverse the direction of the temperature gradient to better discern these effects.

2.6 Conclusions

A first attempt has been made to measure the local interface dynamics of the ice-air interface in snow from μ CT time-lapse experiments and interpret the data in terms of non-equilibrium vapor processes at the pore level. We have developed an interface tracking method for time-lapse experiments and compared the measured normal velocities to the simplest, isotropic diffusion limited and kinetics limited growth models which are applicable to bicontinuous structures. While the growth rates predicted by these models are in the same order of magnitude as the experimental data, a final conclusion about this coincidence is not possible yet. This is due to the large scatter, which was discussed and related to experimental, theoretical and methodological limitations. Given the possible improvements suggested from the analysis, it seems promising to further advance the method, and validate growth laws as required for the upscaling in macroscopic snow modeling.

Acknowledgements

The authors thank Michael Lehning and Martin Schneebeli for stimulating discussions and gratefully acknowledge the careful suggestions from Frederic Flin during the review process. The work was funded by the Swiss National Science Foundation (SNSF), Grant No. 200021_143839.

Relating optical and microwave grain metrics of snow: The relevance of grain shape

3.1 Introduction

Linking physical properties of snow to the microstructure always requires to identify appropriate metrics of grain size. In this regard the two-point correlation function has become a key quantity for the prediction of various properties such as thermal conductivity, permeability and electromagnetic properties of snow [Wiesmann and Mätzler, 1999, Löwe et al., 2013, Calonne et al., 2014b, Löwe and Picard, 2015]. The two-point correlation function carries, in essence, information about a distribution of relevant sizes in the microstructure. For microwave applications, the analysis of two-point correlation functions was already used in the era before micro-computed tomography (μ CT), where thin section data and stereology were employed to obtain the required information [Vallese and Kong, 1981, Zurk et al., 1997, Mätzler and Wiesmann, 1999]. The recently gained interest in two-point correlation functions is mainly driven by available data from μ CT, from which the two-point correlation function can be conveniently estimated. The relevance of the two-point correlation function for microwave modeling originates from the connection between its Fourier transform and the scattering phase function in the Born approximation for small scatterers [Mätzler, 1998, Ding et al., 2010, Löwe and Picard, 2015], or the connection to the effective dielectric tensor via depolarization factors [Leinss et al., 2016].

A common practical way to characterize the two-point correlation function is a fit to an exponential, such that the fit parameter, the so called exponential correlation length ξ , can be used to model the decay of microstructural correlations in snow by a single size parameter. This approach dates back to Debye et al. [1957] in the context of small angle scattering of heterogeneous materials. However the characterization of snow by a single length ξ is only an approximation since the occurrence of multiple length scales [Löwe et al., 2011] are known to play a role, in particular to characterize anisotropy [Löwe et al., 2013, Calonne et al., 2014b]. Despite this caveat, ξ still constitutes the main microstructural parameter for microwave modeling of snow [Proksch et al., 2015a, Pan et al., 2016] when the Microwave Emission Model of layered snowpacks [Wiesmann et al., 1998] is used.

The exponential correlation length is often inferred from measurements of the optical equivalent diameter d_{opt} or, equivalently, from the specific surface area (SSA). This link was established

statistically [Mätzler, 2002] leading to the empirical relation

$$\xi \approx 0.5d_{\text{opt}}(1 - \phi), \quad (3.1)$$

where ϕ is the ice volume fraction. This relation facilitates using the measured optical diameter as the primary input for microwave modeling [Durand et al., 2008, Proksch et al., 2015b, Tan et al., 2015]. However, this link between ξ and d_{opt} can only serve as a first approximation. The numerical prefactor in Eq. (3.1) seems to depend on snow type [Mätzler, 2002] which causes a significant scatter in estimating the exponential correlation length from optical diameter. This poses the question which additional size metric captures variations in grain shape and explains the scatter.

A similar issue of grain shape emerges in the context of optical measurements. Optical properties (e.g. reflectance) can be largely predicted from the optical diameter or SSA [Kokhanovsky and Zege, 2004]. The remaining scatter is commonly attributed to shape [Picard et al., 2009] which influences the absorption enhancement parameter B and the asymmetry factor g^G [Kokhanovsky and Zege, 2004]. The influence of grain shape on B for light penetration was recently addressed and measured by Libois et al. [2013, 2014]. The question remains which additional size metric of the microstructure can be used to capture variations in grain shape and measured scatter in B .

The two examples from microwave or optical modeling above reflect the known fact that the optical diameter as a single metric of grain size is not sufficient to characterize the microstructure for many physical properties. It is thus necessary to account for additional grain size metrics which implement the idea of grain shape. A key requirement for potential, new shape metrics is a well-defined geometrical meaning. Present snowpack models [Vionnet et al., 2012, Lehning et al., 2002] contain empirical shape descriptors such as sphericity [Brun et al., 1992]. An objective definition of these quantities for arbitrary two-phase materials is, however, not possible. New shape metrics should thus ideally seek to replace empirical parameters by an objective, measurable and geometrically comprehensible metric.

One appealing route to define shape is via curvatures of the ice-air interface because curvatures i) have already been used to comprehend snow metamorphism via mean and Gaussian curvatures [Brzoska et al., 2008, Schleef et al., 2014, Calonne et al., 2014a] ii) are natural quantities to assess shape via deviations from a sphere, very close to the definition of sphericity in Lesaffre et al. [1998] and iii) naturally emerge as higher order terms in the expansion of the two-point correlation function [Torquato, 2002]. The latter fact can be used in turn to assess variations of the microwave parameter (ξ) from μ CT images which links back to the aforementioned microwave modeling problem.

Another appealing route to define shape is via chord length distributions because they i) naturally implement the idea of size dispersity and ii) have recently been put forward by Malinka [2014] to derive closed-form expressions for the averaged optical properties of a porous medium. Again, the latter fact can in turn be used to assess variations in the optical parameters (g^G, B) from μ CT images which links back to the aforementioned optical modeling problem.

The motivation of the present paper is to investigate and interconnect these two routes of

(objectively) defining grain shape. First, we will assess the curvature-length in the expansion of the two-point correlation function. We will be guided by the question if and how the well-known statistical relation Eq. (3.1) between the exponential correlation length and the optical diameter can be improved by incorporating curvatures. Second, we will characterize the microstructure in terms of chord length distributions in order to make contact to aspects of shape in snow optics. An interconnection between the two routes can be established by an approximate relation between the two-point correlation function and the chord length distribution that was originally suggested in the context of small angle scattering [Méring and Tchoubar, 1968]. By means of this approximate relation we establish various statistical links between all involved size metrics, the moments of the chord length distributions, optical diameter, surface areas, curvatures and the exponential correlation length. The established links imply a microstructural connection between geometrical optics and microwave scattering via size dispersity, which constitutes one aspect of grain shape.

The paper is organized as follows. In section 3.2 we present the theoretical background for the two-point correlation function, the chord length distribution, the connection between both quantities and the governing length scales. In section 3.3 we provide a summary of the μ CT image analysis methods. To provide confidence of the interpretation of the curvature metrics derived from the two-point correlation function, we present an independent validation of these quantities via the triangulation of the ice-air interface. The results of the statistical models are presented in Section 3.4 and discussed in section 3.5.

3.2 Theoretical background

3.2.1 Two-point correlation function and microwave metrics

The interaction of microwaves with snow is commonly interpreted as scattering at permittivity fluctuations in the microstructure which can be described by the two-point correlation function [Vallese and Kong, 1981, Mätzler, 1998, Ding et al., 2010, Löwe and Picard, 2015]. The two-point correlation function can be derived from the spatial distribution of ice and air that is characterized by the ice phase indicator function $\mathcal{I}(\mathbf{x})$, which is equal to 1 for a point \mathbf{x} in ice and 0 for \mathbf{x} in air. From that, a covariance function can be defined which is often referred to as the two-point correlation function

$$C(\mathbf{r}) = \overline{\mathcal{I}(\mathbf{x} + \mathbf{r})\mathcal{I}(\mathbf{x})} - \phi^2. \quad (3.2)$$

In the following we disregard anisotropy by stating that $C(r)$ only depends on the magnitude of $r = |\mathbf{r}|$. To interpret snow with this approach, an average over different coordinate directions must be carried out.

The value of the two-point correlation function $C(0) = \phi(1 - \phi)$ is simply related to the volume fractions of ice ϕ and air $(1 - \phi)$. Therefore, often only the normalized two-point correlation function

$$A(r) = C(r)/C(0) \quad (3.3)$$

is used, (see Fig. 3.1b). Since $A(r)$ must decay from $A(0) = 1$ to zero for $r \rightarrow \infty$, the two-point correlation function is often described by an exponential form

$$A(r) = \exp(-r/\xi), \quad (3.4)$$

in terms of the exponential correlation length ξ . This single length scale empirically characterizes the decay of $A(r)$.

For small arguments r , rigorous results for the decay of the correlation can be inferred since the expansion of $A(r)$ can be interpreted in terms of geometrical properties of the interface. According to Torquato [2002], the expansion for an isotropic medium reads

$$A(r) = 1 - \frac{r}{\lambda_1} \left[1 - \frac{r^2}{\lambda_2^2} + \mathcal{O}(r^3) \right] \quad (3.5)$$

in terms of the length scales λ_1, λ_2 . The first order term

$$\frac{1}{\lambda_1} = - \left. \frac{d}{dr} A(r) \right|_{r=0} = \frac{s}{4\phi(1-\phi)}, \quad (3.6)$$

is the slope of the two-point correlation function at the origin and can be expressed in terms of the interfacial area per unit volume s [Debye et al., 1957]. The size metric λ_1 is one of the most fundamental lengths scales for a two-phase medium and referred to as the *Porod length* in small angle scattering, or *correlation length* in Mätzler [2002]. We will adhere to Porod length here to clearly distinguish λ_1 from the exponential correlation length ξ . The metric λ_1 can be also related to the SSA, defined as the surface area per ice mass (m^2kg^{-1}), or in turn to the equivalent optical diameter d_{opt} of snow via

$$\lambda_1 = \frac{4\phi(1-\phi)}{s} = \frac{4(1-\phi)}{\rho_i \text{SSA}} = \frac{2(1-\phi)}{3} d_{\text{opt}} \quad (3.7)$$

with ρ_i representing the density of ice. The last equality is obtained when the definition of $d_{\text{opt}} = 6/\rho_i \text{SSA}$ is inserted (see Mätzler [2002]).

For a two-phase material with a smooth interface, the second order term $\sim r^2$ is missing in the expansion Eq. (3.5) and the next non-zero term is the cubic one with a prefactor $1/\lambda_1\lambda_2^2$. Here the length scale λ_2 has a geometric interpretation in terms of interfacial curvatures and is therefore referred to as the curvature length hereafter. As originally shown by Frisch and Stillinger [1963], the following identity holds

$$\frac{1}{\lambda_2^2} = \lambda_1 \left. \frac{d^3}{dr^3} A(r) \right|_{r=0} = \frac{1}{8} \left(\overline{H^2} - \frac{\overline{K}}{3} \right) \quad (3.8)$$

in terms of the average squared mean curvature $\overline{H^2}$ and the averaged Gaussian curvature \overline{K} . The quantity λ_2^{-2} is proportional to the orientationally averaged normal curvature of an interface [Tomita, 1986].

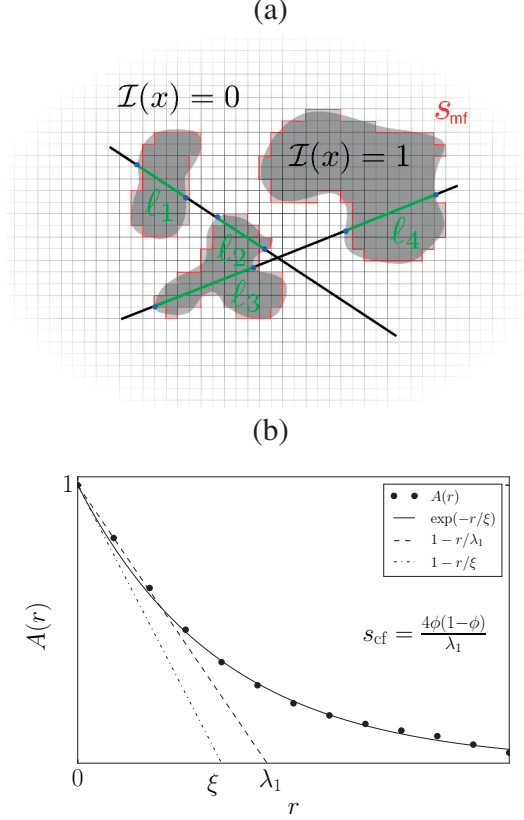


Figure 3.1 – a) Illustration of the chord lengths obtained from an ice sample. The mean chord length is defined as the average length of the green line lengths. A stereological approach [Underwood, 1969] to calculate s is to count the number of blue dots per unit length. The estimation for s_{mf} is given by the red contour. b) Illustration of the two-point correlation function $A(r)$ and the method obtaining an estimate for the Porod length λ_1 to get s_{cf} by fitting the slope at the origin, and the exponential correlation length ξ by fitting $A(r)$ to $\exp(-r/\xi)$ over a larger span.

3.2.2 Chord length distributions and optical metrics

In snow optics the microstructural characterization within radiative transfer theory [Kokhanovsky and Zege, 2004] commonly involves a single metric, the optical diameter. An interesting approach for geometrical optics in arbitrary two-phase media was recently put forward by Malinka [2014]. Thereby, the microstructure is taken into account by the chord length distribution of a medium which can be unambiguously defined for arbitrary two-phase random media [Torquato, 2002]. Chord lengths in an isotropic medium are defined as the lengths of the intersections of random rays through the sample with the ice phase, as illustrated in the schematic in Fig. 3.1a. The chord length distribution $p(\ell)$ of the ice phase denotes the probability (density) for finding a chord of length ℓ .

In contrast to the Born approximation for microwaves, where the microstructure enters as the Fourier transform of the two-point correlation function, the theoretical approach [Malinka, 2014] relates the key optical quantities (absorption, phase function, asymmetry-factor) to the Laplace

transform of the chord length distribution $p(\ell)$ which is denoted by

$$\hat{p}(z) = \int_0^\infty d\ell p(\ell) e^{-z\ell} \quad (3.9)$$

with Laplace variable z . For small z , the Laplace transform can be approximated by the expansion

$$\hat{p}(z) = 1 - \mu_1 z + \frac{\mu_2}{2} z^2 + \mathcal{O}(z^3), \quad (3.10)$$

where μ_i denotes the i -th moment of the chord length distribution, viz

$$\mu_i = \int_0^\infty d\ell \ell^i p(\ell). \quad (3.11)$$

Hence, within the approach from Malinka [2014], the optical response of snow can be systematically improved by successively including higher moments of the chord length distribution. According to Malinka [2014], the Laplace transform has to be evaluated at $z = \alpha$, with the absorption coefficient $\alpha = 4\pi\kappa/\lambda$. Here λ is the wavelength and κ the imaginary part of the refractive index of ice. It is generally sufficient [Malinka, 2014] to retain only a few terms in Eq. (3.10). It is straightforward to show [Underwood, 1969] that the first moment, i.e, the mean chord length μ_1 is given by

$$\mu_1 = \frac{4\phi}{s} = \frac{\lambda_1}{1-\phi} = \frac{2}{3}d_{\text{opt}} \quad (3.12)$$

and thus related to the surface area per unit volume s from Eq. (3.6), or the optical diameter d_{opt} via Eq. (3.7). Therefore, in lowest order, the Laplace transform Eq. (3.9) only contains the Porod length or specific surface area of snow. The next order correction involves the second moment μ_2 for which no geometric interpretation has been hitherto given for arbitrary two-phase random media.

For known chord length distribution, all optical quantities (phase function, single scattering albedo, etc) can be directly computed from Malinka [2014]. To make contact to other approaches e.g. Libois et al. [2013] and discuss our results for the chord lengths in light of shape, an expression of the absorption enhancement parameter B is required within the framework of Malinka [2014] which is derived in Appendix 3.7. From these expressions we can assess the relative importance of the μ_2 correction to the optical diameter μ_1 .

3.2.3 Connection between chord lengths and the Porod length and the curvature-length

Following the previous two sections, a link between optical and microwave metrics of snow thus requires to establish a link between two-point correlation functions and chord length distributions. To this end we employ a relation between the two-point correlation function and chord length distribution that was put forward in the early stages of small angle scattering [Mering and Tchoubar, 1968] to interpret the scattering curve in terms of particle properties. In the present

notation the relation can be written as

$$p(\ell) = \mu_1 \frac{d^2}{d\ell^2} A(\ell), \quad (3.13)$$

which was also used by Gille [2000].

Although Eq. (3.13) is only valid under certain assumptions which will be discussed in section 3.5, it has already some non-trivial implications that can be exploited for the subsequent analysis. As a first consistency check of the approximation Eq. (3.13), we can compute the first moment of the chord length distribution from Eq. (3.11) for $n = 1$, by inserting Eq. (3.13) and integrating by parts. This yields $\mu_1 = \mu_1 A(0)$ which is correct by virtue of Eq. (3.3). As a next step, we aim at an expression for the second moment of the chord length distribution in terms of interfacial curvatures by using Eq. (3.11) for $n = 2$. Again, inserting Eq. (3.13) and integrating by parts yields

$$\mu_2 = 2\mu_1 \int_0^\infty A(r) dr = 2\mu_1 f(\phi, \lambda_1, \lambda_2, \dots). \quad (3.14)$$

Though f is an unknown function here, this link shows that the chord length metric μ_2 must be somehow related to the two-point correlation function metrics λ_1 and λ_2 . In section 3.4 we will statistically investigate the dependence of f on its arguments.

3.3 Methods

3.3.1 Data

For the following analysis we used an existing μ CT dataset of 3D microstructure images described and used in Löwe et al. [2013] for a thermal conductivity analysis and Löwe and Picard [2015] for a comparison of microwave scattering coefficients. All samples were classified according to Fierz et al. [2009] as described in the supplement of Löwe et al. [2013]. The data set comprises 167 different samples including two time series of isothermal experiments, four time series of temperature gradient metamorphism experiments and a set of 37 individual samples. In total, the set includes 62 samples of depth hoar (DH), 54 of rounded grains (RG), 33 of faceted crystals (FC) 10 of decomposing and fragmented precipitation particles (DF), 5 of melt forms (MF) and 3 of precipitation particles (PP).

3.3.2 Geometry from two-point correlation functions

Obtaining the normalized two-point correlation function $A(r)$ from a μ CT image can be conveniently done by using the Fast Fourier Transform (FFT) as e.g. described in Newman and Barkema [1999]. The FFT is typically used for performance issues to evaluate the convolution integral Eq. (3.2) since direct methods can be very slow. The spatial resolution of the two-point correlation function depends on the voxel size Δ of the μ CT image which ranges from 10 to 50 μm .

Since the snow samples in the data set are anisotropic [Löwe et al., 2013], the normalized two-point correlation function is first obtained in the x, y and z direction and then averaged arithmetically over the three directions i.e, $A(r) = (A_x(r) + A_y(r) + A_z(r)) / 3$.

From the normalized two-point correlation function two types of parameter fittings are performed. First, the exponential correlation length ξ is obtained by fitting the μ CT data to the exponential form Eq. (3.4). Technically, we estimated the inverse parameter k by least-squares optimization of the model $A(r) = \exp(-kr)$ to the data in a fixed range of $0 < r < 50\Delta$. An illustration of this method is shown in Fig. 3.1b. In the following we denote by ξ the inverse of the optimal fit parameter $\xi := 1/k$. Secondly, we estimated the expansion parameters λ_1 and λ_2 of the two-point correlation function by a least-squares regression to the expansion Eq. (3.5). Technically, we fitted $A(r) = 1 - k_1 r(1 - k_2 r^2)$ in the fixed range of $0 < r < 3\Delta$ which determines the derivatives at the origin. We denote by λ_1^{cf} and λ_2^{cf} the inverse of the optimal fit parameters $\lambda_1^{\text{cf}} := 1/k_1$ and $\lambda_2^{\text{cf}} := 1/k_2$. The superscript is added to discern these two-point correlation function based estimates from those presented in the next section for a validation. The influence of resolution and anisotropy to the estimates of λ_1 and λ_2 is discussed in section 3.5.

3.3.3 Geometry from triangulations

To confirm the geometrical interpretation of λ_1^{cf} and λ_2^{cf} we use an alternative and independent method to estimate these parameters by measuring the surface area and the local curvatures with a VTK-based image analysis as described in chapter 2. In short, a triangulated ice-air interface is obtained by applying the VTKContour filter. After this step, the interface still resembles the underlying voxel structure. Therefore, in a second step the triangulated interface is smoothed by applying the VTKSmoothing filter which involves a smoothing parameter S which is the number of iterations a Laplacian smoothing on a mesh is repeated. For further details we refer to chapter 2.

3.3.4 Accuracy of surface area and curvatures estimates

The measured total surface area is obtained by integrating (summing) the surface area of the triangles over the surface and the estimate λ_1^{vtk} which naturally depends on the smoothing parameter. A comparison of the triangulation and the two-point correlation function based length scale is shown in Fig. 3.2 (middle row). A higher value of the smoothing parameter implies a lower surface area (caused by shrinking of the enclosed volume upon smoothing) and in turn higher estimates for λ_1^{vtk} . Using higher smoothing also results in a higher variance in the data. This is likely due to filtering of small perturbations in the surface causing the individual samples to react differently.

It is illustrative to note that even without smoothing for $S = 0$ the obtained triangulated surface is still different from the voxel surface s_{mf} , which is obtained by the union of ice-air transition faces in the voxel based image (as illustrated by the red contour in Fig. 3.1a). The quantity s_{mf} is one of the four Minkowski functionals and can be computed by standard counting algorithms [Michielsen and Raedt, 2001]. For isotropic systems, and statistically representative samples, the relation between the surface obtained from the two-point correlation function $s_{\text{cf}} = 4\phi(1 - \phi)/\lambda_1^{\text{cf}}$

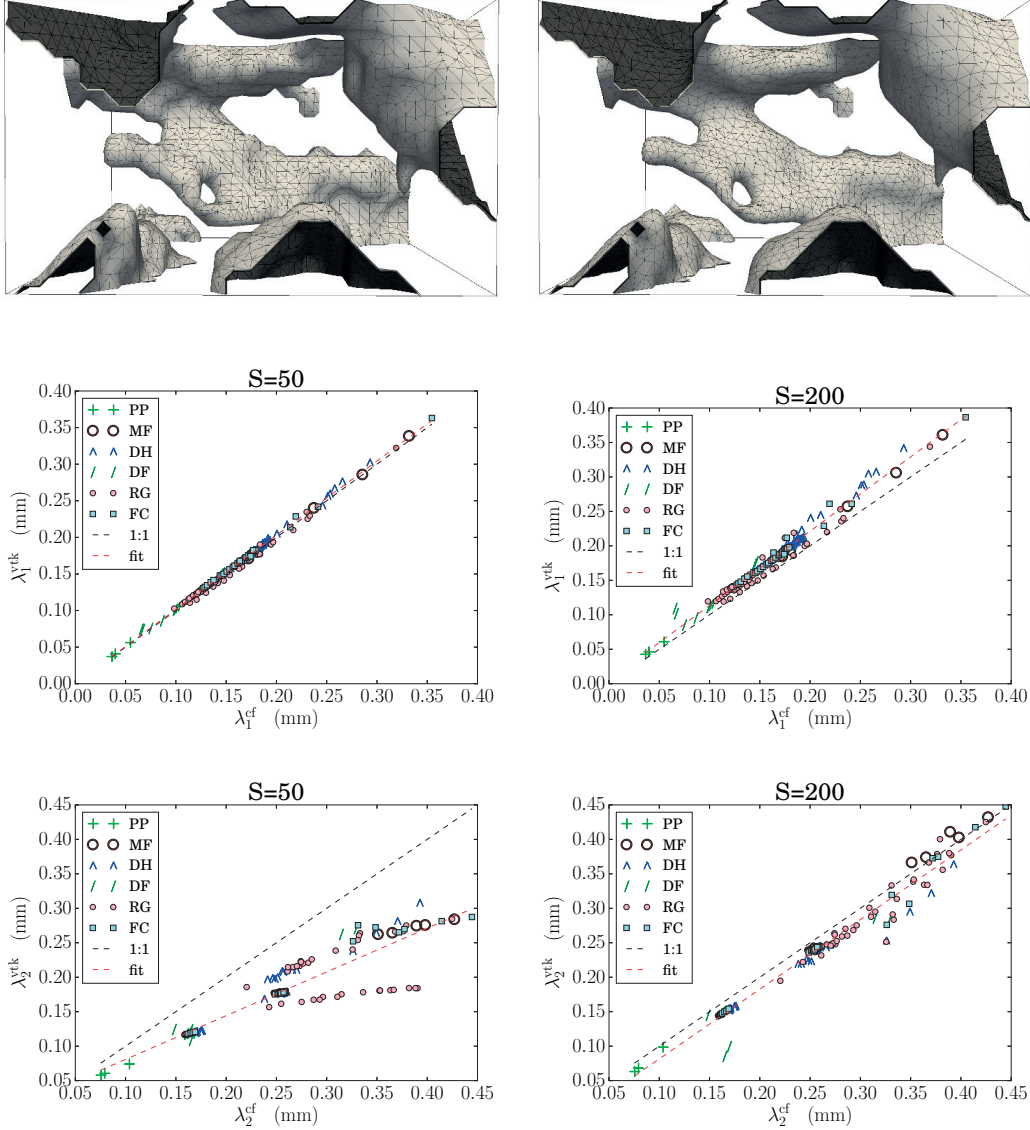


Figure 3.2 – Comparison between smoothing parameter $S = 50$ (left) and $S = 200$ (right). Top: Representation of the triangulated surface of a subsection of a snow sample. Middle: Scatter plots of the Porod length λ_1^{cf} versus λ_1^{vtk} , including a fit (red dotted line). Bottom: Scatter plots of the curvature-length λ_2^{cf} versus λ_2^{vtk} , including a fit (red dotted line).

and the Minkowski functionals is known to be $s_{\text{cf}} = 2s_{\text{mf}}/3$ as discussed in Torquato [2002, p. 290].

An estimate for the curvature-length λ_2^{vtk} is obtained from the VTKCurvature filter on the triangulated ice-air interface yielding local values for mean and Gaussian curvature which can be integrated to compute λ_2^{vtk} via Eq. (3.8). The comparison of the triangulation based curvature-length and the two-point correlation function based curvature length is shown in Fig. 3.2 (bottom row). Again, λ_2^{vtk} depends strongly on the smoothing parameter S . The value $S = 200$ performed best by comparing the value λ_2^{cf} to λ_2^{vtk} , see Fig. 3.2 (bottom row). The deviations from the 1:1 line are caused by the overestimation of the curvatures by the remaining

steps in the triangulation from the underlying voxel-based data, and is thus negatively correlated with the size of the structures and the resolution. In the end, we chose a smoothing parameter $S = 200$ that is, on average, acceptable for all involved samples.

Overall, the comparison provides reasonable confidence that the geometrical interpretation of the two-point correlation function parameters is correct, though uncertainties inherent to the smoothing operations must be acknowledged. In the following we solely use the quantities derived from the two-point correlation function, viz. $\lambda_1 = \lambda_1^{\text{cf}}$ and $\lambda_2 = \lambda_2^{\text{cf}}$ where the superscripts are omitted for brevity.

3.3.5 Chord length distribution

To compute the ice chord length distribution from the binary images, *all* linear lines through the sample in all three Cartesian directions $\beta = x, y, z$ are considered and *all* ice chords were measured and binned to obtain direction dependent counting densities $n^\beta(\ell)$. Here $n^x(\ell)$ denotes the total number of chords in x direction which have length ℓ . For a binary CT image, ℓ can take integer values $0 < \ell < L_x$ which are restricted by the sample size $L_x = N_x \Delta$ and the voxel size Δ of the image. The mean chord length and other moments μ_i are then computed from

$$\mu_i = \frac{1}{\sum_{\ell, \beta} n^\alpha(\ell)} \sum_{\ell, \beta} \ell^i n^\beta(\ell). \quad (3.15)$$

3.3.6 Statistical models

The main part of the following analysis comprises statistical relations between the length scales derived from the chord length distribution and the two-point correlation function in section 3.2. In total, we will consider a few statistical models that first relate the exponential correlation length ξ and μ_2 to the geometrical length scales λ_1 and λ_2 and second, relate ξ to μ_1 and μ_2 . We will start with a one-parameter statistical model and compare the results to the two parameter models. We will assess and compare the quality of the fits with the adjusted correlation coefficient R^2 .

3.4 Results

3.4.1 Relating exponential correlation length to the Porod length and curvature-length

As a starting point for the statistical analysis we revisit the empirical relation

$$\xi = 0.75\lambda_1, \quad (3.16)$$

which is equivalent to Eq. (3.1) by virtue of Eq. (3.7), as suggested by Mätzler [2002]. To this end we fitted ξ and λ_1 and obtained an average slope of 0.79 with a correlation coefficient of $R^2 = 0.733$, shown by the green dashed line in Fig. 3.3a. In the next step we fitted the same

data to include an intercept parameter

$$\xi = a_0 + a_1 \lambda_1. \quad (3.17)$$

Here the adjusted correlation coefficient, accounting for the inclusion of extra parameters, is $R^2 = 0.731$ and the parameters are given by $a_0 = 5.93 \times 10^{-2}$ mm, $a_1 = 0.794$, with very low p -values ($p < 5 \times 10^{-4}$) for the intercept and the slope ensuring the significance of the parameters of the fit. The order of magnitude of the intercept a_0 is negligible. To understand the remaining scatter we have plotted the residuals $\xi - (a_0 + a_1 \lambda_1)$ versus the curvature-length λ_2 as shown in Fig. 3.3b. The correlation coefficient is given by $R^2 = 0.644$ and suggests that including the curvature lengths can improve Eq. (3.17). For an overview, this and all other statistical models will be listed in Table 3.1.

In the next step we include the curvature-length λ_2 where we fitted the exponential correlation length ξ to the model

$$\xi = b_0 + b_1 \lambda_1 + b_2 \lambda_2. \quad (3.18)$$

The results are shown in Fig. 3.3c. Here we find an improvement compared to Eq. (3.17). The correlation coefficient is $R^2 = 0.922$ and the fit parameters are given by $b_0 = 1.23 \times 10^{-2}$ mm, $b_1 = 1.32$ and $b_2 = -3.85 \times 10^{-1}$. The p -values are very small for all coefficients b_i . The order of magnitude of the improvement can already be roughly estimated from the ratio of the prefactors b_1 and b_2 .

3.4.2 Connection between chord length distributions and two-point correlation functions

To relate the chord length metrics to the Porod length and the curvature-length, we first assessed the relation between the chord length distribution $p(\ell)$ and the two-point correlation function $A(\ell)$ as suggested by Eq. (3.13). To this end we compared the chord length distribution obtained directly from the μ CT image (cf. section 3.3.5) with the prediction of Eq. (3.13) via the two-point correlation function for a few examples of different snow types. The results are shown in Fig. 3.4. The selected snow samples are the same as those used in Löwe and Picard [2015, Fig. 8 and Fig. 9]. Qualitatively, the characteristic form (i.e, single maximum), the location of the maximum, and the width of the distribution are correctly predicted by Eq. (3.13). On the other hand, there are obvious shortcomings, such as the oscillatory tail for the RG example when the chord length distribution is derived via Eq. (3.15). We will revisit these characteristics in the discussion.

3.4.3 Relating the second moment of the chord length distribution to the Porod length and the curvature-length

Using the previous results we can derive an approximate relation between the second moment of the chord length distribution and the interfacial curvatures. To motivate a statistical model, we

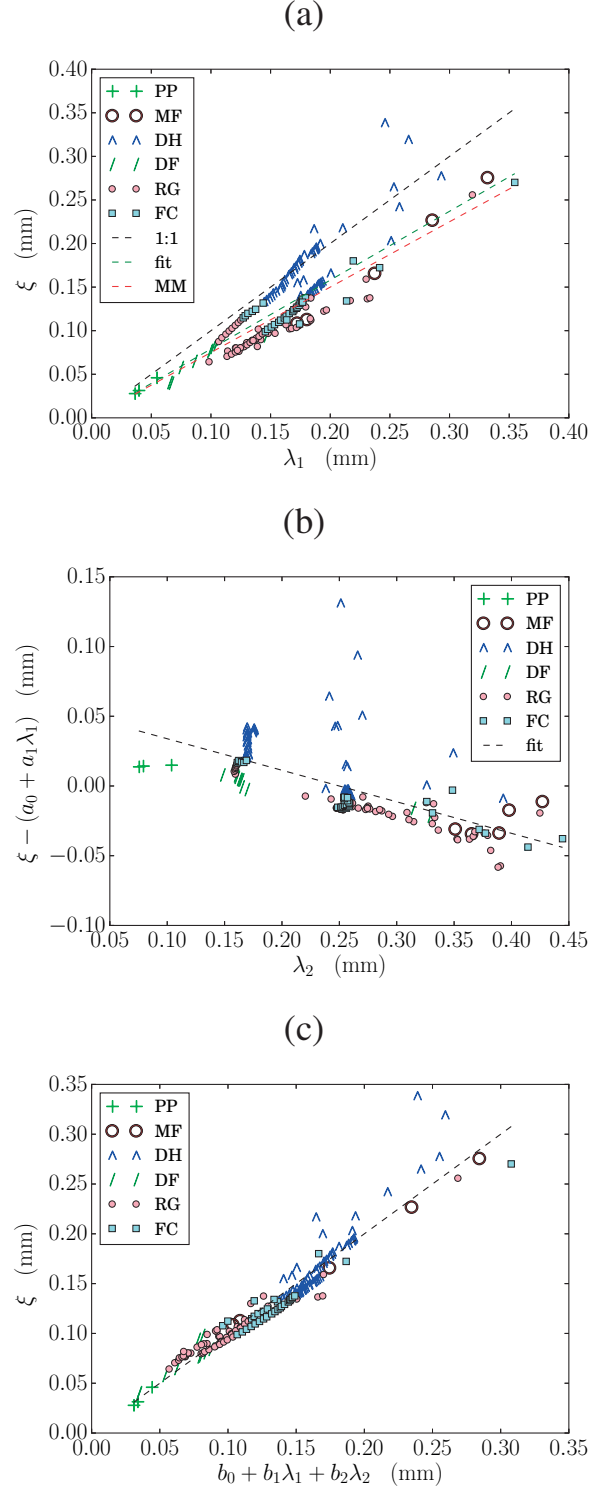


Figure 3.3 – Scatter plots of a) the exponential correlation length ξ versus the Porod length λ_1 . A linear fit is plotted in green. Additionally the prediction of Eq. (3.16) (MM) is plotted in red. b) The residuals of ξ and the statistical model Eq. (3.17), versus the curvature-length λ_2 . c) The statistical model Eq. (3.18) predicting ξ depending on the Porod length λ_1 and the curvature-length λ_2 .

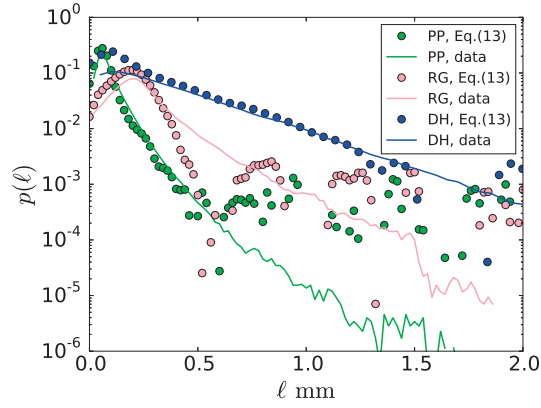


Figure 3.4 – Comparison of the chord length distributions computed from Eq. (3.13) (symbols) and by direct analysis of the μ CT data (solid-line) for three examples of snow types (PP, RG and DH).

start from Eq. (3.14),

$$\frac{\mu_2}{2\mu_1} = f(\phi, \lambda_1, \lambda_2, \dots). \quad (3.19)$$

We investigate the dependency of the function f on parameters λ_1, λ_2 and ϕ of this expression by successively including λ_1, λ_2 and ϕ in a statistical model. In a first step we approximate f by a statistical model including only λ_1

$$\frac{\mu_2}{2\mu_1} = l_0 + l_1 \lambda_1. \quad (3.20)$$

The optimal parameters for model Eq. (3.20) are $l_0 = -2.40 \times 10^{-2}$ mm and $l_1 = 1.25$, with negligible p -values and a correlation coefficient of $R^2 = 0.898$. The results are shown in Fig. 3.5a.

In view of the inclusion of the curvature-length λ_2 , we analyzed the residuals of the previous statistical model and plotted them as a function of λ_2 (Fig. 3.5b). The correlation coefficient ($R^2 = 0.295$) is small but including λ_2 in the analysis further improves the fit. The respective statistical model

$$\frac{\mu_2}{2\mu_1} = n_0 + n_1 \lambda_1 + n_2 \lambda_2 \quad (3.21)$$

yields optimal parameters $n_0 = -3.95 \times 10^{-3}$ mm, $n_1 = 1.50$ and $n_2 = -2.46 \times 10^{-1}$ with a correlation coefficient $R^2 = 0.949$. The p -value for the intercept n_0 is 0.36. For n_1 and n_2 the p -values are again very low.

We have heuristically found a possibility of improving Eq. (3.21) even further. This was achieved by including a factor $(1 - \phi)$ on the left-hand side. More precisely, we tried

$$\frac{(1 - \phi)\mu_2}{2\mu_1} = q_0 + q_1 \lambda_1 + q_2 \lambda_2 \quad (3.22)$$

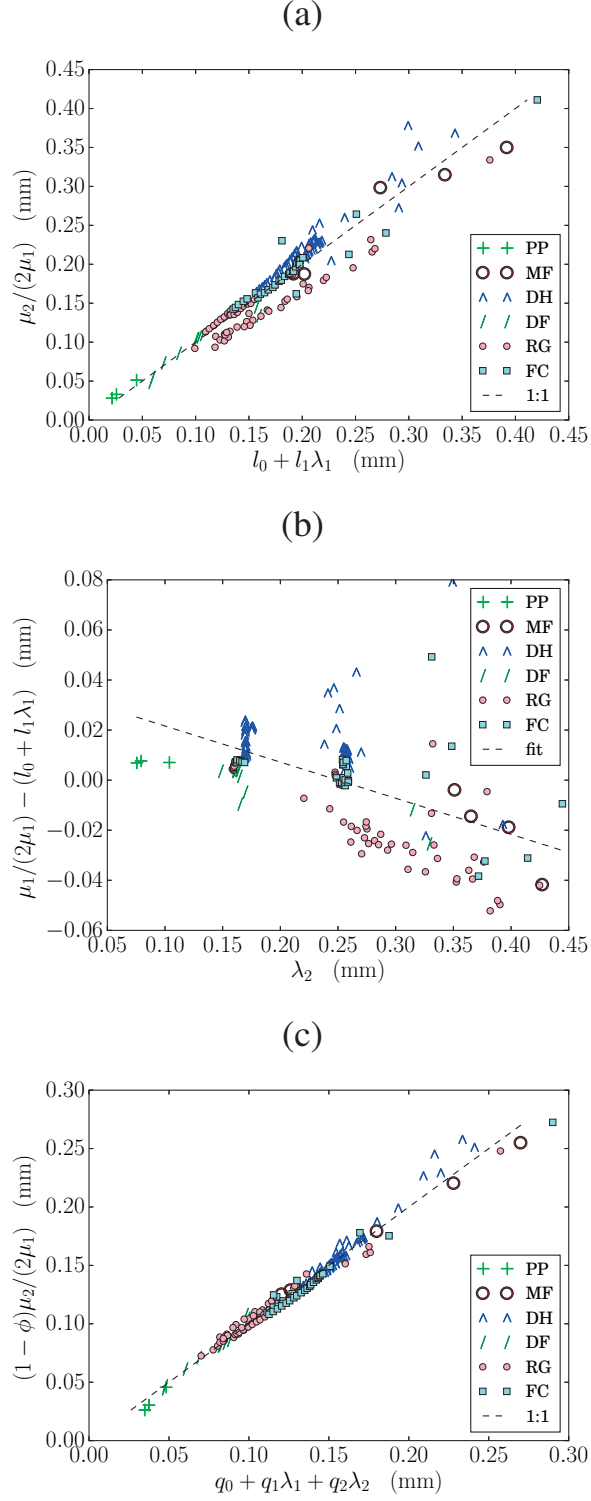


Figure 3.5 – Scatter plots of a) the statistical model see Eq. (3.20) predicting $\mu_2/2\mu_1$ depending on the Porod length λ_1 , b) the residuals of $\mu_2/2\mu_1$ and the statistical model Eq. (3.20) versus the curvature-length scale parameter λ_2 , c) the statistical model predicting $(1 - \phi)\mu_2/2\mu_1$ (see Eq. (3.22)) depending on the Porod length λ_1 and the curvature-length λ_2 .

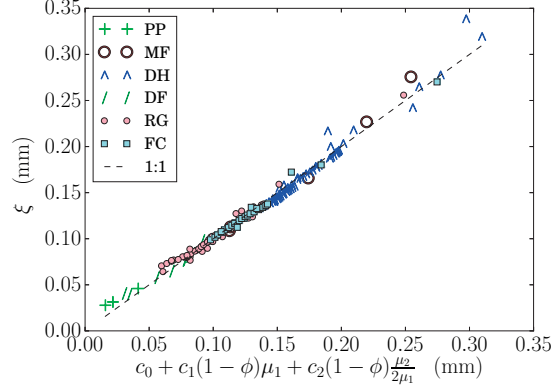


Figure 3.6 – Scatterplot of the exponential correlation length ξ versus the statistical model Eq. (3.23) that depends on the first and second moment of the chord length distribution, μ_1 and μ_2 .

as a statistical model. Here the optimal parameters are $q_0 = -1.23 \times 10^{-2}$ mm, $q_1 = 1.03$, and $q_2 = -1.98 \times 10^{-1}$. The p -values for all coefficients are negligible and the correlation coefficient is $R^2 = 0.980$. The results are shown in Fig. 3.5c.

3.4.4 Relating microwave metrics and optical metrics

In the previous sections we found a statistical relation between the exponential correlation length ξ and the geometrical lengths λ_1 and λ_2 on one hand and a relation between the first and second moment of the chord length distribution (μ_1 and μ_2) and λ_1 and λ_2 on the other hand. Both findings can be recast into a direct connection between the moments of the chord lengths μ_1 and μ_2 and the exponential correlation length ξ . We express this relation in the statistical model

$$\xi = c_0 + c_1(1 - \phi)\mu_1 + c_2 \frac{(1 - \phi)\mu_2}{2\mu_1}. \quad (3.23)$$

Note that $(1 - \phi)\mu_1 = \lambda_1$ by virtue of Eq. (3.12), which means that we essentially replace λ_2 by $(1 - \phi)\mu_2/2\mu_1$ in the statistical model Eq. (3.18) that relates ξ to λ_1 and λ_2 . We obtained the correlation coefficient $R^2 = 0.985$ for the optimal parameters $c_0 = 9.28 \times 10^{-3}$ mm, $c_1 = -7.53 \times 10^{-1}$, $c_2 = 2.00$. This final relation Eq. (3.23) significantly improves both models Eq. (3.17) and Eq. (3.18).

The summary of all models is given in Table 3.1. To ensure that the inclusion of an additional parameter, e.g. by going from model Eq. (3.17) to model Eq. (3.18), is indeed an improvement, we have employed the Akaike information criterion (AIC) [Akaike, 1998]. The AIC measure allows to discern if the improvement of the correlation coefficient is trivially caused by an increasing number of fit parameters or an actual improvement on the likelihood of the fit due to the relevance of the added parameters. Absolute AIC-measures have no direct meaning, however a decrease of at least $2k$ between two models, where k is the number of extra parameters, implies a statistical improvement. For our case $k = 1$ the difference in the AIC-measure between Eq. (3.17) and Eq. (3.18) is 177 confirming the statistical relevance significance of λ_2 .

Table 3.1 – Summary Statistical Models

model	Eq.(#)	parameters (in order)	(adj.) R^2
$\xi = a_0 + a_1\lambda_1$	(3.17)	5.93×10^{-2} mm, 0.79	0.731
$\xi = b_0 + b_1\lambda_1 + b_2\lambda_2$	(3.18)	1.23×10^{-2} mm, 1.32, -3.85×10^{-1}	0.922
$\xi = b_0 + c_1(1 - \phi)\mu_1 + c_2(1 - \phi)\mu_2/2\mu_1$	(3.23)	9.28×10^{-3} mm, -7.53×10^{-1} , 2.00	0.985
$\mu_2/2\mu_1 = l_0 + l_1\lambda_1$	(3.20)	-2.40×10^{-2} mm, 1.25	0.898
$\mu_2/2\mu_1 = n_0 + n_1\lambda_1 + n_2\lambda_2$	(3.21)	-3.95×10^{-3} mm, 1.50, -2.46×10^{-1}	0.949
$(1 - \phi)\mu_2/2\mu_1 = q_0 + q_1\lambda_1 + q_2\lambda_2$	(3.22)	-1.23×10^{-2} mm, 1.03, -1.98×10^{-1}	0.980

3.4.5 Shape factors g^G and B

As an application of the values obtained for the moments of the chord length distribution we can now compute the “shape diagram” of the optical parameters (g^G, B) suggested in Libois et al. [2013] derived from [Malinka, 2014, Eq. 60], and Eq. (3.27). The results depend on the value of the Laplace transform at the absorption coefficient α , and thus on wavelengths. For most wavelengths in the visible and near infrared regime $\alpha\mu_1 \ll 1$ is small and therefore the Laplace transform Eq. (3.9) can be approximated by a few terms in the expansion Eq. (3.10). Taking typical values for α allows us to estimate the relative importance $\alpha\mu_2/2\mu_1$ of the second-order term compared to the first-order term in the expansion Eq. (3.10). These values are obtained by using the values for κ provided by Warren and Brandt [2008]. The first order $\alpha\mu_1$ and ratio $\alpha\mu_2/2\mu_1$ are calculated for typical wavelengths and shown in Table 3.2. The values and standard deviations denote averages taken over all samples. Wavelengths are selected to match common optical methods, namely $0.9 \mu\text{m}$ [Matzl and Schneebeli, 2006], $1.31 \mu\text{m}$ [Arnaud et al., 2011], and the SWIR wavelengths $1.63 \mu\text{m}$, $1.74 \mu\text{m}$ and $2.26 \mu\text{m}$ used by Domine et al. [2006]. We added the wavelength $2.00 \mu\text{m}$, which is not used by any instrument, but has the highest value for α in this range. Note that for this wavelength $\alpha\mu_1$ is not small and the expansion of the Laplace transform, Eq. 3.10, likely not a good approximation. The standard deviations are high as a result of the variations due to grain type. The lowest values of $\alpha\mu_2/2\mu_1$ are found for fresh snow (PP) and highest for depth hoar (DH) and melt forms (MF).

The values in Fig. 3.7 for g^G and B are computed for wavelength $1.3 \mu\text{m}$ and shown as a scatter plot of B versus $1 - g^G$ similar to Libois et al. [2013]. The range of values for $B \in [1.54, 1.72]$ and $(1 - g^G) \in [0.315, 0.335]$ is within the range $B \in [1.25, 2.09]$ and $(1 - g^G) \in [0.2, 0.5]$ obtained by ray-tracing simulations for different geometrical shapes [Libois et al., 2013]. The variations of the values for different snow types is however very small. To complete the analysis we have computed g^G and B for higher absorbing wavelengths for which the shape signature might be higher, but the expansion of Eq. (3.10), less reliable. The results are averaged over all snow samples and included in Table 3.2.

¹this wavelength is not used for optical measurements

Table 3.2 – Determination of the absorption coefficient α [Warren and Brandt, 2008], the first order, the fraction of the first and second order of Eq. (3.10), and the obtained estimates for B and g^G averaged over all snowsamples, including the standard deviation σ .

wavelength (μm)	α (m^{-1})	$\alpha\mu_1 \pm \sigma$	$\mu_2/2\mu_1\alpha \pm \sigma$ (%)	B	$1 - g^G$
0.90	4.1	0.00094 ± 0.0003	< 0.5	1.71 ± 0.00	0.323 ± 0.000
1.31	1.2×10^2	0.026 ± 0.008	2 ± 1	1.64 ± 0.02	0.316 ± 0.000
1.63	2.0×10^3	0.45 ± 0.14	37 ± 13	0.89 ± 0.20	0.253 ± 0.011
1.74	1.1×10^3	0.24 ± 0.079	20 ± 7	1.19 ± 0.14	0.272 ± 0.010
2.00 ¹	9.4×10^3	2.1 ± 0.68	172 ± 60	-	-
2.26	1.1×10^3	0.25 ± 0.08	20 ± 7	1.14 ± 0.13	0.240 ± 0.010

3.5 Discussion

3.5.1 Methodology

Before turning to the discussion of physical implications of the results, we first address methodological details. Retrieving parameters from μCT images must be taken with care. In addition to the uncertainties related to filtering and segmentation pointed out by Hagenmuller et al. [2016], the present method also requires to discuss the interface-smoothing for the validation of λ_1 and λ_2 , the image resolution, and the anisotropy of the samples.

Geometrical interpretation

The present analysis and cross-validation of the curvature metric imposes requirements on the smoothness of the interface. The subtle influence of the smoothing parameter on the surface area s and averaged mean and Gaussian curvatures \overline{H} and \overline{K} is apparent from Fig. 3.2. Naturally, $\overline{H^2}$ is most sensitive to smoothing. We found a competing performance of λ_1 and λ_2 with the smoothing parameter when comparing the triangulation based estimates with the two-point correlation function based values. The agreement for the surface area seems to be best with smoothing parameter $S = 50$. In contrast, more smoothing is required to obtain an agreement for the curvature-length. This higher sensitivity on the smoothing parameter is reasonable, since curvatures are defined by surface gradients which are more sensitive to a smooth mesh representation than the surface area. The competing behavior is caused by the smoothing filter, which neither preserves the volume nor the surface area of the enclosed ice upon smoothing iterations. This causes the drop in agreement for λ_1 in Fig. 3.2 (left, middle) with increased smoothing. As a remedy, more sophisticated smoothing filters could be used which, for example, ensure the conservation of the enclosed volume [Kuprat et al., 2001]. Such problems could be partly avoided by computing normal vector fields and curvatures directly from voxel-based distance maps [Flin et al., 2005]. A detailed comparison of all these different methods however, is beyond the scope of this paper. In contrast to λ_1 and λ_2 , the interpretation of first and second moments of the chord length distribution, μ_1 and μ_2 , is rather straightforward, where μ_1 is directly related to the optical diameter d_{opt} , and μ_2 is a measure of the variations of this size metric.

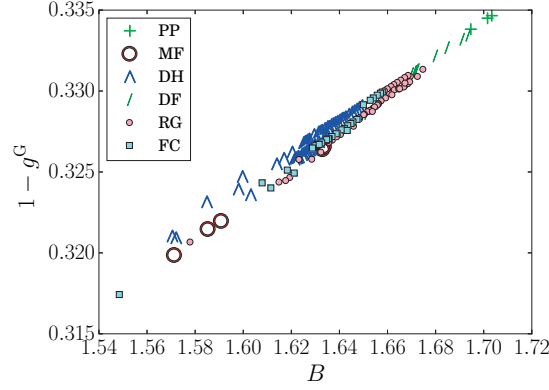


Figure 3.7 – Scatterplot of the asymmetry factor g^G and the optical shape factor B evaluated for the refractive index at wavelength $\lambda = 1.3 \mu\text{m}$.

Resolution

Resolution plays an important role in obtaining estimates for λ_1 and λ_2 . For a μCT measurement the resolution is commonly chosen appropriately depending on snow type. While fresh Snow (PP) is typically reconstructed with $10 \mu\text{m}$ voxel size, melt forms (MF) and larger particles have larger voxel sizes of $35 \mu\text{m}$ or $54 \mu\text{m}$. Since we have obtained λ_1 and λ_2 with two independent methods that agree reasonably well we conclude that the resolution is generally sufficient to estimate the involved length scales. To further confirm that there is no remaining bias with resolution we assessed the ratio $\lambda_2/\text{voxelsize}$. For our data, this ratio is 9.8 on average, with a standard deviation of 2.6 and no systematic difference between small and large voxel sizes, implying that λ_2 can be considered as equally well resolved for all snow samples.

The image resolution plays another important role in the interpretation of the expansion of the two-point correlation function. As pointed out by Torquato [2002], a missing r^2 term is generally equivalent to a smooth interface while discontinuities, like sharp edges, would lead to a second order term. Fresh snow and depth hoar crystals are known to have these discontinuities, at least visually. But it remains questionable if these features can be detected objectively at the micrometer scale from image analysis. In an image, discontinuities are always smeared out, virtually contributing to the third order term.

Anisotropy

The present dataset was previously used to study the anisotropic properties of snow [Löwe et al., 2013]. Therefore it is necessary to elaborate on the impact of anisotropy in the present analysis which exclusively involves isotropic two-point correlation functions. It is important to note that the our analysis does not *assume* isotropy, but it rather includes the orientational averaging in the three Cartesian directions as a part of the method. Such a procedure is principally valid for arbitrary samples. Moreover, also the geometrical interpretation of the quantities remains valid. This was rigorously shown for λ_1 Berryman [1998] which relates the slope of the two-point correlation function at the origin for arbitrary anisotropic structures after orientational averaging

to the surface area per unit volume s . Though we did not find a mathematical proof for the corresponding statement for λ_2 , the agreement of λ_2^{cf} (obtained from the two-point correlation function, orientationally averaged) with λ_2^{vtk} (obtained from direct computation of the interfacial curvatures) strongly suggests its validity. In addition, we assessed that the residuals between λ_2^{vtk} (where anisotropy does not play a role) and λ_2^{cf} are not correlated with anisotropy ($R^2 = .026$).

Overall, we are confident that the method can be applied to arbitrary anisotropic samples to provide orientationally averaged length scales with the correct geometric interpretation with acceptable uncertainties due to image resolution.

3.5.2 Linking size metrics in snow

Accepting the methodological uncertainties, we shall now discuss our findings of the statistical analysis and their relevance for the interpretation of snow microstructure.

Including size dispersity to estimate the exponential correlation length

By construction, the exponential correlation length ξ must be understood as a proxy to characterize the entire two-point correlation function with a single length scale. This single length scale contains signatures of both; properties that dominate the behavior of the two-point correlation function for small arguments (λ_1 and λ_2) and other properties that dominate the tail-behavior of the two-point correlation function for large arguments.

To discuss the statistical relations we will start with recovering Mätzler’s model [Mätzler, 2002]. This statistical model covers a relation between the exponential correlation length and the optical grain size, or in their nomenclature: the correlation length. Mätzler’s model predicts the slope to be $a_1 = 0.75$, which is an average of $a_1 = 0.8$ for depth hoar and $a_1 = 0.6$ for other snow types. This is consistent with our finding $a_1 = 0.79$ since we have many depth hoar samples in the data set, suggesting that grain shape has a direct influence on the statistical relation. This influence was made quantitative by including the curvature-length to the statistical analysis, resulting in the statistical model Eq. (3.18) (Fig. 3.3c). The quantitative improvement on the statistical model Eq. (3.16) by using Eq. (3.18) is given by the increase in the correlation coefficient from $R^2 = 0.733$ to $R^2 = 0.922$.

In addition we established a new statistical relation Eq. (3.23) between ξ and the moments of the chord length distribution, μ_1 and μ_2 . This model performs even better when the correlation coefficient $R^2 = 0.985$ is taken as a quality measure. We confirmed that the inclusion of an additional parameter in Eq. (3.18) and Eq. (3.23) indeed improves on eq. (3.16), by employing the Akaike information criterion (AIC) measure [Akaike, 1998].

All proposed statistical models show an improvement to Eq. (3.1) indicating that at least two different length scales λ_1 and λ_2 or μ_1 and μ_2 are required to obtain a reasonable prediction of the exponential correlation length. While λ_1 and μ_1 are both trivially related to the optical radius via Eq. (3.7) and Eq. (3.12), the two other size metrics μ_2 or λ_2 are the origin of performance increase.

This seems surprising at first sight. Why should local aspects of the interface (λ_1 and λ_2) determine the non-local decay of structural correlations (ξ)? To illustrate our explanation for this finding, we resort to a particle picture and consider a dense, random packing of monodisperse hard spheres. For such a packing, the particle “shape” is trivial and fully determined by the sphere diameter d , which determines the slope of the two-point correlation function at the origin. However, also particle positions and thus the decay of correlations is fixed by d . This becomes obvious from the representation $C(r) = nv_{\text{int}}(r) + n^2 v_{\text{int}}(r) * h(r)$ for the two-point correlation function for such a system at number density n [Löwe and Picard, 2015]. In this representation, the spherical intersection volume v_{int} and the statistics of particle positions $h(r)$ both depend on d . Now imagine that each sphere is deformed by a hypothetical, volume-conserving re-shape operation to an irregular, non-convex particle, which is still located at the center of the original sphere. Due to re-shaping, the parameter $\overline{H^2}$ would increase. After the re-shape, neighboring particles would overlap (on average), since their maximum extension must have been increased compared to the sphere diameter. To recover a non-overlapping configuration, all particle positions must be dilated. The latter, however, also affects the tail of the two-point correlation function. This is exactly what we observe: the “shape of structural units” in snow, as exemplified by $\overline{H^2}$ is always correlated with the “position of the structural units” in space. We note that this particle analogy has clear limitations and only serves here to illustrate the rather abstract statistical relations between different length scales. Snow remains a bi-continuous material where individual particles cannot be distinguished.

Overall, we conclude that both, λ_2 or μ_2 can be used to significantly improve estimates of ξ when compared to optical diameter based estimates.

Linking moments of the chord length distributions to Porod and curvature-length

Hitherto no geometrical interpretation for the second moment μ_2 of the chord length distribution was known. Our results suggest an empirical relation, Eq. (3.22), that involves the two geometrical length scales λ_1 and λ_2 . In the following we provide supporting arguments for the link between μ_2 and λ_1 and λ_2 by discussing the relation Eq. (3.13) between the chord length distribution and the two-point correlation function.

The relation Eq. (3.13) was originally raised in the context of small angle scattering long time ago [Méring and Tchoubar, 1968] and later revisited e.g. by Levitz and Tchoubar [1992], revealing two different approximation steps. A first simplification comes from the assumption that consecutive chords on the random ray in Fig. 3.1 are statistically independent. This issue has been discussed in detail also by Roberts and Torquato [1999], who established an exact relation between the Laplace transforms of the two-point correlation function, the chord length distribution, and a surface-void correlation function based on this assumption. Their results however show that for level-cut Gaussian random fields, where this assumption is violated, the prediction of the chord length distribution can be still very accurate. This indicates that assuming independent chords is per se not a serious limitation. Secondly, Eq. (3.13) is actually an approximation for dilute systems which is generally not valid for snow.

To test the range of validity of the relation (3.13) for snow, we have taken three samples and

computed the chord length distribution directly to compare them to the prediction of Eq. (3.13) as shown in Fig. 3.4. An obvious drawback of Eq. (3.13) can be seen for the rounded grains (RG) sample. Due to the quasi-oscillations in the two-point correlation function (cf. Löwe et al. [2011]), $A(\ell)$ and its second derivative assume negative values, which would imply negative values for $p(\ell)$ via Eq. (3.13). This is in contradiction to the meaning of $p(\ell)$ as a probability density and likely a consequence of the assumptions which are not valid for snow. Despite this obvious drawback, Fig. 3.4 shows that Eq. (3.13) yields three, qualitatively consistent results for different snow types where the basic features of the chord length distribution are well predicted: First, it captures the considerable variations of the position of the maximum, the width, and decay of the chord length distribution. Secondly, the relation Eq. (3.13) predicts that the chord length distribution tends to zero for small values i.e. $p(0) = 0$ (as confirmed in Fig. 3.4). This is a direct consequence of a smooth interface as shown in Wu and Schmidt [1971]. Thirdly, it leads to Eq. (3.14), that involves the integral over the two-point correlation function. The latter indicated a connection between μ_2 and λ_1 and λ_2 , which was confirmed quantitatively via Eq. (3.21). Given the assumptions discussed above, it is not surprising that a heuristic improvement could be achieved by including a term $(1 - \phi)$ in Eq. (3.22), since snow is not a dilute particle system and corrections containing ϕ -terms are to be expected.

Overall, our analysis confirms that both approaches to microstructure characterization, via two-point correlation functions (with metrics λ_1, λ_2) or via chord length distribution (with metrics μ_1, μ_2) are not independent. They rather describe, slightly different but interrelated, structural properties which are now discussed in view of grain shape.

3.5.3 Grain shape

Grain shape, a geometrical interpretation

The international classification for seasonal snow on the ground [Fierz et al., 2009] considers grain shape as the morphological classification into snow types. This is motivated by the common but loose perception of shape as the basic geometrical form of constituent particles. It is clear that grain shape remains a vague concept unless it is formulated in terms of quantities which are unambiguously defined on the 3D microstructure.

Local curvatures are often regarded as shape parameters and used to characterize snow on a more fundamental level. The relevance of the mean curvature is described and analyzed in detail in Calonne et al. [2015], where morphological transitions (e.g, faceting) of snow during temperature gradient metamorphism are visible in the distribution of mean curvatures. The present description of grain shape in snowpack models [Lehning et al., 2002, Vionnet et al., 2012] is based on the variance of the mean curvature, by the sphericity parameter as defined by Lesaffre et al. [1998]. There were attempts to measure the sphericity from digital photographs as described by Lesaffre et al. [1998] and Bartlett et al. [2008]. This definition is valid only in two dimensions and therefore difficult to compare directly to their 3D counterparts in Calonne et al. [2015].

It is therefore natural to use objective measures such as the mean and Gaussian curvature \overline{H}

and \overline{K} to quantify shape. Though \overline{K} is computed from local properties of the interface, it has a strict topological meaning due to its relation to the Euler characteristic which is by definition strictly independent of local shape variations of the ice-air interface. The Euler characteristic was e.g. used by Schleef et al. [2014] to characterize microstructural changes during densification. We found however, that the contribution $\overline{K}/3$ in λ_2 from Eq. (3.8) ranges from 1-13% and is on average 3.7 % of \overline{H}^2 . Hence the curvature-length λ_2 is dominated by the second moment \overline{H}^2 , and thus closely related to the variance of an (inverse) size distribution, the distribution of mean curvatures. This indicates the formal similarity to μ_2 which is also a second moment of a size distribution, the chord length distribution. Hence, both metrics can be regarded as accounting for size dispersity in snow.

Overall, we suggest that both parameters, μ_2 and λ_2 can be used to objectively define a grain shape for 3D microstructures which is closely connected to size dispersity and which naturally extends grain size (optical diameter) determining μ_1 or λ_1 . Note that within this definition, grain shape is not a dimensionless parameter. With this perception of shape we now connect back to the original applications of microwave and optical modeling.

Grain shape for microwave modeling

Thus far, the exponential correlation length ξ as a key parameter for MEMLS based microwave modeling (MEMLS) was mainly predicted from the optical diameter. Our conclusions from section 3.5.2 could now be restated: The inclusion of a grain shape parameter, λ_2 or μ_2 improves the prediction of the exponential correlation length significantly. Or, according to the conclusion from the previous section, one may alternatively restate that size dispersity has an influence on microwave properties. This is known from other models than MEMLS, where an influence of polydispersity on the effective grain scaling parameter within DMRT-ML microwave modeling was found [Roy et al., 2013].

This equivalence of shape and size dispersity at the level of two-point correlation functions can be further illustrated by an interesting example. Consider a microstructure of polydisperse spherical particles. The definition of grain shape from the classification [Fierz et al., 2009] would assign a spherical shape to this microstructure, while the averaged squared mean curvature \overline{H}^2 would instead vary depending on the variance of particle radii. As pointed out by Tomita [1986], for low density, such a system of polydisperse spherical particles can always be mapped uniquely onto an assembly of monodisperse but irregularly shaped particles by solving an integral equation, if only the two-point correlation function is considered. Shape can be equivalent to polydispersity, and snow types which are visually very different might still have very similar physical properties. This example also explains why the objective size dispersity parameters λ_2 or μ_2 cannot be mapped onto the classical definition of grain type from Fierz et al. [2009].

Grain shape in geometrical optics

Finally, we turn to the implications of size dispersity or grain shape on geometrical optics within the scope of Malinka [2014] based on chord length distributions.

As pointed out by Malinka [2014], if consecutive chords were statistically independent i.e. a Markovian process, then the obtained distribution would be an exponential, and all optical properties solely determined by the optical diameter (or μ_1). To quantify the deviation from an exponential chord length distributions we calculated the fraction $\mu_2/2\mu_1^2$ which is unity for a exponential chord length distribution. This fraction is on average 0.75 for rounded grains (RG), 0.76 for melt forms (MF), 0.77 for precipitation particles (PP) and defragmented particles (DF), 0.79 for faceted crystals (FC) and the closest value to unity is 0.876 for depth hoar (DH). This implies that the chord length distribution for depth hoar is closest to an exponential, which can be visually confirmed by Fig. 3.4. We reach a similar conclusion for the two-point correlation function where λ_1 is already a fairly good predictor for the exponential correlation length when depth hoar is considered (see Fig. 3.3a). But due to the deviations from an exponential distribution, an influence of shape via μ_2 on the optical properties would be expected according to Malinka [2014].

Using the chord length distributions we were able to calculate the shape factors B and g^G from Malinka [2014] and Libois et al. [2013] in the limit of low absorption where both approaches can be compared. The (B, g^G) shape diagram (cf. Fig 1.(a) in Libois et al. [2013]) in Fig. 3.7 was obtained for wavelength $1.3\ \mu\text{m}$ where the Laplace transform Eq. (3.10) can be approximated by the first and second order. The variations of the absolute values for B, g^G shown in Fig. 3.7 predominantly stem from corrections which are linear in μ_1 (by virtue of (3.28)), while the small, scattered deviations from a perfect straight line are caused by μ_2 . If B and g^G were evaluated for wavelength $0.9\ \mu\text{m}$, the influence of μ_2 would be even smaller. Our results show that the values for B and g^G are exactly within the range that is suggested by ray-tracing simulations for various geometrical shapes for a wavelength of $0.9\ \mu\text{m}$ [Libois et al., 2013], but show a much smaller variation over the entire set of snow samples. Comparing our results to ray-tracing of geometrical shapes is however not straightforward, since the 3D microstructures cannot be mapped on an ensemble of regular geometrical objects.

The predicted values for B (Fig. 3.7) are very similar to the values obtained by experiments [Libois et al., 2014] but show a smaller variation. It should be noted that, as the authors discuss, the correlation between the experimentally obtained B and shape, as defined by Fierz et al. [2009], is statistically not significant and variations might be attributed to shadowing effects relevant at higher densities.

Overall, our analysis indicates a smaller variation of optical properties with shape via μ_2 according to Malinka [2014] when compared other methods. We can only hypothesize potential origins which are connected to the present analysis. A crucial assumption made in the geometrical optics framework [Malinka, 2014] is the statistical independence of the chord length and the consecutive ice-air incidence angle for a ray which passes through a grain. Such an assumption might be progressively violated for lower absorption where a higher number of internal reflections in fact probes this assumption more often. Hence the true effect of shape on B and g^G might be more pronounced than predicted by size dispersity via μ_2 [Malinka, 2014]. Further details on the discrepancies between measurements, simulations and theory remain to be elucidated by combining tomography imaging and shape analysis together with optical measurements and ray-tracing simulations in the future.

3.6 Conclusions

We have analyzed different microstructural length scales (λ_1 , λ_2 and μ_1 , μ_2) of snow samples which were derived from the two-point correlation function and chord length distribution, respectively. All length scales have a well-defined geometrical meaning. While the first order quantities (μ_1 , λ_1) are both related to the mean size (optical equivalent diameter), their higher order counterparts (λ_2 , μ_2) are objective measures of size dispersity present in the snow microstructure.

For the two-point correlation function, the length scale λ_2 is essentially determined by the second moment of the mean curvature distribution. For the chord lengths, μ_2 is the second moment of the chord length distribution. Both quantities naturally extend the concept of mean grain size as covered by the optical equivalent diameter. The statistical relation established between (λ_1 , λ_2 , μ_1 , μ_2) indicates that in practice the two measures of size dispersity can be used interchangeably.

We have argued that size dispersity is one possible route towards an objective definition of grain shape, and thus both quantities (λ_2 , μ_2) can be regarded as measures of shape. Within this interpretation, we found that grain shape or size dispersity significantly improves a widely used statistical model for the exponential correlation length (as a key size metric for MEMLS based microwave modeling).

We have also used this interpretation of shape to assess the so called optical shape factor B which can be related to μ_1 and μ_2 in the framework of Malinka [2014]. The results suggest that size dispersity is only a first, but likely not a complete step to characterize shape for optical modeling.

Overall, defining grain shape via dispersity measures μ_2 or λ_2 provides a clear intersection between microwave modeling of snow (if based on the exponential correlation length) and optical modeling of snow (if based on Malinka [2014]). We do not believe this intersection to be exhaustive: The influence of shape in snow optics likely involves more than size dispersity. And size dispersity is likely not sufficient to explain the full diversity of microwave properties of snow. But the established overlap of relevant microstructure parameters provides a clear quantitative starting point for further improvements.

3.7 Appendix: Optical shape factor B from moments of the chord length distribution

To derive an expression of the optical shape factor B in terms of the moments of the chord length distribution, we start from expression [Libois et al., 2013, Eq. 6] for the single scattering co-albedo

$$(1 - \omega) = B \frac{\gamma V}{2\Sigma}, \quad (3.24)$$

which is related to B , the average volume of a particle V , the average projected area of a particle Σ , and the absorption coefficient γ . This can be recast in terms of the mean chord-length using

[Malinka, 2014, Eq. 6], which yields, adopting the notation of the present paper, the relation

$$(1 - \omega) = B \frac{\alpha \mu_1}{2} \quad (3.25)$$

On the other hand, an expression for the single scattering co-albedo is directly provided by Malinka [2014, Eq. 56]. Inserting [Malinka, 2014, Eq. 29,42,49,18] and re-arranging terms we obtain

$$(1 - \omega) = \frac{T_{\text{out}}(n)}{1 + \frac{T_{\text{out}}(n)}{n^2} \frac{\hat{p}(\alpha)}{1 - \hat{p}(\alpha)}} \quad (3.26)$$

in terms of the real part of the refractive index n , the averaged Fresnel transmittance coefficient $T_{\text{out}}(n)$ (given by Malinka [2014, Eq. 19] in closed form) and the Laplace transform of the chord length distribution $\hat{p}(\alpha)$.

To obtain an expression for B by comparing Eq. (3.25) and Eq. (3.26) it must be noted that both expressions are based on slightly different assumptions. While Eq. (3.24) is meant to be valid only in the limit of low absorption [Libois et al., 2013], Eq. (3.26) is valid for arbitrary values of α . This is reflected by the existence of the limit $\alpha \rightarrow \infty$ in Eq. (3.26), while Eq. (3.25) diverges if B is regarded as a constant which is strictly independent of α . Hence the comparison of Eq. (3.25) and Eq. (3.26) must be limited to small values of $\alpha \mu_1$ in order to obtain an expression for B which can be compared to the results from [Libois et al., 2013]. That said, we equate Eq. (3.25) and Eq. (3.26), take into account an additional factor of 2 between Malinka [2014] and Libois et al. [2013] due to a different treatment of the extinction efficiency, we end up with

$$B = \frac{1}{\alpha \mu_1} \frac{T_{\text{out}}(n)}{1 + \frac{T_{\text{out}}(n)}{n^2} \frac{\hat{p}(\alpha)}{1 - \hat{p}(\alpha)}} \quad (3.27)$$

Complemented by the approximation Eq. (3.10) for the Laplace transform \hat{p} , the expression [Malinka, 2014, Eq. 19] for $T_{\text{out}}(n)$, this yields an expression of the shape factor B in terms of the first and second moments, μ_1 and μ_2 , of the chord length distribution, the real part of the refractive index n and the absorption coefficient α .

To explicitly reveal the correction of B for small α which involves the second moment of the chord-length distribution, we expand Eq. (3.27) around $\alpha = 0$ to obtain

$$B = n^2 \left[1 - (\alpha \mu_1) \left(\frac{n^2}{T_{\text{out}}(n)} - 1 + \frac{\mu_2}{2\mu_1^2} \right) \right] \quad (3.28)$$

3.8 Acknowledgements

The authors thank G. Picard for a constructive feedback on an earlier version of the manuscript and S. Torquato for helpful clarifications on the factor $2/3$ between s_{mf} and s_{cf} . M. Lehning provided valuable suggestions on the statistical methods. The comments from the reviewers Q. Libois and A. Malinka greatly helped to improve the manuscript and to shape the conclusions

of the paper. The work was funded by the Swiss National Science Foundation via Grant No. 200021_143839.

Upscaling ice-crystal growth dynamics in snow: Rigorous modeling and comparison to 4D X-ray tomography data

4.1 Introduction

Snow on the ground is an interesting example of a porous, high-temperature material close to the melting point of ice, where a continuous evolution of microstructure, referred to as snow metamorphism [Colbeck, 1982], is ubiquitous under ambient conditions. The dynamical evolution originates from micro-scales where sintered ice crystals grow collectively from the vapor phase. Ice crystal growth is therefore not only of interest due to the fascinating morphologies of isolated crystals [Libbrecht, 2005, Barrett et al., 2012], it also constitutes the essential ingredient for upscaled material models of snow. There is an increasing demand to move from empirical to first-principles approaches of microstructure evolution to limit uncertainties of snow models in environmental or climate applications.

The prediction of the morphological evolution of snow on the ground is subject to the common difficulty of separation of spatial scales in heterogeneous materials [Torquato, 2002]. Various techniques [Berryman, 2005] can be employed to bridge between microscopic (grain or pore) growth processes and the macroscopic (spatially averaged) scales of interest for continuum modeling. However, snow microstructure evolution is still based on simple geometrical shapes when relating size changes to dominant thermodynamic driving conditions (e.g. Adams and Brown [1982], Colbeck [1983], Legagneux and Dominé [2005]). Existing approaches are based on variants of classical coarsening models [Ratke and Voorhees, 2002] as a multi-particle diffusion problem, mediated by the curvature dependence of the equilibrium vapor pressure in the Gibbs-Thomson boundary condition.

Sphere based approaches are however not satisfying for obvious reasons. The simplistic model geometry reflects by no means the complex, bicontinuous microstructure of snow. Recent advancements [Pinzer et al., 2012, Calonne et al., 2014a, Schleef et al., 2014, Hammonds et al., 2015, Wiese and Schneebeli, 2017] in observing snow microstructure evolution in time-lapse experiments using X-ray micro-computed tomography (μ CT) can not be related to these approaches which hinders full exploitation of advanced morphological observations. Tomography has e.g. revealed that the Euler characteristic is correlated with the evolution of the surface area via the topological evolution upon unidirectional compression [Schleef et al., 2014]. Another study [Calonne et al., 2014a] has shown that the distribution of mean curvatures in snow develops

an asymmetry between growth and sublimation sites as a consequence of growth kinetics. Even though a visual inspection of snow unambiguously demonstrates that kinetic effects play a role Colbeck [1982], it is difficult to quantitatively relate these aspects to averaged morphological properties. In addition, state-of-the-art 3D modeling of growing single crystals has demonstrated the importance of combining vapor and heat diffusion with anisotropic growth laws [Barrett et al., 2012, Demange et al., 2017a]. This insight is presently however completely disconnected from snow continuum modeling. Only a faithful representation of geometry will allow to utilize local thermodynamic aspects of ice crystal growth for terrestrial snow and exploit 4D data of snow evolution for improvements in upscaled snow models.

Apart from snow, the evolution of bicontinuous microstructures is relevant for other materials as well. A fundamental understanding of isothermal coarsening of bicontinuous structures can be obtained from phase field simulations [Kwon et al., 2007] which demonstrated the discriminating power of the joint probability distributions of mean and Gaussian curvature. A key difficulty in bicontinuous systems arises from non-local terms in the growth law which are related to topological changes [Park et al., 2015]. For solidification in Cu-Al composites it has been demonstrated how an interface analysis can be combined with 4D tomography [Fife et al., 2014]. However a full understanding of the coupled evolution of interface parameters in evolving microstructures is still missing and advancements in relating 4D data to rigorous evolution models is still of broader interest.

A common question of upscaling is the choice of parameters for which evolution equations are to be derived. From a thermodynamic view point, upscaled conservation equations for mass and energy in snow [Calonne et al., 2014b] explicitly involve the ice volume fraction and the specific surface area. Hence an appropriate microstructural viewpoint must provide evolution equations at least for these quantities. Often it is however necessary to extend the set of parameters, either as closure for the initial ones, or because there is specific interest in them. Chapter 3 has e.g. shown that the second moment $\overline{H^2}$ of the mean curvature distribution is also of relevance due to its appearance in the expansion of the two-point correlation function. The latter can be related to macroscopic transport properties via bounds [Torquato, 2002], and thus the dynamics of $\overline{H^2}$ allows constraining the evolution of two-point correlations. This has practical consequences e.g. for situations where 3D microstructure observations are not available and the dynamical characterization relies on estimating interfacial shape via small-angle scattering [Micha et al., 1998].

A powerful starting point to microstructure evolution was suggested by Drew [1990] who developed a mathematically rigorous description of the evolution of averaged properties for an evolving interface by starting from differential equations for the local, principal curvatures. The averaged evolution of the surface is determined by the local interface velocity which must be provided as a “constitutive law” as a closure relation. The strength of the approach [Drew, 1990] has been demonstrated e.g. by Fife et al. [2014] and Morel [2007].

The goal of the present paper is to build on Drew [1990] and derive a rigorous upscaling scheme for snow microstructure which can be coupled to upscaling of heat and mass transfer [Calonne et al., 2014b]. This is achieved by volume averaging the time evolution of local geometrical properties of the ice-air interface, which is determined by a normal interface velocity relating crystal growth

to geometrical and thermodynamic quantities. For snow-specific reasons, we generalize Drew [1990] to include a contribution of the interface velocity from mechanical deformation, and include an equation for the second moment of mean curvature. The averaged microstructural properties are governed by partial differential equations valid in a Eulerian frame of reference. We demonstrate the correctness of the equations in the absence of deformations by numerically tracking the interfaces of idealized grains under a prescribed growth law. This test enables to infer the uncertainties originating from the smoothness of the interface. In a next step we apply the same procedure to 4D data of a time-lapse snow metamorphism experiment under a stationary temperature gradient conducted by μ CT. This comparison quantifies the uncertainties of velocities estimates from 4D data, the representation of curvatures and topological effects. Finally, we exploit that independent of velocity measurements, the analytical framework allows to statistically assess the relevance of common closure models. Using Finite Element simulations of heat transfer, we provide evidence that a diffusion limited picture is in contradiction with the experimentally observed evolution of the specific surface area.

The paper is organized as follows. In Section 4.2 we derive the microstructural evolution equations in the general setting. In Section 4.3 we simplify the equations to the situation of absent macroscopic gradients and show the correctness of the equations for idealized grains. In Section 4.4 we apply the same framework to 4D tomography data of snow evolution experiments and discuss the uncertainties. In Section 4.5 we show how the exact model can be used for a statistical assessment of growth laws. The results are discussed in Section 4.6.

4.2 Upscaling of microstructure in snow metamorphism

4.2.1 Preliminaries and notation

We consider snow in a sample volume $V = V_i + V_v$ comprising ice and (vapor-filled) air sub-volumes V_i, V_v separated by an interface Γ with area $A = |\Gamma|$. The microstructure is characterized by an indicator function

$$\mathcal{I}(\mathbf{x}, t) = \begin{cases} 1 & \text{if } \mathbf{x} \in V_i \text{ at time } t \\ 0 & \text{otherwise} \end{cases} \quad (4.1)$$

The dynamical evolution of the indicator function can be inferred from the motion of the ice-air interface which is described by the discontinuous variant [Drew, 1990] of the level-set equation [Sethian, 1999]

$$\frac{\partial}{\partial t} \mathcal{I}(\mathbf{x}, t) + \mathbf{w}(\mathbf{x}, t) \cdot \nabla \mathcal{I}(\mathbf{x}, t) = 0 \quad (4.2)$$

in terms of the total interface velocity field \mathbf{w} . Due to the relevance of both, we allow for a contribution \mathbf{u} from mechanical deformations and \mathbf{v} from crystal growth according to

$$\mathbf{w} = \mathbf{u} + \mathbf{v} \quad (4.3)$$

Here only the growth part can be assumed to be normal to the interface $\mathbf{v} = v_n \mathbf{n}$ in terms of the normal vector \mathbf{n} . Eq. (4.2) is defined in the sense of distributions since $\nabla \mathcal{I}$ is a gradient of a discontinuous function that acts as delta function concentrated on the interface according to

$$\nabla \mathcal{I} = -\mathbf{n} \frac{\partial \mathcal{I}}{\partial n} \quad (4.4)$$

Here $\partial \mathcal{I} / \partial n$ is a 1D delta function in the normal direction. Note, with this definition the normal vector field is oriented from ice to air. The local mean curvature H and the Gaussian curvature, K , are given by the spatial derivatives of the normal vector

$$H = \frac{1}{2} \nabla \cdot \mathbf{n} = \frac{1}{2} (\kappa_1 + \kappa_2), \quad K = \kappa_1 \kappa_2 \quad (4.5)$$

where κ_1 and κ_2 denote the principal curvatures.

4.2.2 Volume and surface averages

The volume average of a function $f(\mathbf{x})$ for $\mathbf{x} \in V$ is defined by

$$\langle f \rangle := \frac{1}{V} \int d\mathbf{x} f(\mathbf{x}) \quad (4.6)$$

A function f can be restricted to the ice or vapor phase via $f_i := f\mathcal{I}$ or $f_v := f(1 - \mathcal{I})$ and the volume-average of f_i can be written as

$$\langle f_i \rangle = \phi \frac{1}{V_i} \int_{V_i} f(\mathbf{x}) d\mathbf{x} =: \phi \langle f \rangle_i \quad (4.7)$$

which defines the intrinsic average $\langle \bullet \rangle_i$ and the ice volume fraction $\phi = \langle \mathcal{I} \rangle = V_i / V$.

Due to the delta-function in the level-set equation, volume-averages of various microstructural quantities reduce to surface averages. For a function g defined on the interface Γ the surface average is defined by

$$\bar{g} := \frac{1}{s} \left\langle g(\mathbf{x}) \frac{\partial \mathcal{I}}{\partial n} \right\rangle = \frac{1}{A} \int_{\Gamma} da g(\mathbf{x}) \quad (4.8)$$

with the surface area element da and s denoting the surface area per unit volume

$$s = \left\langle \frac{\partial \mathcal{I}}{\partial n} \right\rangle = \frac{A}{V} \quad (4.9)$$

Using the notation above we can restate the temporal and spatial averaging theorems. The Reynolds rules [Flanders, 1973] allows interchanging temporal and spatial derivatives, viz $\nabla \langle f \rangle = \langle \nabla f \rangle$. When calculating the time derivative of Eq. (4.6) and exploiting the level-set equation Eq. (4.2) this gives rise to additional surface average terms for time and space derivatives of a phase-restricted functions f_i according to

$$\frac{\partial \langle f_i \rangle}{\partial t} = \left\langle \frac{\partial f}{\partial t} \right\rangle + s \overline{f w_n} \quad (4.10)$$

in terms of the normal component of the interface velocity field w_n , and according to

$$\nabla \langle f_i \rangle = \langle \nabla f_i \rangle - s \overline{f \mathbf{n}} \quad (4.11)$$

These equations are also known by the volume and surface averaging theorems [Whitaker, 1998].

4.2.3 Evolution of the ice volume fraction

The micro-scale ice mass conservation equation can be written as

$$\frac{\partial \rho_i}{\partial t} + \nabla \cdot (\rho_i \mathbf{u}_i) = 0 \quad (4.12)$$

where $\mathbf{u}_i = \mathbf{u}\mathcal{I}$ is the ice deformation velocity field and $\rho_i = \rho\mathcal{I}$ the density, both restricted to the ice phase. Note that $\langle \rho_i \rangle = \phi \rho_{\text{ice}}$ with ρ_{ice} the density of ice.

In principle \mathbf{u} must be determined by a micro-scale mechanical treatment (force balance and constitutive equation), in the following we shall assume these quantities to be given. By volume averaging the continuity equation Eq. (4.12) and using the averaging theorems Eq. (4.10) and Eq. (4.11) we obtain

$$\frac{\partial \phi}{\partial t} + \nabla \cdot (\phi \langle \mathbf{u} \rangle_i) = s \overline{v_n} \quad (4.13)$$

This result corresponds to Calonne et al. [2014b] when \mathbf{u} was set to zero. It relates ice mass changes in the control volume V to the deformation velocity \mathbf{u} and the accretion of mass v_n integrated over the surface s .

4.2.4 Evolution of the surface area per unit volume

Eq. (4.13) implies that the macroscopic mass conservation equation requires an evolution equation for the surface area s . Due to the general form of the velocity field (4.3) the derivation of the surface area evolution must be generalized compared to Drew [1990]. The essential steps are provided in Appendix 4.8.1, the result is given by

$$\frac{\partial s}{\partial t} + \nabla \cdot s \overline{\mathbf{w}} = s \overline{\mathcal{F}_s} \quad (4.14)$$

in terms of the source term \mathcal{F}_s given by

$$\mathcal{F}_s = 2v_n H + (\nabla \cdot \mathbf{u}) - \mathbf{n} [\nabla \otimes \mathbf{u}] \mathbf{n} \quad (4.15)$$

Here \otimes denotes the outer product of two vectors. Eq. (4.14) is a partial differential equation for the surface area per unit volume in a Eulerian frame of reference which accounts for the change in surface area from the divergence in the mean velocity field (left hand side) while the right hand side captures the contribution from growth (first term) and the first order correction of the surface area from deformation gradients involving \mathbf{u} (second and third term). Due to a typo in Drew [1990] the first term on the right hand side of (4.15) differs by a factor of 2 which affects

the form of the following curvature equations as well.

4.2.5 Evolution of interfacial curvatures

While the evolution equation for the ice volume fraction (4.13) requires the surface area, the equation for the surface area (4.15) requires the mean curvature. Analogous to Drew [1990] the local evolution equations for arbitrary moments of the curvature can be derived again by algebraic manipulation of (4.2) and subsequent averaging. For the curvatures we neglect higher order changes from non-normal components of the interface velocity via \mathbf{u} in (4.3) which is tedious, but principally feasible via the evolution of the metric tensor McLachlan and Segur [1994]. The key steps are provided in the Appendix 4.8.2, resulting in the set of continuity equations

$$\frac{\partial}{\partial t} \overline{H} + \overline{w} \cdot \nabla \overline{H} = -\frac{1}{s} \nabla s \overline{w} \left(\overline{H - H} \right) + \overline{\mathcal{F}_H} + \left(\overline{H - H} \right) \overline{\mathcal{F}_s} \quad (4.16)$$

$$\frac{\partial}{\partial t} \overline{K} + \overline{w} \cdot \nabla \overline{K} = -\frac{1}{s} \nabla s \overline{w} \left(\overline{K - K} \right) + \overline{\mathcal{F}_K} + \left(\overline{K - K} \right) \overline{\mathcal{F}_s} \quad (4.17)$$

$$\frac{\partial}{\partial t} \overline{H^2} + \overline{w} \cdot \nabla \overline{H^2} = -\frac{1}{s} \nabla s \overline{w} \left(\overline{H^2 - H^2} \right) + 2\overline{H} \overline{\mathcal{F}_H} + \left(\overline{H^2 - H^2} \right) \overline{\mathcal{F}_s} \quad (4.18)$$

with the source terms

$$\begin{aligned} \mathcal{F}_H &= -\left(2H^2 - K \right) v_n - \frac{1}{2} \left(\partial_1^2 + \partial_2^2 \right) v_n \\ \mathcal{F}_K &= -2HK v_n - H \left(\partial_1^2 + \partial_2^2 \right) v_n + \sqrt{H^2 - K} \left(\partial_1^2 - \partial_2^2 \right) v_n \end{aligned} \quad (4.19)$$

where $\partial_1^2, \partial_2^2$ denote the second derivatives along principal coordinates on the surface. Eqs. (4.13), (4.15), (4.16), (4.17), (4.18) constitute the evolution equations for the most important interface parameters hitherto investigated for snow.

4.3 Interface evolution of idealized grains

To assess the correctness of the coupled evolution equations we first consider the evolution of grains with idealized shapes but non-trivial curvature distributions (spheroids, tori) under a uniform growth law.

4.3.1 Reduced evolution equations

For single grains or statistically homogeneous microstructures the evolution equations can be simplified due to absence of the gradient terms in Eq. (4.16) to (4.18). Furthermore we can neglect deformation in the evolution for the averaged surface area i.e. the last two terms in \mathcal{F}_s vanish in (4.15). Due to the constant velocity field also non-local, surface gradient terms in the curvature equations vanish. Overall we end up with

$$\begin{aligned} \frac{\partial s}{\partial t} &= 2s \overline{v_n H} & \frac{\partial \overline{H}}{\partial t} &= \overline{v_n K} - 2\overline{H} \overline{v_n H} \\ \frac{\partial \overline{K}}{\partial t} &= -2\overline{v_n H K} \end{aligned} \quad (4.20)$$

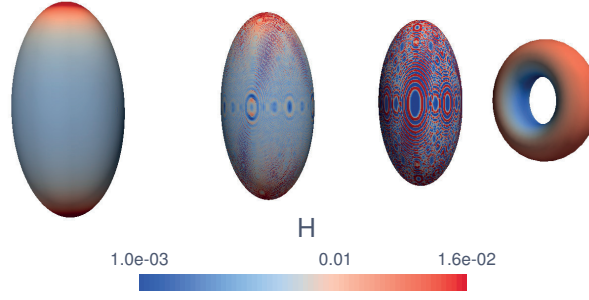


Figure 4.1 – Idealized grains (spheroids A,B,C and torus), surfaces colored by mean curvature H .

4.3.2 Generation of initial states

For the comparison we created three equally sized spheroids with different smoothing methods and a torus using VTK and Paraview Hernderson [2007]. Spheroid A is based on a parametric surface from a `vtkSphere` object and rescaled to a spheroid using `vtkTransform`. Spheroid B was sampled on a voxel image and convoluted with a Gaussian filter (support 4.5, $\sigma = 9$ voxels) for smoothing before applying a contour filter to obtain the triangulated surface mesh as the zero-level set of the image. Spheroid C is also based on a binary voxel image, but here contouring was applied before the mesh was smoothed by Laplacian smoothing with $S = 500$ iterations as described in chapter 2. To include also a grain with negative mean curvatures, a torus was chosen which is also based on a parametric surface with numerically exact positions of the mesh-points. All objects are shown in Fig. 4.1 revealing the differences in surface representation by the mean curvatures.

Results

All objects are evolved forward in time by (Euler) integrating the trajectories of the mesh points under a uniform normal velocity field v_n using the VTK filter `WarpByVector`. To ensure stability via the CFL-condition [Sethian, 1999], time steps are adapted to the mesh size. The procedure yields a time series of surfaces and at each time-step the averaged quantities $s, \overline{H}, \overline{K}, \overline{H^2}$ are obtained by integrating their local counterparts over the surface according to (4.8). This allows comparing left and right hand side of the evolution equations (4.20) using a Crank–Nicholson scheme for their (finite-differences) discretization. In the following we refer to the left hand side as the *measured* quantity and the right hand side as the *modeled* quantity. The results are shown in Fig. 4.2. For the Spheroid A and the torus, which are based on parametric surfaces, a very good agreement is obtained indicating the correctness of equations and calculation of interface parameters. The comparison of Spheroid A to B and C (Fig. 4.1) reveals the influence of different smoothing procedures when the objects are derived from voxel data, similar to the typical experimental situations discussed below. In particular higher order moments such as $\overline{H^2}$ are considerably affected by the apparent surface roughness (Fig. 4.2), but still resulting in a reasonable correlation between modeled and measured rates.

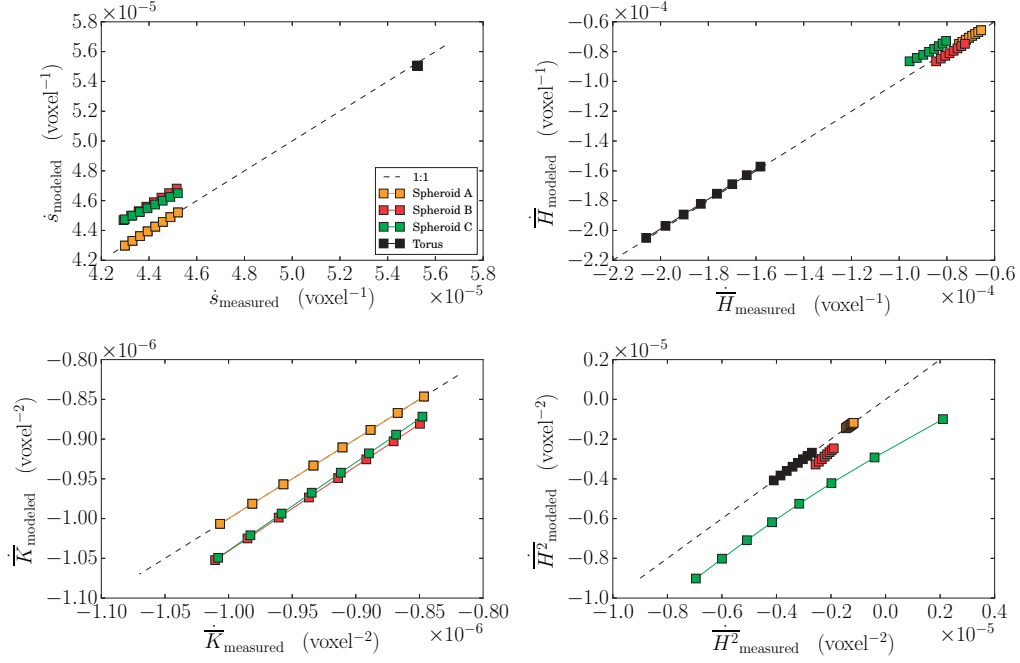


Figure 4.2 – Scatter plots of measured and modeled rates for interface parameters of the grains from Fig. 4.1.

The results for the evolution of idealized grains show that under certain requirements of surface smoothness, the image analysis can be applied to infer the evolution of interface properties via (4.20). This comparison can be directly carried out at the level of their governing differential equations if an estimate of the interface velocity is available.

4.4 Ice-air interface evolution from 4D tomography data

4.4.1 Time lapse experiments and interface tracking

Next we conduct a comparison of the model to 4D image data of a temperature gradient metamorphism experiment by using interface tracking, as developed in chapter 2, to estimate the *a-priori* unknown interface velocity. To this end we analyzed two temperature gradient experiments (Series 1 and 2) that were previously presented in Pinzer et al. [2012]. In these experiments, homogeneous cylindrical snow samples of diameter 3.6 cm and height 2 cm were thermodynamically driven by a constant temperature gradient applied via Peltier elements in an instrumented tomography sample holder to monitor the microstructure by μ CT. The snow in the experiments has the same mean temperature $T = -8^\circ\text{C}$, while slightly different temperature gradients $\nabla T = 46, 55 \text{ K/m}$ were applied for 384, 665 h with a time step between successive μ CT scans of 8 h.

For the image analysis the reconstructed binary images were blurred with a Gaussian filter (support = 2.0, $\sigma = 1.5$) to improve the extraction of the zero-level set from the contour filter, as suggested by the performance comparison from the previous section. From the time series of

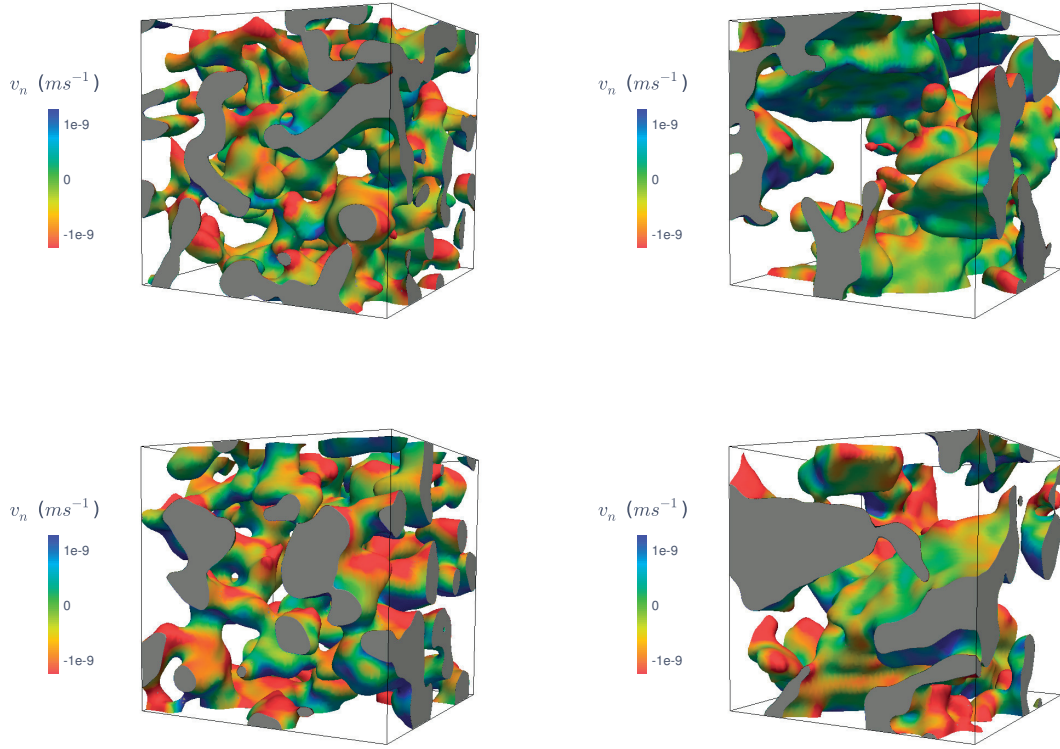


Figure 4.3 – Cubic cutouts of the ice-air interface at $t = 0$ (left) and $t = 288h$ (right) from Series 1 (top, cube length 1.26 mm) and Series 2 (bottom, cube length 2.52 mm) colored by interface velocities v_n .

images we extracted the interface velocity field using the interface tracking method developed in Krol and Löwe [2016a]. The rendered initial ($t = 0$) and intermediate ($t = 288h$) states of the microstructure together with their estimated velocity fields are shown in Fig. 4.3. The analysis yields local estimates of the geometrical quantities s, H, K, H^2 and the interface velocity v_n from which the right hand side (“modeled”) of (4.20) can be computed by integration over the surface. Again, we employ the set of reduced equations (4.20). We have tested the assumption of statistical homogeneity of the sample to drop the gradient terms. The relevance of neglecting the non-local terms requires however a separate discussion.

4.4.2 Results

The comparison of the measured and modeled rates from Eq. (4.20) (again compiled by Crank–Nicholson finite differencing) is shown in Fig. 4.4. The volume fraction rates $\dot{\phi}$ allow for the most basic assessment of the derived interface velocities via the right hand side of (4.13) which highly underestimates the measured rates. This is partly caused by the errors of the interface tracking method which converges to the correct values only for high temporal and spatial resolution (see chapter 2). Velocity estimates are additionally influenced by crystals entering

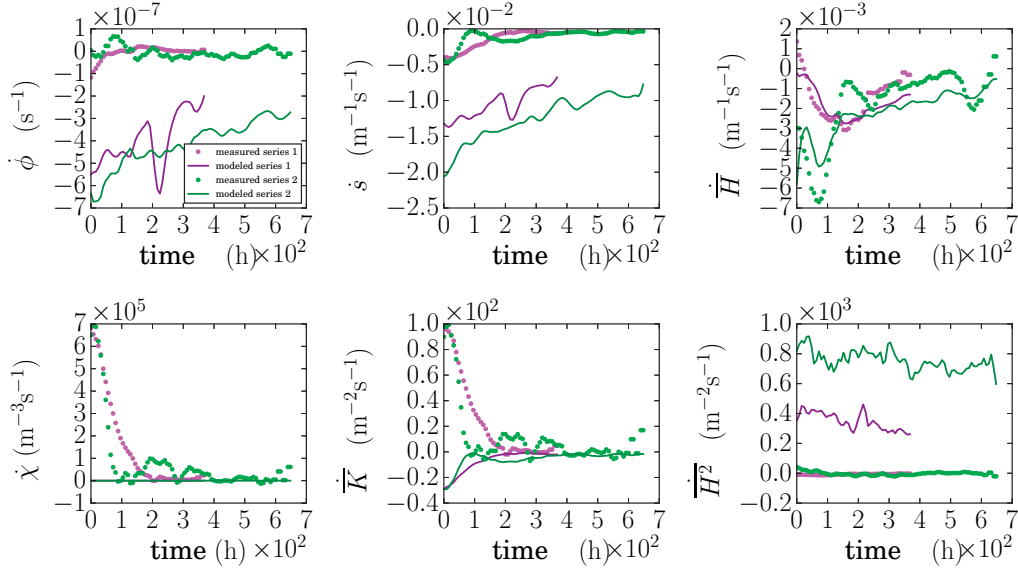


Figure 4.4 – Plot of measured rates versus predicted rates for the ϕ , s , H , K , χ and H^2 from Eqs. (4.20).

and leaving the control volume during a time step. Likewise, the modeled values for \dot{s} are also significantly influenced by the errors of $2\overline{v_n H}$. As a remedy, for the other parameters we have therefore replaced $2\overline{v_n H}$ on the right hand side by the measured \dot{s}/s values since the latter can be estimated reliably. This is immediately reflected by the \overline{H} comparison giving at least reasonable agreement which indicates $-\overline{H} \overline{v_n H}$ (cf. (4.20)) to be the dominant contribution. The consequence of omitting surface gradients in (4.20) is that the topology evolution is not well captured [Park et al., 2015]. This is reflected by (4.20), which implies $\dot{s}/s = -\dot{K}/K$. This is equivalent to an Euler characteristic per unit volume, $\chi = sK/(2\pi)$, which is constant in time. As shown by \overline{K} or $\overline{\chi}$, topology stabilizes only in the second part of the experiments while the initial dynamic phase is not captured by the reduced model. The $\overline{H^2}$ predictions are most affected by velocity errors in joint averages with higher order moments of K, H .

4.5 Statistical analysis of crystal growth laws

Independent of the errors in the estimation of interface velocities revealed in the previous section, the exact model allows conducting a statistical assessment of crystal growth laws which typically depend on quantities that can be computed with higher accuracy.

4.5.1 Growth laws for temperature gradient driven growth

If crystal growth is modeled as a variant of a Stefan-type of diffusion problem [Libbrecht, 2005], the local interface velocity must be related to the chemical potential difference between ice and vapor, i.e. to the difference between the actual vapor concentration $\rho_v(\mathbf{x})$ and the equilibrium concentration $\rho_v^{\text{eq}}(\mathbf{x})$ at a point \mathbf{x} on the interface according to $v_n(\mathbf{x}) = \alpha [\rho_v(\mathbf{x}) - \rho_v^{\text{eq}}(\mathbf{x})]$ with a

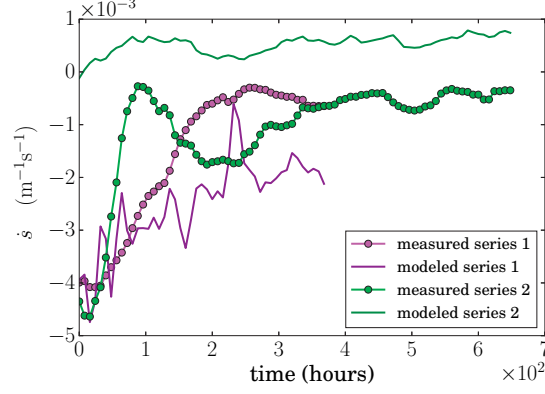


Figure 4.5 – Comparison of modeled and measured evolution of \dot{s} according to (4.22).

kinetic coefficient α . It is well-known that the excess vapor concentration comprises diffusive and kinetic contributions [Colbeck, 1983], their relative importance was however difficult to assess quantitatively so far. If for the diffusion limited part local equilibrium between temperature and vapor is assumed [Shreve, 1967], the local interface velocity can be related to temperature gradients in the pore space according to chapter 3

$$v_n(\mathbf{x}) = A \mathbf{n}(\mathbf{x}) \cdot \nabla T(\mathbf{x}) \Big|_+, \quad (4.21)$$

where $+$ denotes the limit of approaching the interface from the pore side.

To assess (4.21) we have computed the temperature fields for Series 1,2 in the microstructure by the Finite Element Method [Pinzer et al., 2012] using standard means of a voxel-based solution of the stationary heat equation in the air-ice “composite” by applying the average temperature gradient of the experiment as boundary condition in the numerics. This allows to compute the local temperatures and gradients at the interface to infer a theoretical estimate of the local interface velocity v_n according to (4.21). For A we used the temperature dependent theoretical prefactor A from chapter 3. These local values for v_n can be used in Eq. (4.20) to compute $s \overline{H v_n}$ by integration over the surface and estimate the theoretical rates for the surface area evolution. This amounts to a statistical analysis since we are actually probing the implicit curvature dependence of the temperature field in (4.21) via

$$\dot{s} = 2s \overline{H v_n} = s \int dH p(H) H v_n(H). \quad (4.22)$$

4.5.2 Results

The comparison of the left and right hand side of Eq. 4.22 are shown in Fig. 4.5. While the agreement is reasonable for Series 1, the experimental data for Series 2 is showing a decrease in surface area per unit volume while the growth law (4.21) would predict an increase (positive rates). To discuss the different behavior of Series 1,2 we note that the approximation (4.21) essentially implements the idea of purely diffusion limited growth where vapor fluxes in the pore space are related to temperature gradients assuming local equilibrium. In this picture,

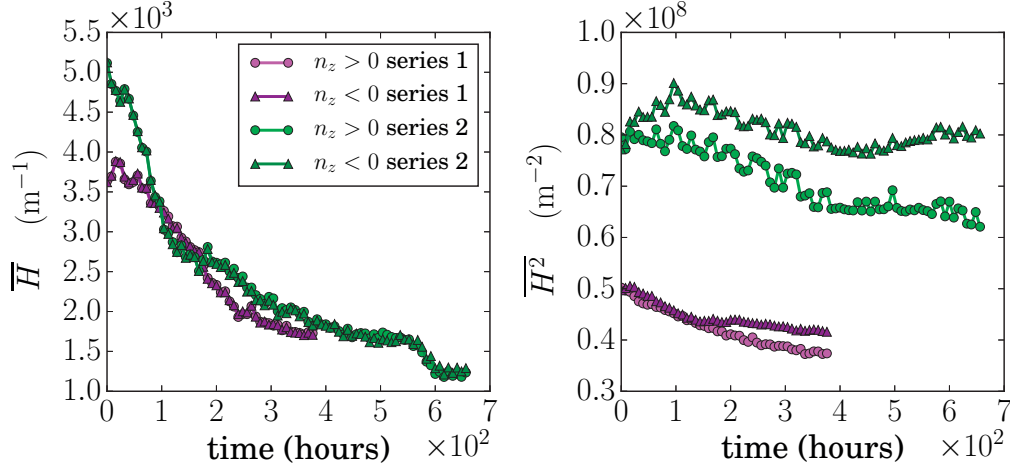


Figure 4.6 – Evolution of \overline{H} and $\overline{H^2}$ restricted to growing ($n_z < 0$) and sublimating ($n_z > 0$) parts of the interface.

variations of the interface velocity are mainly due to variations of temperature gradients caused by geometrical effects. Since the temperature is determined by the Laplace equation, the most prominent effect of geometry on the solution in a heterogeneous medium is the local “deformation” of temperature iso-lines. This leads to an increase of gradients at positive curvature regions (convexities) and a decrease of gradients in negative curvature regions (concavities). This effect is akin to Laplacian growth, i.e. the *destabilizing* contribution in the Mullins–Sekerka problem [Libbrecht, 2005] which principally allows for positive \dot{s} in (4.22). This effect is superimposed by more complex microstructural signatures in $v_n(H)$. The analyzed Series 2 provides clear evidence that the relation (4.21), which has been confirmed statistically chapter 2, is merely a side effect and not the *origin* of the observed evolution of the specific surface area since it is in contradiction with (4.22).

To further demonstrate the morphological differences between the two series we compared the difference between sublimating and growing surface sites by constraining the surface averages on upward and downward faces as a proxy for it (cf. Fig. 4.3 and Calonne et al. [2014a]). The results are shown in Fig. 4.6 which confirms the findings from Calonne et al. [2014a]: While \overline{H} on growing and sublimating parts remain the same, $\overline{H^2}$ starts from the same initial values but split up during the evolution reflecting the morphological asymmetry between growing and sublimating surfaces. The onset of disagreement found in Fig. 4.5 roughly corresponds to the onset of the $\overline{H^2}$ split up in Fig. 4.6. Fig. 4.6 also reveals that the width of the curvature distribution $\overline{H^2} - \overline{H}^2$ of Series 2 is considerably (60%) higher when compared to Series 1.

4.6 Discussion

4.6.1 Main findings

We have derived a mathematically exact model for the coupled evolution of the most important parameters that are presently used to analyze snow microstructure in tomography experiments [Flin et al., 2004, Schleef et al., 2014, Calonne et al., 2014a, Krol and Löwe, 2016b]. The derivation is based on volume averaging the (discontinuous) level-set equation as a full dynamical characterization of the ice indicator function at the micro-scale. The volume averaged evolution equations (4.13), (4.15), (4.16), (4.17), (4.18) enables to bridge from micro to macro scales relevant for continuum snow modeling [Calonne et al., 2014b].

We generalized the approach from Drew [1990] for a contribution of the interface velocity stemming from mechanical deformations. Even though we have not yet exploited these terms, they are crucial for future applicability to account for the fact that crystal growth in snow is always accompanied by viscoplastic deformations. The growth contribution to the interface velocity captures the non-equilibrium thermodynamics at the ice-air interface at the micro-scale scale, within the known limitations of diffusion modeling of crystal growth [Libbrecht, 2005]. Strictly, the set of equations are incomplete and must be regarded as a part of a hierarchy of evolution equations for the moments of the joint distribution of mean and Gaussian curvatures. For a validation of the PDEs in the reduced form this is however irrelevant since all terms can in principle be computed without *a priori* information solely from 4D observations.

We have shown that the equations are formally correct in a reduced setting (Eq. (4.20)) by comparing their predictions to the numerical propagation of interfaces of idealized grains (Fig. 4.1). The comparison revealed the impact of surface smoothness, with a stronger impact on the accuracy of higher order curvature terms \overline{K} and $\overline{H^2}$, in particular if the interfaces are derived from contouring binary voxel images for the 3D representation of geometry (Fig. 4.2).

In a next step we have compared the system of equations to 4D image data of snow microstructure evolution acquired from temperature gradient metamorphism experiments. These experiments were chosen to have negligible densification. Even though estimated interface velocities appear to be reasonably smooth (Fig. 4.3), the benchmark revealed considerable errors (Fig. 4.4). The main reason for the disagreement is the limited temporal and spatial resolution of present experiments which do not continuously resolve the evolution, causing a bias in the interface tracking method (chapter 2). An additional contribution stems from surface smoothness for the images derived from binary data, as suggested by the grain evolution tests. For an improvement it seems advantageous to combine segmentation, interface detection and velocity measurements directly from gray values by using level-set segmentation methods as e.g. employed in Fife et al. [2014].

We have further used the fact that uncertainties in velocity estimates do not play a role if the model is employed for a statistical assessment of closure relations for snow metamorphism under temperature gradient growth. We have shown that the surface area evolution cannot be explained in both experiments (especially Series 2 in Fig. 4.5) from the diffusion limited growth law Eq. 4.21, even though the latter itself has been previously confirmed statistically in chapter 2.

The excess vapor originating from temperature differences [Colbeck, 1983] either does (Fig. 4.5, Series 1) or does not (Fig. 4.5, Series 2) provide the dominating contribution to the surface area evolution, though uncertainties of the solution of the Laplace (heat) equation at the interface (see chapter 2) on voxel data must be acknowledged. Here further insight of the relation between kinetic effects and shape of ice crystals is required. In a first step it seems necessary to clarify the role of the morphological asymmetry between growing and sublimating parts of the surface (Fig. 4.6). The asymmetry reflects that sublimating surfaces (upward, cf. 4.3) tend to be rounded while growing surfaces (downward) become faceted prior to the skeletal instability (onset visible in Fig. 4.3). This is consistent with a variance of the mean curvatures which is higher on the downward surfaces, confirming the observations from Calonne et al. [2014a].

4.6.2 Limitations and prospects

It is obvious that inferring ice crystal growth thermodynamics solely from image data is inherently ill-posed since discriminating the cause for a moving ice-air interface either by deformation or by growth is locally impossible: A single sphere growing in temperature gradient simply migrates in a shape-invariant way [Shreve, 1967], equivalent to a rigid-body translation. The problem must in fact be constrained by additional micro-scale information on the strain field (densification). Fig. 4.3 reveals that heterogeneities in growth are heterogeneous over length scales of a single grain, while deformation processes are expected to be slow and with heterogeneities over larger scales [Theile et al., 2011]. It seems thus feasible to combine the interface tracking with e.g. volume correlation techniques on hierarchical scales and correct for deformation gradients which were neglected in (4.20). Deformations presently hinder a benchmark analysis (Sec. 4.4) of isothermal coarsening experiments of low density snow [Schleef et al., 2014] which are dominated by curvature effects but also strongly affected by deformations.

Another drawback of the present analysis is neglecting surface gradients in (4.19) for the reduced equations (4.20). Surface gradients are important for topological transitions [Park et al., 2015] which can be illustrated by the following hand-waving argument: Upon a topological transition (e.g. pinch-off) the velocity field must develop a discontinuity and surface gradients develop a delta-function leading to non-differentiable evolutions for the parameters H, K, H^2 . These aspects are notoriously difficult for surface tracking methods, while they are naturally accounted for in phase field models. For a finite number of droplets, the consequence of topology changes in the Mullins–Sekerka problem on a non-differentiable surface area is shown in Garcke [2013]. Although not mathematically exact, topological changes may be captured on a phenomenological level as source terms in the evolution equations as suggested in Drew [1990].

For our comparison we have chosen experiments where the densification is small. To reduce the uncertainties and further exploit the predictions of the model it would be helpful to carry out dedicated experiments at higher temporal and spatial resolution [Calonne et al., 2015] to capture the processes in a truly time-resolved manner. It seems sufficient to focus thereby on smaller volumes of interest since the representativeness of averages is not a problem. Ideally experiments would cover a few sintered ice crystals interacting by diffusion in a closed cavity for a full control of mass conservation. In the absence of micro-gravity, temperature gradients should be applied under different, relative orientation to gravity to discern growth from vertical

deformation velocities. Here the analysis of sinusoidal temperature gradient forcing [Pinzer and Schneebeli, 2009] may provide valuable insight. Additional input can be expected from phase field models, when the growth law v_n of the associated sharp interface limit is known exactly [Garcke, 2013]. Thereby details of the volume averaged microstructure model can be assessed beyond the scope of the idealized grain evolution presented here.

4.7 Conclusions

We have derived a mathematically exact upscaling model for microstructure parameters which are presently most commonly used to characterize snow microstructure in tomography experiments. The key ingredient is the local interface velocity of the ice-air interface which characterizes local crystal growth dynamics. The model can be used to benchmark the involved image analysis methods, since local estimates of the interface velocity can be obtained from 4D X-ray tomography image data without *a-priori* assumptions. Alternatively the model can be used for a statistical assessment of growth laws to improve simplifications for macroscopic continuum modeling of snow. Due to the rigorous starting point, we believe that the derived evolution scheme is a powerful tool to assess the simplifications employed for crystal growth in snow by combining 4D data and simulations and exploiting the overlap to closely related coarsening problems.

Acknowledgements

This work was funded by SNSF through grant no. 00021_143839.

4.8 Appendices

4.8.1 Derivation of the surface area equation

To derive (4.14) we consider the auxiliary expression

$$\frac{\partial}{\partial t} (\mathbf{n} \cdot \nabla \mathcal{I}) + \nabla \cdot ([\mathbf{w} \otimes \mathbf{n}] \nabla \mathcal{I}) \quad (4.23)$$

and note, by taking the gradient of (4.2), the validity of another auxiliary relation

$$\frac{\partial}{\partial t} \nabla \mathcal{I} + \mathbf{w} [\nabla \otimes \nabla] \mathcal{I} = - [\nabla \otimes \mathbf{w}] \nabla \mathcal{I}. \quad (4.24)$$

Carrying out the derivatives in (4.23) using the product rule, subsequently inserting (4.24) and further exploiting $\dot{\mathbf{n}} \cdot \mathbf{n} = 0$ and $(\nabla \otimes \mathbf{n}) \cdot \mathbf{n} = \mathbf{0}$ yields the identity

$$\frac{\partial}{\partial t} (\mathbf{n} \cdot \nabla \mathcal{I}) + \nabla \cdot ([\mathbf{w} \otimes \mathbf{n}] \nabla \mathcal{I}) = (\nabla \cdot \mathbf{w})(\mathbf{n} \cdot \nabla \mathcal{I}) - \mathbf{n} \cdot [\nabla \otimes \mathbf{w}] \nabla \mathcal{I} \quad (4.25)$$

which is valid for arbitrary \mathbf{w} . Now we insert the specific superposition (4.3) into the right hand side of (4.25) and note that the two velocity contributions must be treated differently: For the

deformation part \mathbf{u} no further simplifications can be made. For the growth part $\mathbf{v} = v_n \mathbf{n}$ that is normal to the interface, the right hand side reduces to $v_n(\nabla \cdot \mathbf{n})(\mathbf{n} \cdot \nabla \mathcal{I})$. Collecting all the terms and additionally inserting (4.4) we obtain

$$\frac{\partial}{\partial t} \left(\frac{\partial \mathcal{I}}{\partial n} \right) + \nabla \cdot \left(\mathbf{w} \frac{\partial \mathcal{I}}{\partial n} \right) = \mathcal{F}_s \left(\frac{\partial \mathcal{I}}{\partial n} \right) \quad (4.26)$$

with \mathcal{F}_s given by (4.15). Volume averaging (4.26) and exploiting (4.8) and (4.9) finally leads to (4.14).

4.8.2 Derivation of the curvature equations

To derive evolution equations for averages of arbitrary functions of the principal curvatures we start from the time evolution of the principal curvatures $\kappa_i, i = 1, 2$ under a normal velocity field v_n in a surface-following (Lagrangian) frame of reference which is given by Drew [1990]

$$\dot{\kappa}_i = -v_n \kappa_i^2 - \partial_i^2 v_n. \quad (4.27)$$

The time evolution for H, K, H^2 can be inferred by using (4.5) which yields

$$\dot{H} = \mathcal{F}_H, \quad \dot{K} = \mathcal{F}_K, \quad \dot{H}^2 = 2H\mathcal{F}_H \quad (4.28)$$

with $\mathcal{F}_{H,K}$ given by Eq. 4.19. The respective Eulerian counterparts of (4.28) are obtained by adding $\mathbf{w} \cdot \nabla(\bullet)$ on the left hand side.

The derivation of averaged quantities is shown below for the mean curvature \bar{H} as an example. To this end we multiply Eq. 4.26 by H and add the Eulerian counterpart of Eq. (4.28) times $\frac{\partial \mathcal{I}}{\partial t}$ which yields

$$\frac{\partial}{\partial t} \left(H \frac{\partial \mathcal{I}}{\partial n} \right) + \nabla \cdot \left(\mathbf{w} H \frac{\partial \mathcal{I}}{\partial n} \right) = H \mathcal{F}_s \frac{\partial \mathcal{I}}{\partial n} + \mathcal{F}_H \frac{\partial \mathcal{I}}{\partial n} \quad (4.29)$$

and volume averaging implies

$$\frac{\partial}{\partial t} (s\bar{H}) + \nabla \cdot (s\mathbf{w}\bar{H}) = s\bar{\mathcal{F}}_H + s\bar{H}\bar{\mathcal{F}}_s \quad (4.30)$$

After insertion of Eq. (4.14) and reshuffling terms we arrive at (4.16). Equations for \bar{K} and \bar{H}^2 can be derived accordingly.

Assessment of growth laws for isothermal metamorphism

5.1 Introduction

Isothermal metamorphism of snow has been studied for a long time from both, experimental (e.g. [Kaempfer and Schneebeli, 2007, Flin et al., 2004, Schleef and Löwe, 2013, Schleef et al., 2014]) and theoretical point of view (e.g. [Adams and Brown, 1982, Flanner and Zender, 2006, Legagneux and Dominé, 2005]). All studies relate to, at least from a phenomenological point of view, to the process of Ostwald ripening [Ratke and Voorhees, 2002]. Ostwald ripening is characterized by the growth of the average size of a collection of particles which interact by mass heat diffusion. The classical theoretical framework is provided by the Lifshits-Slyozov-Wagner (LSW) theory [Lifshitz and Slyozov, 1961, Wagner, 1961] which provides a minimal model for this process. The collective behavior is mediated by a curvature term in the equilibrium vapor pressure referred to as Gibbs-Thomson effect, which is incorporated in the boundary condition of the diffusion problem [Ratke and Voorhees, 2002]. The interaction of spheres of different size leads to an effective transport of mass from small to large particles.

To apply the model developed in chapter 4 to low density, isothermal experiments published earlier in Schleef et al. [2014] and Löwe et al. [2011], a full image analysis similar to the one presented in Section 4.4 must be carried out. However a major difficulty arises due to considerable deformation velocities (i.e. displacement rates that are larger than the average grain size). This makes it impossible to get reliable measurements for the interface velocities, especially since the deformation field is not uniform over the whole sample. Therefore, the motion of the interface from deformations are fundamentally indiscernible from curvature driven crystal growth. A different approach is thus needed here. To account for crystal growth *and* deformations we show that specific surface area

$$\text{SSA}_V = s/\phi, \quad (5.1)$$

with ϕ the volume fraction of ice, is essentially independent of the deformation field after making some simplifying assumptions. This approach requires us to derive an evolution equation for the SSA_V which can be combined with the statistical analysis similarly to Section 4.5, given a prescription of the interface velocity v_n in terms of local and averaged parameters is provided.

This Chapter is organized as follows. In Section 5.2 we derive an expression for the coupled evolution of the SSA_V and the second moment of the mean curvature $\overline{H^2}$. In Section 5.3 we discuss the available methods and the parameters that can be conveniently estimated within the scope of the thesis before going into the full analysis of the 600 samples. In Section 5.4 we will assess three different growth laws and derive corresponding evolution for SSA_V and $\overline{H^2}$. In Section 5.5 we show the results of the three different approaches that will be discussed in Section 5.6.

5.2 Evolution equation for SSA_V and $\overline{H^2}$

To predict the surface area evolution under coarsening of arbitrary interfaces we propose a similar expression for the interface velocity as suggested by Fife et al. [2014] and Tomita [2000]. This allows us to connect the components of LSW theory to the mathematical framework developed in Chapter 4.

The starting point is given by the evolution equation (4.14) for the averaged interfacial area

$$\frac{\partial s}{\partial t} + \nabla s \bar{\mathbf{w}} = s \overline{2v_n H} + \overline{(\nabla \cdot \mathbf{u})} - \overline{\mathbf{n} [\nabla \otimes \mathbf{u}] \mathbf{n}} \quad (5.2)$$

The corresponding equation for SSA_V can be derived by using equations (4.13), (5.2) and (5.1) yielding

$$\begin{aligned} \frac{\partial \text{SSA}_V}{\partial t} + \bar{\mathbf{w}} \cdot \nabla \text{SSA}_V + \text{SSA}_V \frac{1}{\phi} \cdot \nabla (\phi \bar{\mathbf{w}} - \phi \langle \mathbf{u} \rangle_i) = \\ 2 \text{SSA}_V \overline{v_n H} - \text{SSA}_V^2 \overline{v_n} - \text{SSA}_V \overline{\mathbf{n} [\nabla \otimes \mathbf{u}] \mathbf{n}} + \text{SSA}_V \overline{\nabla \cdot \mathbf{u}} \end{aligned} \quad (5.3)$$

For simplicity, we neglect deformation velocities, specifically we omit the last two terms of Eq. (5.3). This implies $\bar{\mathbf{u}} = \langle \mathbf{u} \rangle_i$. Furthermore we assume that the volume fraction ϕ and surface s are homogeneous to neglect corresponding gradients in (5.3), which leads to

$$\frac{\partial \text{SSA}_V}{\partial t} + \text{SSA}_V \nabla \cdot (\bar{\mathbf{v}}) = 2 \text{SSA}_V \overline{v_n H} - \text{SSA}_V^2 \overline{v_n}. \quad (5.4)$$

Note that Eq. 5.4 only involves the divergence of the yet unspecified growth velocity $\bar{\mathbf{v}}$ while the divergence of the deformation velocity $\nabla \cdot \bar{\mathbf{u}}$ drops out due to $\bar{\mathbf{u}} = \langle \mathbf{u} \rangle_i$.

Therefore, considering the specific surface area SSA_V instead of s , enables the separation of densification and crystal growth and the only contribution to the evolution of SSA_V comes from crystal growth. This approach is supported by the finding of Schleef et al. [2014], who showed that the evolution of the SSA_V is not statistically influenced by the applied external stress. This approach can be considered as a formalization of the fact that the SSA_V in a volume does not

change if additional snow of the sample type is added.

Next, we derive here a similar expression for $\overline{H^2}$ by starting from Eq.(4.18) for $\overline{H^2}$

$$\frac{\partial}{\partial t} \overline{H^2} + \overline{\mathbf{w}} \cdot \nabla \overline{H^2} = -\frac{1}{s} \nabla s \overline{\mathbf{w}} \left(H^2 - \overline{H^2} \right) + 2 \overline{H \mathcal{F}_H} + \left(H^2 - \overline{H^2} \right) \mathcal{F}_s, \quad (5.5)$$

with

$$\mathcal{F}_H = - \left(2H^2 - K \right) v_n - \frac{1}{2} \left(\partial_1^2 + \partial_2^2 \right) v_n. \quad (5.6)$$

In addition to the homogeneity assumptions for s and ϕ we also have to assume $\nabla \overline{H^2} = 0$ and $\nabla \cdot (s \overline{\mathbf{w}} H^2) = s \overline{H^2} \nabla \cdot \overline{\mathbf{w}}$ to obtain an expression for $\overline{H^2}$ that is independent of gradient terms. In addition, we neglect the second term in Eq.(5.6) as done in Section 4.5 to arrive at

$$\frac{\partial}{\partial t} \overline{H^2} = -2 \left(\overline{v_n H^3} - \overline{v_n H K} + \overline{H^2 v_n H} \right). \quad (5.7)$$

which is the same equation (4.20), as used in Chapter 4.

5.3 Data and Methodology

To validate the mathematical model developed in Chapter 4 for isothermal metamorphism of snow we will reanalyze the dataset originally published in Schleef and Löwe [2013] and Schleef et al. [2014]. The data set consists of 45 time-series containing 600 μ CT samples of naturally and artificially produced fresh snow with various morphologies undergoing metamorphism and compaction under applied stresses. The dataset is extended by three longer term time series consisting of 36 μ CT samples originally published by Löwe et al. [2011].

A thorough analysis similar to Chapter 4 would require a full VTK interface analysis of the 636 measurements, which has not been done due to time constraints. But even without this analysis it is possible to proceed with already existing data and asses Eq.(5.4) and (5.7) in a preliminary test. To this end, we use an alternative curvature characterization presented in Schleef and Löwe [2013], namely by the integral-geometric computation of the mean and Gaussian curvature according to Michielsen and Raedt [2001]. This data is complemented by estimates of $\overline{H^2}$ that can be retrieved from the two-point correlation function (see chapter 3).

The estimates for \overline{H} and \overline{K} are calculated from the Minkowski functionals MF_2 , MF_3 and MF_4 [Michielsen and Raedt, 2001] by

$$\overline{H} = \frac{3\text{MF}_3}{\text{MF}_2} \quad \text{and} \quad \overline{K} = \frac{6\pi\text{MF}_4}{\text{MF}_2}. \quad (5.8)$$

We tested these relations by comparing the Minkowski-based estimates for \overline{H} and \overline{K} to the VTK-based estimates for temperature gradient series 2, analyzed in Chapter 4. The results are given in Fig. 5.2 and show a principle agreement for both quantities, with increased scatter in the Gaussian curvature. The higher order moment $\overline{H^2}$ can be obtained from the two-point correlation functions, which have also been computed previously for the data-sets of interest. By

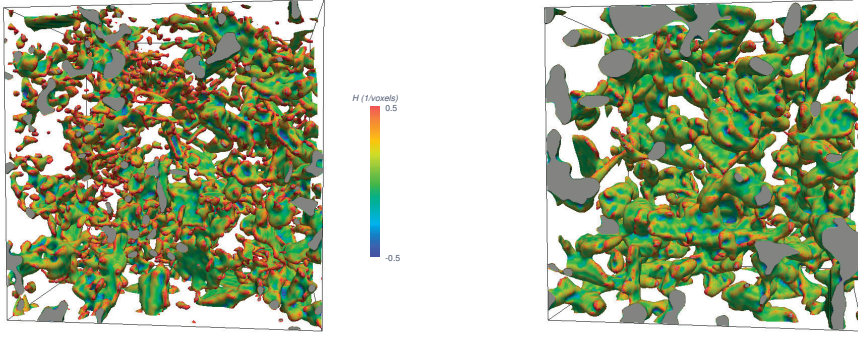


Figure 5.1 – Visualization of initial and final mean curvature measures on one of the compaction experiments (natural snow at $-13^{\circ}C$, Schleef et al. [2014]), retrieved from the VTK-based image analysis.

fitting the two-point correlation function we can retrieve the parameters SSA_V , the curvature length λ_2 and the exponential correlation length ξ (see Chapter 3). To obtain the second moment of the mean curvature $\overline{H^2}$ we use Eq.(3.8), from which we calculate

$$\overline{H^2} = \lambda_2^{-2}/8 + \overline{K}/24, \quad (5.9)$$

where \overline{K} is estimated from the Minkowski functionals via Eq.(5.8).

5.4 Growth laws for isothermal metamorphism

Finding a valid model for v_n is not a trivial task. In chapter 2, two growth laws were tested on an isothermal experiment, 1) a kinetics limited and 2) a diffusion limited growth law. Here we will test these different growth laws that can be represented in the general form

$$v_n = C \left(\overline{H} - H \right) / L \quad (5.10)$$

with three possible expressions for L

$$L = \begin{cases} 1 \\ \lambda = (2H^2 - K)^{-1/2} \rightarrow (2\overline{H^2} - \overline{K})^{-1/2} \\ \xi = f(SSA_V, \overline{H^2} - \overline{K}/3). \end{cases} \quad (5.11)$$

For $L = 1$ we obtain the kinetics limited growth law used in chapter 2. For a and $L = \lambda$ we obtain the form for diffusion limited growth, which is believed to hold for bicontinuous structures [Fife et al., 2014, Tomita, 2000], where λ can be interpreted as a screening length [Tomita, 2000]. As such λ is actually a local quantity, but for reasons related to the limitations of available data we will replace $2H^2 - K$ by $2\overline{H^2} - \overline{K}$ in Eq. (5.11) as indicated by the arrow. The third growth law with L given by the exponential correlation length ξ is an ad-hoc, empirical variation of the

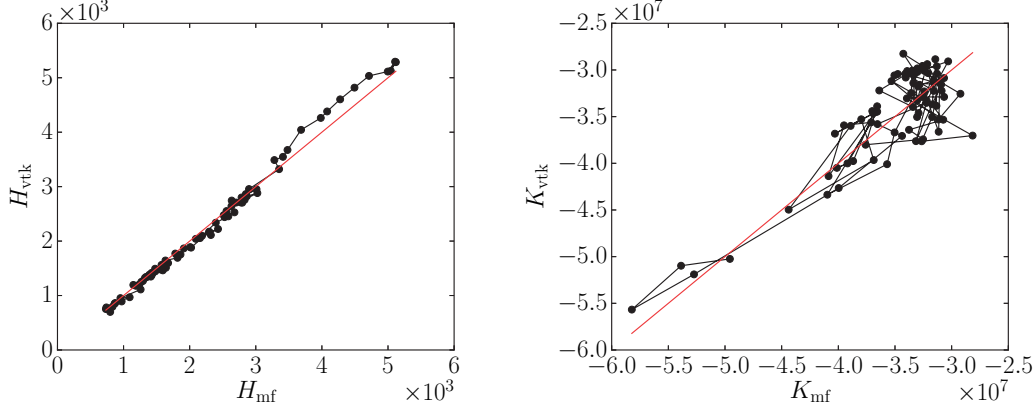


Figure 5.2 – Scatter plots of the mean curvature \overline{H} and the Gaussian curvature \overline{K} measured with the VTK based image analysis and with the Minkowski functionals, according to Eq. 5.8 on TG series 2 from chapter 4. The red lines indicate the 1 : 1 correspondence.

diffusion limited growth law.

For all mentioned possible growth laws $\overline{v_n} = 0$. The expressions Eq. (5.11) and $\overline{v_n} = 0$ can be used in Eq.(5.4) to obtain the evolution equation for the SSA_V

$$\frac{\partial \text{SSA}_V}{\partial t} = 2C(T) \text{SSA}_V (\overline{H^2} - \overline{H}^2) / L \quad (5.12)$$

with a temperature dependent prefactor $C(T)$.

For the evolution of the second moment of the mean curvature we plug Eq. (5.11) into Eq. (5.7) and obtain

$$\frac{\partial \overline{H^2}}{\partial t} = -\frac{2C(T)}{L} (\overline{H^4} - \overline{H} \overline{H^3} - \overline{H^2 K} + \overline{H} \overline{H K} + \overline{H^2} \overline{H^2} - \overline{H}^2). \quad (5.13)$$

This form obviously has many higher order terms that cannot be computed from the Minkowski functionals and two-correlation function data. Therefore we have to resort to a parametrization of the higher order terms. Inspired by the form of Eq.(5.12), a first attempt is given by

$$\frac{\partial \overline{H^2}}{\partial t} = 2D(T) \overline{H^2} (\overline{H^2} - \overline{H}^2) / L \quad (5.14)$$

with a temperature dependent prefactor $D(T)$. Both equations (5.12) and (5.14) can be validated with the given methodology discussed in Section 5.3.

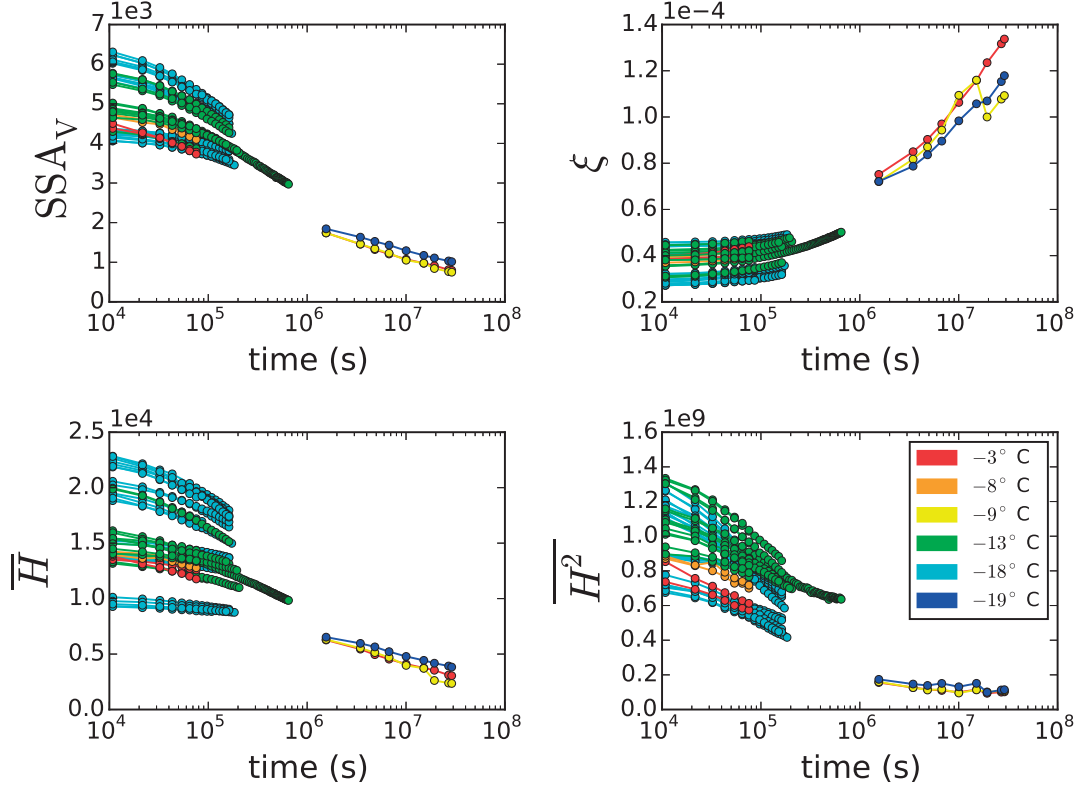


Figure 5.3 – Plot of the measured parameters ϕ , SSA_V , \overline{H} and \overline{H}^2 of all 48 datasets over time.

5.5 Results

For illustration purposes we have generated two VTK-based visualizations of an initial and final snow sample out of the isothermal metamorphism experiments from Schleef et al. [2014] shown in Fig. 5.1.

For all 48 isothermal experimental time series we have estimated the parameters of the model by means of the integral geometry estimates for \overline{H} and \overline{K} and a fitting procedure of the two-point correlation function to estimate \overline{H}^2 , λ and ξ as described in Section 5.3. The time evolution of all parameters SSA_V , ξ and the curvatures terms \overline{H} and \overline{H}^2 are shown in Fig. 5.3.

Each time-series is fitted to $C(T)$ and $D(T)$ for which we allow a nonlinear dependency on temperature by including three fit parameters

$$\begin{aligned} C(T) &= a_1 + b_1 T + c_1 T^2 \\ D(T) &= a_2 + b_2 T + c_2 T^2. \end{aligned} \tag{5.15}$$

We have tested Eq. (5.12) and Eq. (5.14) with the three possible expressions for the interface velocity Eq. (5.11) and measured its performance by the Pearson correlation coefficient R^2 . The results are given in Table 5.1. The best model performance was obtained when $L = \xi$ with a Pearson correlation coefficient $R^2 = 0.88$ for the evolution of the SSA_V and \overline{H}^2 (see Table

Table 5.1 – Summary: Correlation coefficients for ISO closure models

interface velocity	R^2 for Eq. (5.12)	R^2 for Eq. (5.14)
$v_n = C \left(\overline{H} - H \right)$	0.80	0.76
$v_n = C \left(\overline{H} - H \right) / \lambda$	0.84	0.80
$v_n = C \left(\overline{H} - H \right) / \xi$	0.88	0.83

5.1). In Fig. 5.4 we show measured and modeled rates for SSA_V and \overline{H}^2 for the best performing model ($L = \xi$ in Eq. (5.11)). For this growth law, the optimal parameters from Eq. (5.15) are $a_1 = 4.7 \times 10^{-17}$, $b_1 = 3.6 \times 10^{-19}$, $c_1 = 7.0 \times 10^{-22}$ and $a_2 = 1.3 \times 10^{-16}$, $b_2 = -9.9 \times 10^{-19}$, $c_2 = 1.9 \times 10^{-21}$.

5.6 Discussion and Conclusion

We have made a first attempt to validate the mathematical framework proposed in Chapter 4 for 48 isothermal compaction experiments in a statistical closure modeling approach. The chosen expression for v_n has a measurable impact on the performance.

Overall, the performance of this model for SSA_V is similar to the model that is proposed by Schleef et al. [2014]. We suggested a preliminary but reasonable approach to predict evolution of \overline{H}^2 , which has never been done before.

For the data in Chapter 2, there was more support for the kinetic-based growth law, i.e. $L = 1$ in Eq. (5.1), than for diffusion limited growth laws for fresh snow samples. Here we find that if L is chosen to be the exponential correlation length ξ , the model performs slightly better. It is however, important to note that the analysis in Chapter 2 was based on a local quantity λ in Eq. (5.11) while here we only tested averaged length scales (ξ and λ). We can therefore not yet conclude that this model gives more physical insight to the problem.

Despite a similar performance, the model for SSA_V presented in [Schleef et al., 2014] has the advantage of being rather simple. Its prediction is given by

$$\text{SSA}_V = (a' + b'T) \text{SSA}_V^{m'} \quad (5.16)$$

and only needs an initial measurement of SSA_V , which could be achieved with infrared-photography [Matzl and Schneebeli, 2006]. Thus, Eq. (5.16) does not rely on μCT measurements or uncertain predictions of \overline{H}^2 .

Despite the fact that many assumptions on the homogeneity of the samples had to be made to arrive at Eq. (5.12), they can all be eventually investigated by going back to the mathematically exact starting point Eq. (5.3) and (5.5).

The scatter that is observed in Fig. 5.4 can have various origins. To investigate the temperature

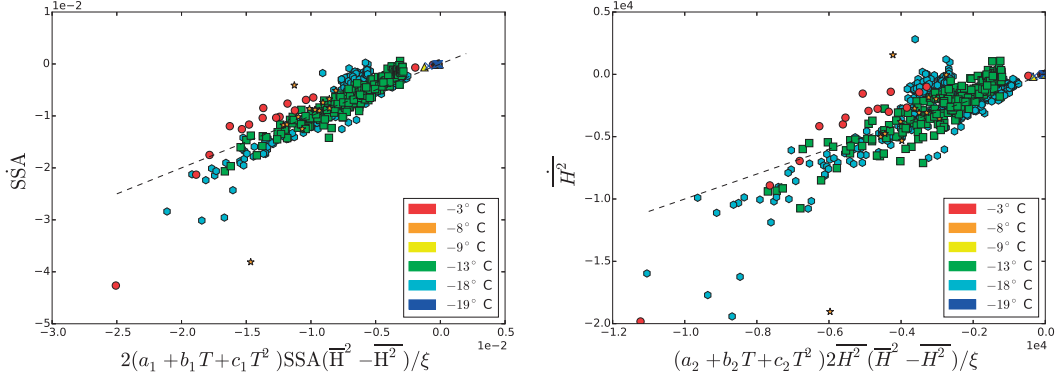


Figure 5.4 – Plot of measured rates versus predicted rates for the SSA_V and $\overline{H^2}$.

dependence of the prefactors $C(T)$ and $D(T)$, we have also fitted all series in the dataset individually with one parameter C, D and assessed the distribution of the fitted values as a function of temperature. The results are shown in Fig. 5.5 together with the best estimate of $C(T)$ and $D(T)$ from Eq. (5.15). Although a non-linear dependency of ice-kinetics could be expected [Libbrecht, 2005], the scatter is rather large especially given the scarce data for higher temperatures. However, the scatter plots of the coefficients for C and D look very similar, indicating that the growth laws from Eq. (5.11) are a reasonable starting point. The parametrization of Eq. (5.14) is considerably influenced by the higher order terms in $\mathcal{F}_H \overline{H}$.

The evolution of both SSA_V and $\overline{H^2}$ can, at least to some extent, be related to the variance of the mean curvature. This suggests that all length scales discussed here behave similarly in isothermal metamorphism. This also explains why Eq. (5.16) can be relatively successful. However, in view of temperature gradient metamorphism, where the curvature length behaves differently from the SSA_V , see Chapter 3 and Chapter 4, the potentials of a rigorous starting point which distinguishes between both quantities will become obvious.

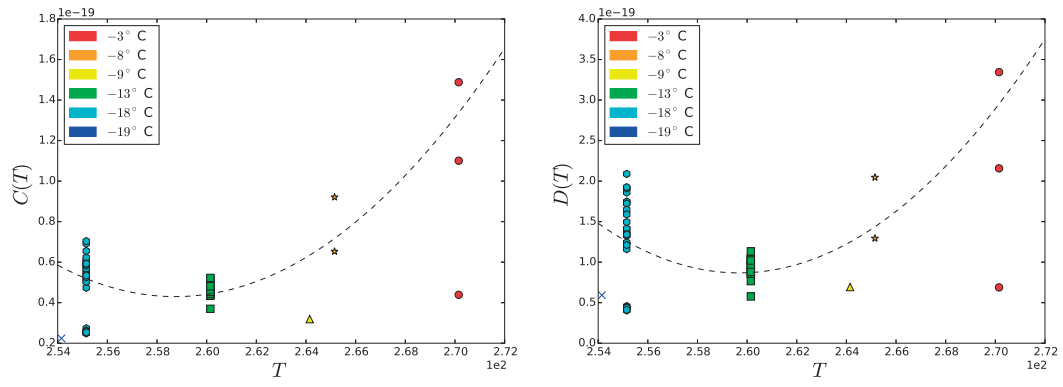


Figure 5.5 – Scatter plot of fitted values for $C(T)$ and $D(T)$ as a function of temperature.

Conclusion

The research gap for modeling microstructure evolution in snow could be described from two diametrically opposed perspectives. One is the applied, macroscopic perspective, of continuum modeling of heat and mass transfer in operational snowpack models [Lehning et al., 2002, Vionnet et al., 2012], with empirical choices of microstructure parameters, tailored to traditional measurements in the field [Fierz et al., 2009], and employing pragmatic approaches for the rate equations of these parameters in the models. The other is the fundamental, microscopic perspective, which focuses on details of shape evolution for single ice-crystals [Demange et al., 2017a] and employs ice crystal growth thermodynamics via non-equilibrium growth laws [Libbrecht, 2003]. In between these two perspectives, there are recent advancements of X-ray tomography and time-lapse observations that were already focusing on relevant parameters from the microscopic perspective (interfacial curvatures), but still missing key ingredients to serve as a validation tool for macroscopic snowpack modeling. Overall, the two perspectives were hitherto largely disconnected.

The goal of improving microstructure dynamics in snowpack models bears fundamental difficulties of choosing a suitable modeling strategy and deciding which microstructure parameters should be actually considered in a future model. To this end, the problem needed to be iterated from different sides cf Fig. 1.5, and these are reflected by the main research focuses of the thesis i) deciding on what kind of microstructure parameters should be considered ii) assessing the possibilities of extracting key crystal growth properties from time-lapse tomography and iii) deriving an evolution model for the parameters of interest.

Based on the literature and the results from Chapters 2 and 3 we decided to derive a microstructure evolution scheme from first principles. We re-derived a rigorous upscaling approach of interfacial evolution based on Drew [1990], and tailored it to snow microstructural parameters. The advantage of being mathematically exact means that the model can be unambiguously validated in idealized situations (Sec. 4.18). The model comprises coupled partial differential equations for the parameters. The equations are naturally coupled to the upscaled evolution equations for heat and mass via the local *a priori* unknown velocity v_n of the ice-air interface driving the microstructural evolution of snow. To quantify the interface velocity we developed a VTK-based image analysis tool (see chapter 2) that enables tracking the ice-air interface from two consecutive μ CT images. We showed that in principle it is feasible to assess the validity of

theoretical growth laws, but we observed a considerable scatter for isothermal and temperature gradient conditions. This was mainly due to experimental difficulties and subsequent resolution issues and uncertainties inherent to the image analysis methods, which will be discussed in chapter 7.

The derivation of the model has shown that the evolution equation for the surface area per unit volume s is mainly determined by a volume average of the interface velocity times the mean curvature. It was therefore mandatory to derive an equation for the mean curvature using Eq. (4.16) for the local evolution of the principle curvatures κ_1, κ_2 . In the evolution equation for \overline{H} , the Gaussian curvature K appears, highlighting the hierarchical character of these coupled differential equations. Technically, the upscaling scheme can be applied to *any* geometrical parameter $f(\kappa_1, \kappa_2)$, which can be expressed as a function of the principal curvatures κ_1 and κ_2 since the local time evolution of such a parameter can be derived via $\dot{f} = \nabla f \cdot (\dot{\kappa}_1, \dot{\kappa}_2)$ via Eq.(4.27) and subsequently volume-averaged. The Gaussian curvature $K = \kappa_1 \kappa_2$ is an example of such a parameter. The appearance of the curvatures in the model is a very convenient coincidence since exactly these quantities are being increasingly investigated experimentally, and the microstructure model thus naturally follows present trends in time-lapse tomography with a focus on mean [Flin et al., 2004], Gaussian [Schleef et al., 2014, Calonne et al., 2014a] or variance of mean curvatures [Calonne et al., 2014a].

The fact that the model predicts parameters (s, H, K, H^2) that can be conveniently measured does not, however, imply that these parameters are the most *important* ones to model physical properties of snow. While the relevance of s (or alternatively any other (inverse) length scale which is related via Eq. (3.7)) is without a doubt, the relevance of averaged curvatures for macroscopic physical properties of snow has not yet been discussed in literature. In contrast, recent work rather focused on the correlation length as key parameter, due to the relevance for microwave scattering coefficient, dielectric permittivity, and thermal conductivity parameterization [Löwe et al., 2013, Calonne et al., 2014b, Löwe and Picard, 2015, Leinss et al., 2016]. Due to the predictive power of correlation lengths, it is clear that a new modeling approach should include the possibility to predict the exponential correlation length.

It was thus necessary to confirm that the new evolution model is able to make contact to the correlation lengths. The analysis from Section 3.4 shows that exponential correlation lengths can be accurately predicted from the Porod length λ_1 and the curvature length λ_2 , or likewise from ϕ , SSA and $\overline{H^2}$. This finding has two important consequences. First, it confirms that a dynamic model for ϕ , SSA and $\overline{H^2}$ can also be used to infer the evolution of the exponential correlation lengths via the parametrization (3.18). Second, it reveals that $\overline{H^2}$ carries independent information, beyond the SSA, and can thus be regarded as a shape parameter (Section 3.5.3). This is conceptually highly satisfying since the suggested new approach thereby follows exactly the previous strategy in snowpack models where the parameters (grain size, sphericity, dendricity) essentially characterize the size of and deviations from an equivalent spherical shape. The new objective parameters SSA, \overline{H} , \overline{K} , $\overline{H^2}$ naturally follow the same idea and even come with their exact evolution equations. The immediate question if one of these parameters will possibly turn out to be more redundant than the others could not yet be answered unambiguously from the analysis (see chapter 5).

One of the unique features of the model is that it can be used as a benchmark, suited to assess experimental methods, image analysis and assumptions underlying the microstructure evolution during time-lapse μ CT imaging (sec. 4.5). Such a benchmark comparison has revealed that errors from the current image analysis setup related to the interface velocity estimates is the origin of the current disagreement between model and measurements in snow. On the other hand, prescribing the interface velocity enables a statistical approach to model validation that circumvents the estimation of velocity estimates. For temperature gradient metamorphism we confirmed before that local growth is correlated to the local temperature gradient (see chapter 2). However, the statistical model analysis showed that this correlation was unable to correctly predict the measured SSA decay for at least one of the two tested temperature gradient experiments. This means that the evolution of SSA cannot be recovered if the growth law Eq. (4.21) in terms of the local temperature gradient (diffusion limited growth) is used to evolve the microstructure. It is therefore clear that the growth law for temperature gradient metamorphism must be critically revisited in the future, e.g. by considering kinetic effects. Some ideas which will be further discussed in chapter 7. While kinetics effects have been well-discussed in the literature for a long time [Colbeck, 1983] and are clearly visible from the depth hoar morphology (see Figures 1.1, 1.4, and 4.3), this is the first time that the diffusion limited growth law given by the local temperature gradient approximation can be discarded as the source of SSA decay based on quantitative measurements from 4D μ CT data.

Limitations and Outlook

7.1 Image analysis and experimental setup

Despite the wealth of new opportunities that come with the new microstructure evolution model, this work also clearly revealed key issues that need to be solved in the future. The interface tracking method developed in chapter 2 bares fundamental deficiencies when estimating local crystal growth rates. It gives rise to topological inconsistencies as discussed in chapter 2 and is biased towards negative velocities, as shown in chapter 4, Fig. 4.4. In addition the method can not discern crystal growth from settling. Although this is inherent to interface tracking and not dependent on the methodology that is used here, it prevents drawing firm conclusions on the curvature dependence of growth in isothermal metamorphism and also contributes to the error in the benchmarking of the developed model in chapter 4. Although we have shown that the interface-tracking method can, in principle, recover prescribed growth laws for high spatial and temporal resolution in an idealized setup, the present experimental setting gives rise to a significant signal-to-noise problem, which limits the extraction of the correctness of growth laws and subsequently the validation of metamorphism models from 4D time-lapse data. This error also influences the solution of the finite element method for computing local temperature gradients in the vicinity of the interface. Here the question remains to what extent higher resolution experiments would solve the inherent problem of re-sampling a voxel-based, numerical solution on a triangular mesh representing the interface, or if 3D solutions to the heat equation must generally move towards more sophisticated methods as discussed e.g. in Soghrati et al. [2012].

The temporal and spatial resolution of the μ CT images give rise to a significant signal-to-noise problem which must be approached twofold. First, it is desirable that the spatial and temporal resolution of experiments become higher in the future. The spatial resolution of the μ CT measurements may be increased to similar values obtained by Calonne et al. [2015] which would already gain a factor 3 in resolution. For crystal growth, a trade-off between resolution and statistical representative sample size must be achieved. To estimate to what extent the spatial and temporal resolution must be improved, a sensitivity study should be conducted on existing data. For the purpose of benchmarking the microstructure model, experimental data with higher resolution is likely required. Second the interface tracking for local crystal growth rates can be likely improved by working on gray-scale data rather than on binary images. For example,

estimating the ice-air interface can be done by contouring the original gray-scale images before thresholding them to binary images on which the present analysis is based. This suggests that level-set segmentation methods [Fife et al., 2014] might be advantageous since they directly make contact to the level-set equation (4.2), which is the core of the microstructure model presented here.

Another important source of uncertainty is the compaction by gravity. This is most pronounced in isothermal metamorphism of fresh snow, making it presently impossible to benchmark the experimental data by the model. Although there are alternatives to validate present ideas of curvature-driven coarsening (shown in chapter 5), the interface velocities cannot discern displacements from crystal growth. Especially in temperature gradient metamorphism, the temperature gradient is typically vertically oriented (parallel to gravity) in both, the lab-experiments and in the natural snowpack. Experiments with horizontal temperature gradients may be able to discern between the two contributions to the interface velocities.

7.2 Modeling snow microstructure

The model equations are mathematically exact and are shown to correctly predict the evolution of simple geometrical objects without topological changes. However, further work needs to be done before this microstructure model can be implemented in a snowpack model. The form of the equations requires an interface velocity prescription that describes growth rates specific to the type of snow metamorphism. In particular, the results for the temperature gradient case have shown that there is a clear lack of insight in the growth law that describes the evolution of the microstructure with sufficient success.

In additions to the uncertainties related to crystal growth, the equations also contain higher order curvature terms. Strictly speaking, the evolution equation for these terms must be derived as well, revealing the hierarchical structure of the partial differential equations involving higher moments of curvatures of arbitrary order. For practical reasons, a truncation or effective mean-field approach, has to be given to solve the closure problem of these coupled partial differential equations. Chapter 5 of this thesis indicates how this can be done for isothermal conditions where an effective description of the SSA decay is derived and a parametrization for the evolution equation for second moment of the curvature is proposed. The results suggest that some curvature metrics are correlated and therefore a similar parametrization for the mean and Gaussian curvature could be expected. Once the equations are rewritten in terms of available parameters, the coupled set of equations can be solved numerically and could serve as a module in a snowpack model.

A different route to utilize the equations is to perform a term-by-term parametrization based on the form of the present equations, and by fitting the parameters to existing datasets. For this approach however, two temperature gradient metamorphism experiments are not sufficient. For this purpose, more experiments, with variation in the initial values for density, SSA and curvatures at various temperatures and temperature gradients, should be conducted.

Another issue that needs to be addressed, is topological changes. The evolution equations for

both the mean curvature \overline{H} and the Gaussian curvature \overline{K} depend on the surface gradients of the interface velocity (see Eq. (4.19)). The evolution of the Euler characteristic defined by $\chi = s\overline{K}/2\pi$ in the reduced setting (where surface gradients of the interface velocity are neglected) predicts zero changes. Therefore, the reduced set of equations cannot predict topological changes. This suggests that the changes in topology are related to the terms that have been neglected, which is well-discussed in Park et al. [2015]. Interestingly, these terms affect the evolution equation of the SSA only indirectly, but have a direct effect on the evolution of the curvatures. A qualitative argument can be made that a topological change initiates from a discontinuity in the derivative of the interface velocities. However these transitions are far from being experimentally detectable due to limited resolution. As a remedy, it seems possible to tackle this problem statistically, similar to Drew [1990], by replacing terms involving surface gradients, with terms that statistically capture the contribution related to $\dot{\chi}$ in a parametrized manner. These choices should be verified of course by experiments.

Furthermore, it is instructive to comment on a potential extension of the model to anisotropic microstructures. As shown by Löwe et al. [2013], the anisotropy of snow is an important parameter to estimate the effective thermal conductivity of snow. A possible route to include anisotropy in the present framework could be to derive an evolution equation for an anisotropy (fabric) tensor $\overline{\mathbf{n}} \otimes \overline{\mathbf{n}}$ as used by López-Barrón and Macosko [2010] and Shertzer and Adams [2011]. Such a definition of structural fabric can be conveniently related to the level-set equation (4.2) that enables a treatment within the present framework.

The analysis in chapter 4 shows that the details of temperature gradient metamorphism case is far from being understood, and more insight from crystal growth dynamics is needed. To improve on the growth law for temperature gradient metamorphism in snow we should revisit the Gibbs-Thomson boundary condition Eq. (2.3). In chapter 2 we have assumed Dirichlet boundary conditions and local thermodynamic equilibrium for vapor and temperature which basically means that the vapor flux and subsequently the interface velocity, is completely determined by local temperature gradients in the vicinity of the ice-air interface. To obtain an improved interface velocity, the mass transport equation should be solved with the Gibbs-Thomson boundary condition, including the curvature and/or kinetic corrections. It remains uncertain however, if this inclusion would be sufficient to capture the decay of the SSA since additional effects like the observed growth-sublimation asymmetry (Fig. 4.6) are then still not included.

To quantify the effect of the boundary conditions on the interface velocity, it might be interesting to conduct numerical studies such as phase-field simulations. Recently a successful attempt to simulate the morphology of precipitation particles was done by Demange et al. [2017a,b]. From these studies we learn that two types of anisotropy control the growth laws that lead to the known complex morphologies of precipitation particles. The first is given by an anisotropy in the condensation coefficient (kinetics), which cause a geometrical anisotropy resulting in plate-like or needle-like particles. A second anisotropy is related to the surface tension, which manifests the hexagonal symmetry. Both anisotropies are inherited from the underlying crystal orientation. If the inclusion of crystal orientation will solve open questions in metamorphism in snow, remains to be seen, however the much observed faceted crystals, hexagonal and cubic depth hoar crystals in temperature gradient experiments indicate that crystal growth is fairly dependent on these effects. Applying phase-field modeling directly to snow however bares the fundamental difficulty

of high computational demands [Kaempfer and Plapp, 2009]. With recent advances in this field it is more likely that phase-field modeling of single grains under temperature gradient conditions, combined with experimental studies like Adams and Miller [2002], would be an interesting first step to reveal the relevant growth laws for temperature gradient metamorphism.

From an experimental point of view, assessing crystal orientation during metamorphism can presently be determined destructively by thin-sections [Riche et al., 2012, Calonne et al., 2017] which prohibits measuring growth rates in that setup. A proof of concept of simultaneously retrieving 3D imaging and local crystal orientation by X-Ray Diffraction Contrast Tomography is done by Rolland du Roscoat et al. [2011]. Though promising for future research, the method is quite complex and has not yet been systematically developed.

The combination of a phase field model including anisotropy, combined with in-situ imaging of microstructures and crystal orientation, and a generalization of the developed rigorous averaging scheme to crystal anisotropy would ultimately advance understanding of metamorphism in snow.

Bibliography

- E. E. Adams and R. L. Brown. A model for crystal development in dry snow. *Geophys. Res. Lett.*, 9(11):1287–1289, 1982. doi: 10.1029/GL009i011p01287.
- E. E. Adams and D. A. Miller. Morphology of crystal growth and grain bonding in snow. *Proceedings of the 2002 ISSW*, pages 323–327, 2002.
- H. Akaike. *Selected papers of Hirotugu Akaike*, pages 199–213. Springer New York, 1998. doi: 10.1007/978-1-4612-1694-0_15.
- L. Arnaud, G. Picard, N. Champollion, F. Domine, J. Gallet, E. Lefebvre, M. Fily, and J. Barnola. Measurement of vertical profiles of snow specific surface area with a 1 cm resolution using infrared reflectance: instrument description and validation. *J. Glaciol.*, 57(201):17–29, 2011. doi: 10.3189/002214311795306664.
- J. Baerentzen and H. Aanaes. Signed distance computation using the angle weighted pseudonormal. *IEEE Trans. Vis. Comput. Graphics*, 11(3):243–253, 2005.
- M. Barrere, F. Domine, B. Decharme, S. Morin, V. Vionnet, and M. Lafaysse. Evaluating the performance of coupled snow-soil models in surfexv8 to simulate the permafrost thermal regime at a high arctic site. *Geosci. Model Dev. Discuss.*, 2017:1–38, 2017. doi: 10.5194/gmd-2017-50.
- J. W. Barrett, H. Garcke, and R. Nürnberg. Numerical computations of faceted pattern formation in snow crystal growth. *Phys. Rev. E*, 86:011604, 2012. doi: 10.1103/PhysRevE.86.011604.
- P. Bartelt and M. Lehning. A physical {SNOWPACK} model for the swiss avalanche warning: Part i: numerical model. *Cold Reg. Sci. Technol.*, 35(3):123 – 145, 2002. doi: 10.1016/S0165-232X(02)00074-5.
- S. J. Bartlett, J.-D. Rüedi, A. Craig, and C. Fierz. Assessment of techniques for analyzing snow crystals in two dimensions. *Ann. Glaciol.*, 48(1):103–112, 2008. doi: 10.3189/172756408784700752.
- J. G. Berryman. Planar spatial correlations, anisotropy, and specific surface area of stationary random porous media. *J. App. Phys.*, 83(3):1685–1693, 1998. doi: 10.1063/1.366885.
- J. G. Berryman. Comparison of upscaling methods in poroelasticity and its generalizations. *Journal of Engineering Mechanics*, 131(9):928–936, 2005. doi: 10.1061/(ASCE)0733-9399(2005)131:9(928).

- L. Brucker, G. Picard, and M. Fily. Snow grain-size profiles deduced from microwave snow emissivities in antarctica. *J. Glaciol.*, 56(197):514–526, 2010. doi: doi:10.3189/002214310792447806.
- E. Brun, P. David, M. Sudul, and G. Brunot. A numerical model to simulate snow-cover stratigraphy for operational avalanche forecasting. *J. Glac.*, 38(128):13–22, 1992. doi: 10.3198/1992JoG38-128-13-22.
- J. B. Brzoska, F. Flin, and N. Ogawa. Using gaussian curvature for the 3D segmentation of snow grains from microtomographic data. In W. F. Kuhs, editor, *Physics and Chemistry of Ice*, page 125, 2007.
- J.-B. Brzoska, F. Flin, and J. Barckicke. Explicit iterative computation of diffusive vapour field in the 3d snow matrix: preliminary results for low flux metamorphism. *Ann. Glaciol.*, 48(1):13–18, 2008. doi: 10.3189/172756408784700798.
- N. Calonne, F. Flin, C. Geindreau, B. Lesaffre, and S. Rolland du Roscoat. Study of a temperature gradient metamorphism of snow from 3d images: time evolution of microstructures, physical properties and their associated anisotropy. *Cryosphere*, 8(6):2255–2274, 2014a. doi: 10.5194/tc-8-2255-2014.
- N. Calonne, C. Geindreau, and F. Flin. Macroscopic modeling for heat and water vapor transfer in dry snow by homogenization. *J. Phys. Chem. B*, 118(47):13393–13403, 2014b. doi: 10.1021/jp5052535.
- N. Calonne, F. Flin, B. Lesaffre, A. Dufour, J. Roulle, P. Puglièse, A. Philip, F. Lahoucine, C. Geindreau, J.-M. Panel, S. Rolland du Roscoat, and P. Charrier. CellDyM: A room temperature operating cryogenic cell for the dynamic monitoring of snow metamorphism by time-lapse X-ray microtomography. *Geophys. Res. Lett.*, 42(10):3911–3918, 2015. doi: 10.1002/2015GL063541.
- N. Calonne, M. Montagnat, M. Matzl, and M. Schneebeli. The layered evolution of fabric and microstructure of snow at point barnola, central east antarctica. *Earth and Planetary Science Letters*, 460:293 – 301, 2017. ISSN 0012-821X. doi: <http://dx.doi.org/10.1016/j.epsl.2016.11.041>.
- T. Carlsen, G. Birnbaum, A. Ehrlich, J. Freitag, G. Heygster, L. Istomina, S. Kipfstuhl, A. Orsi, M. Schäfer, and M. Wendisch. Comparison of different methods to retrieve effective snow grain size in central antarctica. *The Cryosphere Discussions*, 2017:1–20, 2017. doi: 10.5194/tc-2016-294.
- C. M. Carmagnola, S. Morin, M. Lafaysse, F. Domine, B. Lesaffre, Y. Lejeune, G. Picard, and L. Arnaud. Implementation and evaluation of prognostic representations of the optical diameter of snow in the surfex/isba-crocus detailed snowpack model. *The Cryosphere*, 8(2):417–437, 2014. doi: 10.5194/tc-8-417-2014.
- H. S. Carslaw and J. C. Jaeger. *Conduction of Heat in Solids*. Oxford University Press, USA, 1986.
- S. C. Colbeck. An overview of seasonal snow metamorphism. *Rev. Geophys.*, 20(1):45–61, 1982. doi: 10.1029/RG020i001p00045.

- S. C. Colbeck. Theory of metamorphism of dry snow. *J. Geophys. Res. Oceans*, 88(C9):5475–5482, 1983. doi: 10.1029/JC088iC09p05475.
- C. Coléou, B. Lesaffre, J.-B. Brzoska, W. Ludwig, and E. Boller. Three-dimensional snow images by X-ray microtomography. *Ann. Glaciol.*, 32:75–81, 2001. doi: 10.3189/172756401781819418.
- R. Dadic, B. Light, and S. G. Warren. Migration of air bubbles in ice under a temperature gradient, with application to “Snowball Earth” . *J. Geophys. Res. Atmos.*, 115(D18125), 2010. doi: 10.1029/2010JD014148.
- P. Debye, H. Anderson, and H. Brumberger. Scattering by an inhomogeneous solid .2. the correlation function and its application. *J. Appl. Phys.*, 28(6):679–683, 1957. doi: 10.1063/1.1722830.
- G. Demange, H. Zapolsky, R. Patte, and M. Brunel. A phase field model for snow crystal growth in three dimensions. *npj Computational Materials*, 3(1):15, 2017a. doi: 10.1038/s41524-017-0015-1.
- G. Demange, H. Zapolsky, R. Patte, and M. Brunel. Growth kinetics and morphology of snowflakes in supersaturated atmosphere using a three-dimensional phase-field model. *Phys. Rev. E*, 96:022803, Aug 2017b. doi: 10.1103/PhysRevE.96.022803.
- S. Deville. Ice-templating, freeze casting: Beyond materials processing. *Journal of Materials Research*, 28(17):2202–2219, 2013. doi: 10.1557/jmr.2013.105.
- K.-H. Ding, X. Xu, and L. Tsang. Electromagnetic scattering by bicontinuous random microstructures with discrete permittivities. *IEEE Trans. Geosci. Remote Sens.*, 48(8):3139–3151, 2010. doi: 10.1109/TGRS.2010.2043953.
- F. Domine, R. Salvatori, L. Legagneux, R. Salzano, M. Fily, and R. Casacchia. Correlation between the specific surface area and the short wave infrared (swir) reflectance of snow. *Cold Reg. Sci. Technol.*, 46(1):60 – 68, 2006. doi: 10.1016/j.coldregions.2006.06.002.
- F. Domine, A.-S. Taillandier, A. Cabanes, T. A. Douglas, and M. Sturm. Three examples where the specific surface area of snow increased over time. *The Cryosphere*, 3(1):31–39, 2009. doi: 10.5194/tc-3-31-2009.
- F. Domine, M. Barrere, and D. Sarrazin. Seasonal evolution of the effective thermal conductivity of the snow and the soil in high arctic herb tundra at bylot island, canada. *The Cryosphere*, 10(6):2573–2588, 2016. doi: 10.5194/tc-10-2573-2016.
- D. A. Drew. Evolution of geometric statistics. *SIAM J. Appl. Math.*, 50(3):649–666, 1990. doi: 10.1137/0150038.
- M. Dumont, E. Brun, G. Picard, M. Michou, Q. Libois, J.-R. Petit, M. Geyer, S. Morin, and B. Josse. Contribution of light-absorbing impurities in snow to greenland/’s darkening since 2009. *Nature Geosci.*, 7(7):509–512, 07 2014. doi: 10.1038/ngeo2180.
- M. Durand, E. J. Kim, and S. A. Margulis. Quantifying uncertainty in modeling snow microwave radiance for a mountain snowpack at the point-scale, including stratigraphic effects. *IEEE T Geosci. Remote*, 46:1753–1767, 2008. doi: 10.1109/TGRS.2008.916221.

- C. Fierz and M. Lehning. Assessment of the microstructure-based snow-cover model snowpack: thermal and mechanical properties. *Cold Reg. Sci. Technol.*, 33(2):123 – 131, 2001. doi: 10.1016/S0165-232X(01)00033-7.
- C. Fierz, R. L. Armstrong, Y. Durand, P. Etchevers, E. Greene, D. M. McClung, K. Nishimura, P. K. Satyawali, and S. Sokratov. The international classification for seasonal snow on the ground. *IHP-VII Technical Documents in Hydrology, 83, IACS Contribution (1), UNESCO-IHP, Paris*, 2009.
- J. Fife, J. Gibbs, E. Gulsoy, C.-L. Park, K. Thornton, and P. Voorhees. The dynamics of interfaces during coarsening in solid-liquid systems. *Acta Mat.*, 70:66–78, 2014. doi: 10.1016/j.actamat.2014.01.024.
- H. Flanders. Differentiation under the integral sign. *The American Mathematical Monthly*, 80(6):615–627, 1973. doi: 10.2307/2319163.
- M. G. Flanner and C. S. Zender. Linking snowpack microphysics and albedo evolution. *J. Geophys. Res.*, page D12208, 2006.
- F. Flin, J.-B. Brzoska, B. Lesaffre, C. Coléou, and R. A. Pieritz. Full three-dimensional modelling of curvature-dependent snow metamorphism: first results and comparison with experimental tomographic data. *J. Phys. D: Appl. Phys.*, 36(10A):A49, 2003. doi: 10.1088/0022-3727/36/10A/310.
- F. Flin, J.-B. Brzoska, B. Lesaffre, C. Coléou, and R. A. Pieritz. Three-dimensional geometric measurements of snow microstructural evolution under isothermal conditions. *Ann. Glaciol.*, 38(1):39–44, 2004. doi: 10.3189/172756404781814942.
- F. Flin, J.-B. Brzoska, D. Coeurjolly, R. Pieritz, B. Lesaffre, C. Coleou, P. Lamboley, F. Teytaud, G. L. Vignoles, and J.-F. Delesse. Adaptive estimation of normals and surface area for discrete 3d objects: application to snow binary data from x-ray tomography. *Image Processing, IEEE Transactions on*, 14(5):585–596, 2005. doi: 10.1109/TIP.2005.846021.
- H. L. Frisch and F. H. Stillinger. Contribution to the statistical geometric basis of radiation scattering. *J. Chem. Phys.*, 38(9):2200–2207, 1963. doi: 10.1063/1.1733950.
- H. Garcke. Curvature driven interface evolution. *Jahresbericht der Deutschen Mathematiker-Vereinigung*, 115(2):63–100, 2013. doi: 10.1365/s13291-013-0066-2.
- A. S. Gardner and M. J. Sharp. A review of snow and ice albedo and the development of a new physically based broadband albedo parameterization. *J. Geophys. Res-Earth*, 115(F1): 2156–2202, 2010. doi: 10.1029/2009JF001444.
- W. Gille. Chord length distributions and small-angle scattering. *Eur. Phys. J. B*, 17(3):371–383, 2000. doi: 10.1007/s100510070116.
- P. Hagenmuller, M. Matzl, G. Chambon, and M. Schneebeli. Sensitivity of snow density and specific surface area measured by microtomography to different image processing algorithms. *The Cryosphere*, 10(3):1039–1054, 2016. doi: 10.5194/tc-10-1039-2016.

- K. Hammonds, R. Lieb-Lappen, I. Baker, and X. Wang. Investigating the thermophysical properties of the ice–snow interface under a controlled temperature gradient. *Cold Reg. Sci. Technol.*, 120:157 – 167, 2015. doi: 10.1016/j.coldregions.2015.09.006.
- A. C. Hansen and W. E. Foslien. A macroscale mixture theory analysis of deposition and sublimation rates during heat and mass transfer in dry snow. *The Cryosphere*, 9(5):1857–1878, 2015. doi: 10.5194/tc-9-1857-2015.
- S. Haussener, M. Gergely, M. Schneebeli, and A. Steinfeld. Determination of the macroscopic optical properties of snow based on exact morphology and direct pore-level heat transfer modeling. *J. Geophys. Res-Earth*, 117(F3):F03009, 2012. doi: 10.1029/2012JF002332.
- A. Hernderson. ParaView Guide, A Parallel Visualization Application. Kitware Inc., 2007.
- C. Huggel. *The High-Mountain Cryosphere: Environmental Changes and Human Risks*. Cambridge University Press, 2015.
- IPCC. *Summary for Policymakers*. Cambridge University Press, Cambridge, United Kingdom and New York, NY, USA, 2013. ISBN ISBN 978-1-107-66182-0. doi: 10.1017/CBO9781107415324.004.
- T. U. Kaempfer and M. Plapp. Phase-field modeling of dry snow metamorphism. *Phys. Rev. E*, 79(3, Part 1), 2009. ISSN 1539-3755. doi: 10.1103/PhysRevE.79.031502.
- T. U. Kaempfer and M. Schneebeli. Observation of isothermal metamorphism of new snow and interpretation as a sintering process. *J. Geophys. Res-Atmospheres*, 112(D24), 2007. doi: 10.1029/2007JD009047. D24101.
- F. Koch, M. Prasch, L. Schmid, J. Schweizer, and W. Mauser. Measuring snow liquid water content with low-cost gps receivers. *Sensors*, 14(11):20975–20999, 2014. doi: 10.3390/s141120975.
- A. A. Kokhanovsky and E. P. Zege. Scattering optics of snow. *Appl. Opt.*, 43(7):1589–1602, 2004. doi: 10.1364/AO.43.001589.
- Q. Krol and H. Löwe. Analysis of local ice crystal growth in snow. *J. Glaciol*, 62(232):378–390, 2016a. doi: 10.1017/jog.2016.32.
- Q. Krol and H. Löwe. Relating optical and microwave grain metrics of snow: the relevance of grain shape. *The Cryosphere*, 10(6):2847–2863, 2016b. doi: 10.5194/tc-10-2847-2016.
- A. Kuprat, A. Khamayseh, D. George, and L. Larkey. Volume conserving smoothing for piecewise linear curves, surfaces, and triple lines. *J. Comput. Phys.*, 172(1):99–118, 2001. doi: 10.1006/jcph.2001.6816.
- Y. Kwon, K. Thornton, and P. W. Voorhees. Coarsening of bicontinuous structures via nonconserved and conserved dynamics. *Phys. Rev. E*, 75:021120, 2007. doi: 10.1103/PhysRevE.75.021120.
- L. Legagneux and F. Dominé. A mean field model of the decrease of the specific surface area of dry snow during isothermal metamorphism. *J. Geophys. Res. Earth*, 110:F04011, 2005. doi: 10.1029/2004JF000181.

- L. Legagneux, A. Cabanes, and F. Dominé. Measurement of the specific surface area of 176 snow samples using methane adsorption at 77 K. *J. Geophys. Res-Atmospheres*, 107(D17): 4335, 2002. doi: 10.1029/2001JD001016.
- M. Lehning, P. Bartelt, B. Brown, C. Fierz, and P. Satyawali. A physical snowpack model for the Swiss avalanche warning: Part II. Snow microstructure. *Cold Reg. Sci. Technol.*, 35(3):147–167, 2002. doi: 10.1016/S0165-232X(02)00073-3.
- S. Leinss, H. Löwe, M. Proksch, J. Lemmetyinen, A. Wiesmann, and I. Hajsek. Anisotropy of seasonal snow measured by polarimetric phase differences in radar time series. *The Cryosphere*, 10(4):1771–1797, 2016. doi: 10.5194/tc-10-1771-2016.
- B. Lesaffre, E. Pougatch, and E. Martin. Objective determination of snow-grain characteristics from images. *Ann. Glaciol.*, 26:112–118, 1998.
- P. Levitz and D. Tchoubar. Disordered porous solids : from chord distributions to small angle scattering. *J. de Phys. I*, 2(6):771–790, 1992. doi: 10.1051/jp1:1992174.
- K. Libbrecht. Growth rates of the principal facets of ice between -10°C and -40°C . *J. Cryst. Growth*, 247(3-4):530–540, 2003. doi: 10.1016/S0022-0248(02)01996-6.
- K. Libbrecht. *Ken Libbrecht’s Field Guide to Snowflakes*. Voyageur Press, 2006.
- K. G. Libbrecht. The physics of snow crystals. *Rep. Prog. Phys.*, 14(4):599–895, 2005.
- Q. Libois, G. Picard, M. Dumont, L. Arnaud, C. Sergent, E. Pougatch, M. Sudul, and D. Vial. Experimental determination of the absorption enhancement parameter of snow. *J. Glaciol.*, 60(222):714–724, 2014. doi: 10.3189/2014J0G14J015.
- Q. Libois, G. Picard, J. L. France, L. Arnaud, M. Dumont, C. M. Carmagnola, and M. D. King. Influence of grain shape on light penetration in snow. *Cryosphere*, 7(6):1803–1818, 2013. doi: 10.5194/tc-7-1803-2013.
- I. Lifshitz and V. Slyozov. The kinetics of precipitation from supersaturated solid solutions. *J. Phys. Chem. Solids*, 19(1–2):35–50, 1961. doi: 10.1016/0022-3697(61)90054-3.
- S. Linow, M. Hörhold, and J. Freitag. Grain-size evolution of polar firn: a new empirical grain growth parameterization based on x-ray microcomputer tomography measurements. *Journal of Glaciology*, 58(212):1245–1252, 2012. doi: 10.3189/2012JoG11J256.
- H. Löwe and G. Picard. Microwave scattering coefficient of snow in memls and dmrt-ml revisited: the relevance of sticky hard spheres and tomography-based estimates of stickiness. *Cryosphere*, 9(6):2101–2117, 2015. doi: 10.5194/tc-9-2101-2015.
- H. Löwe, J. K. Spiegel, and M. Schneebeli. Interfacial and structural relaxations of snow under isothermal conditions. *J. Glaciol.*, 57(203):499–510, 2011. doi: 10.3189/002214311796905569.
- H. Löwe, F. Riche, and M. Schneebeli. A general treatment of snow microstructure exemplified by an improved relation for thermal conductivity. *The Cryosphere*, 7(5):1473–1480, 2013. doi: 10.5194/tc-7-1473-2013.

- C. R. López-Barrón and C. W. Macosko. Direct measurement of interface anisotropy of bicontinuous structures via 3d image analysis. *Langmuir*, 26(17):14284–14293, 2010. doi: 10.1021/la102314r.
- A. V. Malinka. Light scattering in porous materials: Geometrical optics and stereological approach. *J. Quant. Spectrosc. Ra.*, 141:14–23, JUL 2014. doi: 10.1016/j.jqsrt.2014.02.022.
- M. Matzl and M. Schneebeli. Measuring specific surface area of snow by near-infrared photography. *J. Glaciol.*, 52(179):558–564, 2006. doi: 10.3189/172756506781828412.
- C. Mätzler. Improved born approximation for scattering of radiation in a granular medium. *J. Appl. Phys.*, 83(11, 1):6111–6117, 1998.
- C. Mätzler. Relation between grain-size and correlation length of snow. *J. Glac.*, 48(162): 461–466, 2002. doi: 10.3189/172756502781831287.
- C. Mätzler and A. Wiesmann. Extension of the microwave emission model of layered snowpacks to coarse-grained snow. *Rem. Sens. Environ.*, 70(3):317–325, DEC 1999. doi: 10.1016/S0034-4257(99)00047-4.
- R. I. McLachlan and H. Segur. A note on the motion of surfaces. *Phys. Lett. A*, 194(3):165 – 172, 1994. doi: 10.1016/0375-9601(94)91278-5.
- J. Méring and D. Tchoubar. Interprétation de la diffusion centrale des rayons X par les systèmes poreux. I. *J. App. Crystallogr.*, 1(3):153–165, 1968. doi: 10.1107/S0021889868005212.
- M. A. Micha, C. Burger, and M. Antonietti. Generalized phase diagram for microphase-separated systems and its determination by small-angle scattering. *Macromolecules*, 31(17):5930–5933, 1998. doi: 10.1021/ma980085c.
- K. Michielsen and H. D. Raedt. Integral-geometry morphological image analysis. *Phys. Rep.*, 347(6):461 – 538, 2001. doi: 10.1016/S0370-1573(00)00106-X.
- D. A. Miller and E. E. Adams. A microstructural dry-snow metamorphism model for kinetic crystal growth. *J. Glaciol.*, 55(194):1003–1011, 2009.
- C. Morel. On the surface equations in two-phase flows and reacting single-phase flows. *Int. J. Multiph. Flow*, 33:1045–1073, 2007. doi: 10.1016/j.ijmultiphaseflow.2007.02.008.
- U. Nakaya. *Snow Crystals: Natural and Artificial*. Harvard University Press, Cambridge, MA, 1954.
- M. Newman and G. Barkema. *Monte carlo methods in statistical physics*. Clarendon Press, 1999.
- J. Pan, M. Durand, M. Sandells, J. Lemmetyinen, E. J. Kim, J. Pulliainen, A. Kontu, and C. Derksen. Differences between the hut snow emission model and memls and their effects on brightness temperature simulation. *IEEE T Geosci. Remote*, 54(4):2001–2019, 2016. ISSN 0196-2892. doi: 10.1109/TGRS.2015.2493505.
- C.-L. Park, P. Voorhees, and K. Thornton. Evolution of interfacial curvatures of a bicontinuous structure generated via nonconserved dynamics. *Acta Mater.*, 90:182 – 193, 2015. doi: 10.1016/j.actamat.2015.02.037.

- R. Perla, J. Dozier, and R. E. Davis. Preparation of serial sections in dry snow specimens. *J. Microsc.*, 142(1):111–114, 1986. doi: 10.1111/j.1365-2818.1986.tb02744.x.
- G. Picard, L. Arnaud, F. Domine, and M. Fily. Determining snow specific surface area from near-infrared reflectance measurements: Numerical study of the influence of grain shape. *Cold Reg. Sci. Technol.*, 56(1):10–17, APR 2009. ISSN 0165-232X. doi: 10.1016/j.coldregions.2008.10.001.
- B. Pinzer and M. Schneebeli. Breeding snow: an instrumented sample holder for simultaneous tomographic and thermal studies. *Meas. Sci. Technol.*, 20(9):095705, 2009. doi: 10.1088/0957-0233/20/9/095705.
- B. R. Pinzer, M. Schneebeli, and T. U. Kaempfer. Vapor flux and recrystallization during dry snow metamorphism under a steady temperature gradient as observed by time-lapse micro-tomography. *The Cryosphere*, 6(5):1141–1155, 2012. doi: 10.5194/tc-6-1141-2012.
- M. Proksch, H. Löwe, and M. Schneebeli. Density, specific surface area and correlation length of snow measured by high-resolution penetrometry. *J. Geophys. Res.–Earth*, 120:346–362, 2015a. doi: 10.1002/2014JF003266.
- M. Proksch, C. Mätzler, A. Wiesmann, J. Lemmetyinen, M. Schwank, H. Löwe, and M. Schneebeli. Memls3&a: Microwave emission model of layered snowpacks adapted to include backscattering. *Geosci. Mod. Dev.*, 8(8):2611–2626, 2015b. doi: 10.5194/gmd-8-2611-2015.
- C. Quammen, C. Weigle, and R. T. II. Boolean operations on surfaces in vtk without external libraries. *VTK Journal*, 05 2011.
- L. Ratke and P. Voorhees. *Growth and coarsening*. Springer, New York, 2002.
- F. Riche, M. Schneebeli, and S. Tschanz. Design-based stereology to quantify structural properties of artificial and natural snow using thin sections. *Cold Reg. Sci. Technol.*, 79:67 – 74, 2012. doi: 10.1016/j.coldregions.2012.03.008.
- A. Roberts and S. Torquato. Chord-distribution functions of three-dimensional random media: Approximate first-passage times of Gaussian processes. *Phys. Rev. E*, 59(5, A):4953–4963, MAY 1999. ISSN 1063-651X. doi: 10.1103/PhysRevE.59.4953.
- S. Rolland du Roscoat, A. King, A. Philip, P. Reischig, W. Ludwig, F. Flin, and J. Meyssonier. Analysis of snow microstructure by means of x-ray diffraction contrast tomography. *Adv. Eng. Mater.*, 13(3):128–135, 2011. doi: 10.1002/adem.201000221.
- A. Roy, G. Picard, A. Royer, B. Montpetit, F. Dupont, A. Langlois, C. Derksen, and N. Champollion. Brightness temperature simulations of the canadian seasonal snowpack driven by measurements of the snow specific surface area. *IEEE Trans. Geosci. Remote sens*, 51(9): 4692–4704, 2013. doi: 10.1109/TGRS.2012.2235842.
- Y. Saito. *Statistical Physics of Crystal Growth*. World Scientific, 1996.
- S. Schleef and H. Löwe. X-ray microtomography analysis of isothermal densification of new snow under external mechanical stress. *J. Glaciol.*, 59(214):233–243, 2013. doi: 10.3189/2013JoG12J076.

- S. Schleef, H. Löwe, and M. Schneebeli. Influence of stress, temperature and crystal morphology on isothermal densification and specific surface area decrease of new snow. *The Cryosphere*, 8(5):1825–1838, 2014. doi: 10.5194/tc-8-1825-2014.
- S. Schleef, H. Löwe, and M. Schneebeli. Hot-pressure sintering of low-density snow analyzed by X-ray microtomography and in situ microcompression. *Act. Mater.*, 71:185–194, 2014. doi: 10.1016/j.actamat.2014.03.004.
- M. Schneebeli and S. Sokratov. Tomography of temperature gradient metamorphism of snow and associated changes in heat conductivity. *Hydrol. Process.*, 18(18, SI):3655–3665, 2004. doi: 10.1002/hyp.5800. 61st Eastern Snow Conference (ESC), Portland, ME, JUN 09-11, 2004.
- J. Schweizer and T. Wiesinger. Snow profile interpretation for stability evaluation. *Cold Reg. Sci. Technol.*, 33(2):179 – 188, 2001. doi: 10.1016/S0165-232X(01)00036-2. ISSW 2000:International Snow Science Workshop.
- J. Schweizer, J. Bruce Jamieson, and M. Schneebeli. Snow avalanche formation. *Rev. Geophys.*, 41(4), 2003. doi: 10.1029/2002RG000123.
- J. A. Sethian. *Level Set Methods and Fast Marching Methods*. Cambridge University Press, second edition edition, 1999.
- R. H. Shertzer and E. E. Adams. Anisotropic thermal conductivity model for dry snow. *Cold Reg. Sci. Technol.*, 69(2):122 – 128, 2011. doi: 10.1016/j.coldregions.2011.09.005.
- R. L. Shreve. Migration of air bubbles, vapor figures, and brine pockers in ice under a temperature gradient. *J. Geophys. Res.*, 72(16):4093–4100, 1967. doi: 10.1029/JZ072i016p04093.
- S. Soghrati, A. M. Aragón, C. Armando Duarte, and P. H. Geubelle. An interface-enriched generalized fem for problems with discontinuous gradient fields. *Int. J. Numer. Meth. Eng.*, 89(8):991–1008, 2012.
- M. Spivak. *A comprehensive introduction to differential geometry*. Number v. 3 in A comprehensive introduction to differential geometry. Publish or Perish, Incorporated, 1975.
- J. Sullivan. Curvatures of smooth and discrete surfaces. In A. Bobenko, J. Sullivan, P. Schröder, and G. Ziegler, editors, *Discrete Differential Geometry*, volume 38 of *Oberwolfach Seminars*, pages 175–188. Birkhäuser Basel, 2008. doi: 10.1007/978-3-7643-8621-4_9.
- A.-S. Taillandier, F. Domine, W. R. Simpson, M. Sturm, and T. A. Douglas. Rate of decrease of the specific surface area of dry snow: Isothermal and temperature gradient conditions. *J. Geophys. Res-Earth*, 112(F3003), 2007. doi: 10.1029/2006JF000514.
- S. Tan, M. Aksoy, M. Brogioni, G. Macelloni, M. Durand, K. C. Jezek, T. L. Wang, L. Tsang, J. T. Johnson, M. R. Drinkwater, and L. Brucker. Physical models of layered polar firn brightness temperatures from 0.5 to 2 ghz. *IEEE J. Sel. Top. Appl.*, 8(7):3681–3691, 2015. doi: 10.1109/JSTARS.2015.2403286.
- J. Taylor, J. Cahn, and C. Handwerker. Overview no. 98 i – geometric models of crystal growth. *Act. Metal. Mater*, 40(7):1443–1474, 1992. doi: 10.1016/0956-7151(92)90090-2.

- T. Theile, H. Löwe, T. Theile, and M. Schneebeli. Simulating creep of snow based on microstructure and the anisotropic deformation of ice. *Acta Mater.*, 59(18):7104 – 7113, 2011.
- W. Thomson. Lx. on the equilibrium of vapour at a curved surface of liquid. *Philosophical Magazine*, 42(282):448–452, 1871. doi: 10.1080/14786447108640606.
- H. Tomita. Statistical properties of random interface system. *Prog. Theo. Phys*, 75(3):482–495, 1986. doi: 10.1143/PTP.75.482.
- H. Tomita. An explicit form of the equation of motion of the interface in bicontinuous phases. *Prog. Theor. Phys.*, 104(2):307–324, 2000. doi: 10.1143/PTP.104.307.
- S. Torquato. *Random heterogeneous materials: Microstructure and macroscopic Properties*. Interdisciplinary Applied Mathematics. Springer, 2002.
- E. E. Underwood. Stereology, or the quantitative evaluation of microstructures. *J. Microsc.*, 89(2):161–180, 1969. doi: 10.1111/j.1365-2818.1969.tb00663.x.
- F. Vallese and J. Kong. Correlation-function studies for snow and ice. *J. Appl. Phys.*, 52(8):4921–4925, 1981. doi: 10.1063/1.329453.
- R. Vetter, S. Sigg, H. M. Singer, D. Kadau, H. J. Herrmann, and M. Schneebeli. Simulating isothermal aging of snow. *Europhys. Lett.*, 89(2):26001, 2010. doi: 10.1209/0295-5075/89/26001.
- V. Vionnet, E. Brun, S. Morin, a. Boone, S. Faroux, P. Le Moigne, E. Martin, and J.-M. Willemet. The detailed snowpack scheme crocus and its implementation in surfex v7.2. *Geosci. Model. Develop.*, 5(3):773–791, 2012. doi: 10.5194/gmd-5-773-2012.
- C. Wagner. Theorie der alterung von niederschlagen durch umlösen (ostwald-reifung). *Z. Elektrochem.*, 65(7-8):581–591, 1961.
- K. Wang. Unified model equations for microstructure evolution. *Phys. A*, 387:3084, 2008. doi: 10.3970/icces.2008.005.179.
- S. G. Warren and R. E. Brandt. Optical constants of ice from the ultraviolet to the microwave: A revised compilation. *J. Geophys. Res-Atmos*, 113(D14), 2008. doi: 10.1029/2007JD009744.
- J. Wettlaufer, M. Jackson, and M. Elbaum. A geometric model for anisotropic crystal-growth. *J. Phys. A-Math. Gen.*, 27(17):5957–5967, 1994. doi: 10.1088/0305-4470/27/17/027.
- S. Whitaker. *The Method of Volume Averaging*. Theory and Applications of Transport in Porous Media. Springer Netherlands, 1998.
- M. Wiese and M. Schneebeli. Snowbreeder 5: a micro-ct device for measuring the snow-microstructure evolution under the simultaneous influence of a temperature gradient and compaction. *J. Glaciol*, 63(238):355–360, 2017. doi: 10.1017/jog.2016.143.
- A. Wiesmann and C. Mätzler. Microwave emission model of layered snowpacks. *Remote Sens. Environ.*, 70(3):307–316, 1999. doi: 10.1016/S0034-4257(99)00046-2.
- A. Wiesmann, C. Mätzler, and T. Weise. Radiometric and structural measurements of snow samples. *Radio Sci.*, 33(2):273–289, 1998.

- W. J. Wiscombe and S. G. Warren. A model for the spectral albedo of snow. i: Pure snow. *J. Atmos. Sci.*, 37(12):2712–2733, 1980. doi: 10.1175/1520-0469(1980)037<2712:AMFTSA>2.0.CO;2.
- H.-I. Wu and P. W. Schmidt. Intersect distributions and small-angle X-ray scattering theory. *J. Appl. Crystallogr.*, 4(3):224–231, 1971. doi: 10.1107/S0021889871006745.
- S. Würzer, N. Wever, R. Juras, M. Lehning, and T. Jonas. Modelling liquid water transport in snow under rain-on-snow conditions – considering preferential flow. *Hydrology and Earth System Sciences*, 21(3):1741–1756, 2017. doi: 10.5194/hess-21-1741-2017.
- E. Yokoyama and T. Kuroda. Pattern formation in growth of snow crystals occurring in the surface kinetic process and the diffusion process. *Phys. Rev. A*, 41:2038–2049, 1990. doi: 10.1103/PhysRevA.41.2038.
- J. M. Zalc, S. C. Reyes, and E. Iglesia. The effects of diffusion mechanism and void structure on transport rates and tortuosity factors in complex porous structures. *Chemical Engineering Science*, 59(14):2947 – 2960, 2004. doi: 10.1016/j.ces.2004.04.028.
- L. Zurk, L. Tsang, J. Shi, and R. Davis. Electromagnetic scattering calculated from pair distribution functions retrieved from planar snow sections. *IEEE T. Geosci. Remote*, 35(6): 1419–1428, 1997. doi: 10.1109/36.649796.

Quirine Krol | Curriculum Vitae

In den Büelen 53, 7260, Davos Dorf, Switzerland

☎ +41 762043534 • 📠 +41 814717108

✉ quirine.krol@gmail.com, krol@slf.ch

Education

- PhD Candidate (spring 2014–summer 2017) at EPFL. Supervisors: Prof. M. Lehning and Dr. H. Löwe.
- PhD Student (summer 2013–spring 2017) at the Institute for Snow and Avalanche Research (SLF).
- MSc. Theoretical Physics at Utrecht University (2010-2013). Supervisor: Prof. Gerard Barkema.
- BSc. in Mathematics at Utrecht University (2004–2010). Supervisor: Andre Henriques.
- BSc. in Physics and Astronomy at Utrecht University (2004–2010). Supervisor: Andre Henriques.
- Highschool (VWO), Profile Nature and Technology, Stichtse Vrije School, Zeist, The Netherlands.

Teaching Experience

James Boswell Institute, Student assistant

- Teaching as a Student Assistant in various courses, mostly Physics and Mathematics at a High school level. At an average of 1 day per week for 6 years (2006-2013).
- Teaching intensive Exam Training courses in High School Physics and Mathematics (5 years).
- Individual Tutoring, on Physics and Mathematics.

University Utrecht, Student assistant

- Special Relativity, three semesters (2006/2007, 2007/2008 and 2009/2010).
- Classical Mechanics, first semester (2007/2008).
- Advanced Statistical Physics, first semester (2012/2013).

Publications

Q. Krol and H. Löwe. Upscaling ice-crystal growth dynamics in snow: Rigorous modeling and comparison to 4D X-ray tomography data. submitted to *Acta Materialia*.

Q. Krol and H. Löwe. Analysis of local ice crystal growth in snow. *J. Glaciol*, 2016a. 10.1017/jog.2016.32.

Q. Krol and H. Löwe. Relating optical and microwave grain metrics of snow: the relevance of grain shape. *The Cryosphere*, 2016b.

Conference Contributions

- American Geophysical Union **AGU**, 2016, San Francisco, Poster: Q.Krol and H.Löwe, *The notion of snow grain shape: Ambiguous definitions, retrieval from tomography and implications on remote sensing*.
- Multiscale Materials Modeling **MMM**, 2016, Dijon, Poster: Q.Krol and H.Löwe, *Upscaling the microscopic crystal growth dynamics in snow*, **Awarded best poster**.

- European Geophysical Union **EGU**, 2016, Vienna, Poster: Q.Krol and H.Löwe, *On the relevance of grain shape for microwave and microstructure modeling of snow*.
- International Union of Geodesy and Geophysics **IUGG**, 2015, Prague, Poster: Q.Krol and H.Löwe *Can interfacial curvatures predict the missing size metric in the characterization of snow microstructure?*
- Physics and Chemistry of Ice **PCI**, 2014, Hanover, Poster: Q.Krol, H.Löwe, M. Schneebeli *Estimating local crystal growth laws from time-lapse tomography during snow metamorphism via interface tracking*.

Presentations and Media

- Invited talk, ETHZ, Zurich, 2017, Title: *Snow micro structure: Objective parameters and their evolution*.
- Seminar, MSU, Bozeman, 2016, Title: *Snow micro structural evolution: In search for objective parameters*.
- Participation in Documentary on Snow scientists, Dutch TV-program: 'De kennis van nu'.
- Colloquium, SLF, Davos, 2015 Title: *Snow Dynamics: From microscopic experiments to macroscopic applications via mean-field modeling*.

Languages and Computer Skills

- Dutch (Native), English (Fluent), German (Basic).
- Programming in Python, Mathematica and C/C++ (basics).

Tournaments participation

- Active member and organizer in Team Loll (finalist) in the run for the academic year prize (NRC handelsblad) **science communication** (2005/2006).
- 2nd place with Team Lorentz in the Ukrainian Physics Tournament, Kiev (2006).

Boards and Committees

- Organizer of the yearly female-scientist event (2017).
- Organizer of PhD student trip (2013,2016).
- Editor of the local Climbing magazine committee *RockIn* (2012-2013).
- Student member of the Educational Committee for Physics and astronomy (2007-2011).
- Evaluation Manager for first year Courses in Physics (2006/2007).
- Board member of the Student Committee Physics and Astronomy (2005/2006).

